

1-1-2014

The Mechanics Of Momentum Transfer From Explosive Charges Buried In Water, In Sand, And In Sand With Fines

David M. Fox
Wayne State University,

Follow this and additional works at: https://digitalcommons.wayne.edu/oa_dissertations

 Part of the [Mechanical Engineering Commons](#)

Recommended Citation

Fox, David M., "The Mechanics Of Momentum Transfer From Explosive Charges Buried In Water, In Sand, And In Sand With Fines" (2014). *Wayne State University Dissertations*. 1289.
https://digitalcommons.wayne.edu/oa_dissertations/1289

This Open Access Embargo is brought to you for free and open access by DigitalCommons@WayneState. It has been accepted for inclusion in Wayne State University Dissertations by an authorized administrator of DigitalCommons@WayneState.

**THE MECHANICS OF MOMENTUM TRANSFER FROM
EXPLOSIVE CHARGES BURIED IN WATER, IN SAND,
AND IN SAND WITH FINES**

by

DAVID M. FOX

DISSERTATION

Submitted to the Graduate School

of Wayne State University,

Detroit, Michigan

in partial fulfillment of the requirements

for the degree of

DOCTOR OF PHILOSOPHY

2014

MAJOR: MECHANICAL ENGINEERING

Approved by:

Advisor

Date

Co-advisor

Date

**© COPYRIGHT BY
DAVID M. FOX
2014
ALL RIGHTS RESERVED**

DEDICATION

This work is dedicated to my wife, Chen Xu, to my grandmother, Genevieve Fox, and to my grandfather, Dr. Samuel Fox.

ACKNOWLEDGEMENTS

I am grateful to my colleagues from the University of Maryland, College Park - Professor William Fourney, Uli Leiste, Les Taylor, and Professor Fourney's students - who, among numerous other things, performed and provided the blast experiments; to Jon Windham, Stephen Akers, Kent Danielson, and Paul Reed - my colleagues from the US Army Engineer Research and Development Center in Vicksburg, MS who, among many other things, performed and provided the soil characterizations; to Scott Kukuck, Xiaogang Huang, and Chian Fong Yen from the US Army Research Laboratory; and to my advisors, Professor Joon Sang Lee and Professor Trilochan Singh. I also appreciate the efforts of those on my Committee - Professors Christopher Eamon, Marcis Jansons, and Ming Chia Lai. I am grateful to all of these people for their help and for many, many insights regarding science and engineering in general and this topic in particular. I also very much appreciate all of the support extended to me by Neil Gniazdowski, Ed Fioravante, Nora Eldridge, and Pat Baker of the Weapons and Materials Directorate of the US Army Research Laboratory.

TABLE OF CONTENTS

Dedication.....	ii
Acknowledgments.....	iii
List of Tables	vii
List of Figures	viii
Chapter 1 Introduction.....	1
1.1 Background and motivation for this work	1
1.2 Elements of the mine blast problem	2
1.3 Previous work	3
Chapter 2 Overview of the present work	22
2.1 Research objectives.....	22
2.2 Thesis outline.....	23
Chapter 3 Erosion phenomena: Couette flow in a fluidized bed	25
3.1 Overview of fluidized bed flow investigation	25
3.2 The gas-particle flow model.....	25
3.3 Model geometry.....	27
3.4 Equations of motion for test cases	28
3.5 Definition of boundary conditions.....	29
3.6 Physical properties for gas and particle phases.....	29
3.7 Discretization of equations of motion	31
3.8 Solution method	32
3.9 Comparison of numerical and analytical results	32
3.10 Parameter identification: air velocity distribution	34
3.11 Parameter identification: particle velocity.....	37
3.12 Effect of grid spacing on solution	38
3.13 Iteration convergence	38

3.14	Summary of experimental results	39
3.15	Flow effects resulting from variation of sphericity and particle diameter	40
Chapter 4	The excitation of structures by explosive buried in sand and water	45
4.1	Overview of the sand- and water-based investigation.	45
4.2	Experimental setup.	46
4.3	Computational model	47
4.3.1	Computational techniques.	47
4.3.2	Constitutive models	51
4.4	Results and analysis	60
Chapter 5	Momentum transfer involving sand and soils containing fines	73
5.1	Overview.	73
5.2	Experimental Setup	74
5.2.1	Blast test setup.	74
5.2.2	Test bed preparation	75
5.2.3	Soil Characterization	79
5.3	Computational approach	83
5.3.1	Computational procedures	83
5.3.2	Constitutive models	83
5.4	Comparison of experimental and computational results	91
5.5	Sensitivities to yield surface, hydrostat, and bulk density	94
Chapter 6	Momentum transfer to more complex target geometries	107
6.1	Overview.	107
6.2	Experimental setup.	108
6.3	Computational domain model	110
6.4	Effect of target geometry	112
6.5	Effect of offset loading	116
6.6	Computational results	120

Chapter 7	Conclusions and future research recommendations	124
7.1	Conclusions	124
7.2	Recommendations for future research.	126
References		128
Abstract		139
Autobiographical Statement		141

LIST OF TABLES

Table 1.1	Influence of soil properties on ground shock	10
Table 3.1	Parameter scales for ϵ_p estimate	31
Table 3.2	Physical properties of glass beads and air	31
Table 3.3	Summary of experimental data	40
Table 4.1	Explosive model parameters	51
Table 4.2	Fluid model parameters	52
Table 4.3	Properties for converged wet sand emplacement condition	58
Table 4.4	Miscellaneous soil model parameters	58
Table 4.5	Computational results for the water - wet sand comparison	63
Table 4.6	Computational results for the dry sand - wet sand comparison	65
Table 5.1	Soil emplacement conditions: poorly graded sand (SP).	77
Table 5.2	Soil emplacement conditions: silty sand (SM).	77
Table 5.3	Soil emplacement conditions: clayey sand (SC).	78
Table 5.4	Soil models used for computations	84
Table 5.5	Starting points for sensitivity studies	94
Table 5.6	Soil model characteristics for sensitivity studies	95
Table 5.7	Sensitivity of target momentum to yield strength	96
Table 5.8	Sensitivity of target momentum to lock-up strain	103
Table 5.9	Computational sensitivity of target momentum to wet density	106
Table 6.1	Effect of target geometry	114

LIST OF FIGURES

Figure 1.1	Number of veterans seeking health care	2
Figure 1.2	Economic cost of explosive device injuries	3
Figure 1.3	Components of the mine blast problem	4
Figure 1.4	Examples of early time soil surface deformation	13
Figure 1.5	Plate momentum transfer as a function of diameter and mass	17
Figure 1.6	Bottom surfaces of rigid targets	18
Figure 3.1	Simplified geometry for test cases	28
Figure 3.2	Elastic modulus correlations	30
Figure 3.3	Comparison of single component numerical and analytical solutions	33
Figure 3.4	Comparison of experiment and initial numerical solution	34
Figure 3.5	Air-phase velocity effect, particle viscosity = 1.0 Pa s	35
Figure 3.6	Air-phase velocity effect, particle viscosity = 0.01 Pa s	36
Figure 3.7	Computation mean square error versus particle viscosity	37
Figure 3.8	Mesh sensitivity	38
Figure 3.9	Iteration convergence	39
Figure 3.10	Comparison of experiment and two phase computation	41
Figure 3.11	Effect of sphericity on velocity distribution	42
Figure 3.12	Effect of particle size on velocity distribution	43
Figure 3.13	Prediction of velocity distributions for some real materials	44
Figure 4.1	Experimental setup for sand and water excitation experiments	45
Figure 4.2	Flow chart of ALE time integration loop	49
Figure 4.3	Compressive behavior of dry sand, wet sand, and water	53
Figure 4.4	Particle size distributions for poorly graded concrete sand	54
Figure 4.5	Stress - strain relations for differing sand emplacement conditions	56
Figure 4.6	Yield relations for differing sand emplacement conditions	57

Figure 4.7	Yield surfaces for wet and dry sand	60
Figure 4.8	Comparison of experiment and computation for various target sizes	61
Figure 4.9	Computations for 25.4 cm target loading with wet sand	62
Figure 4.10	Normalized response from the water - wet sand comparison	64
Figure 4.11	Normalized response from the wet sand - dry sand comparison	66
Figure 4.12	Comparison of strain rate and substrate flow	68
Figure 4.13	First order interaction between yield surface type and Poisson ratio	69
Figure 4.14	Uniaxial strain stress path responses	70
Figure 4.15	Effect of Poisson ratio for dry sand	71
Figure 5.1	Apparatus for small scale blast tests	76
Figure 5.2	Soil particle size distributions	79
Figure 5.3	Relation between mean yield strength and soil water content	82
Figure 5.4	Typical soil hydrostats for pressures up to 200 MPa	86
Figure 5.5	Typical soil hydrostats for pressures up to 5 GPa	87
Figure 5.6	Typical soil yield surfaces up to 200 MPa pressure	89
Figure 5.7	Typical soil yield surfaces up to 5 GPa pressure	90
Figure 5.8	Comparison of experiment and computation	92
Figure 5.9	Deviation between experimental means and computations	93
Figure 5.10	Sensitivity of target momentum to yield strength	97
Figure 5.11	Effect of yield strength on flow and target loading	98
Figure 5.12	Effect of yield strength on ejection of soil from bed	99
Figure 5.13	Variation of lock-up strain with air filled void content	100
Figure 5.14	Sensitivity of target momentum to lock-up strain	101
Figure 5.15	Effect of air filled void content on soil ejection and volume fraction	102
Figure 5.16	Effect of air filled voids content on soil ejected from bed	104
Figure 5.17	Computational sensitivity of target momentum to wet density	105
Figure 6.1	Experimental setup for target interaction investigations	109

Figure 6.2	Target plate geometries	110
Figure 6.3	Concrete sand particle size distribution	111
Figure 6.4	ALE three-dimensional mesh	112
Figure 6.5	Mesh convergence	113
Figure 6.6	Impulse as a function of stand-off distance	115
Figure 6.7	Specific impulse as a function of distance from charge center	116
Figure 6.8	Conformation of flat and angled plates 20 ms after detonation	117
Figure 6.9	Effect of bolt supports on target dynamics	118
Figure 6.10	Effect of rotational constraint on kinetic energy	119
Figure 6.11	Computed target momenta for three constitutive sand treatments	120
Figure 6.12	Comparison of computation and experiment	122

Chapter 1

Introduction

1.1 Background and motivation for this work

As a result of recent world events, the ground vehicle mine blast mitigation problem constitutes a research topic that has been generating increased interest and activity. Physical tests and development projects involving full scale vehicle systems that are subjected to blast loads are relatively expensive. The judicious development and implementation of properly conceived computational and analytical methods to better illustrate the mechanics of mine blast phenomena could be used to significantly reduce the scale and cost of experimentation and thus moderate the cost of development of mine protected vehicles and protective equipment for infantry and demining personnel.

A study of demining operations conducted by the United States Department of Defense (2000) indicated that the number and severity of casualties resulting from demining operations could be significantly reduced given, among other things, significant improvements to protective equipment. Furthermore, the United States Department of Defense (2008) reported that more than 2,300 U.S. troops died and almost 22,000 troops - approximately two thirds of all casualties - were wounded between 2001 and 2008 during the Iraq and Afghanistan conflicts as a result of explosive devices such as landmines. Landmines are explosive device that are typically buried in soil and are designed to damage people and structures by means of momentum transfer produced by the interaction of the high explosive and the soil.

As can be seen in Fig. 1.1, the number of U.S. veterans seeking health care as a result of the conflicts in West Asia has been steadily and rapidly rising since 2003 (Stiglitz and Bilmes, 2008). Based on economic estimates from Stiglitz for as well as on the assumption that two out of three of the injuries from the global conflicts result from explosive devices, the economic impact of explosive devices on society has been estimated to be \$277 billion

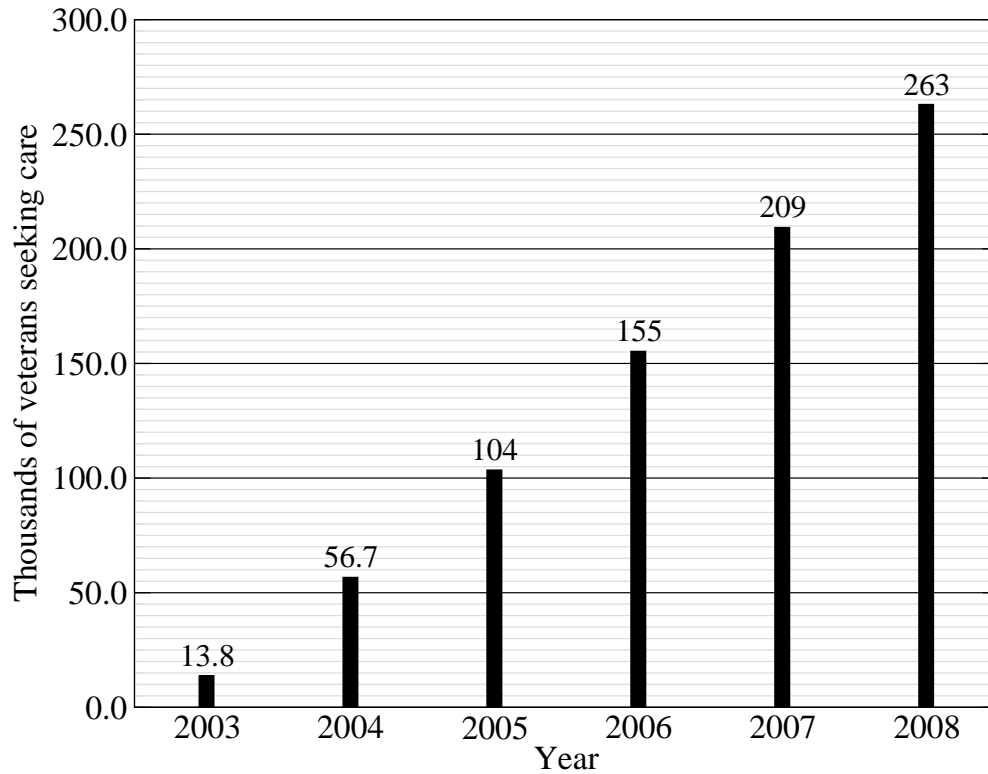


Figure 1.1: Increase in veterans seeking Veterans' Administration health care (from Stiglitz and Bilmes (2008))

(Fig. 1.2). Clearly, then, development of technologies to reduce the destructive effects of explosive devices would have a favorable effect not only on the economy but, more importantly, on the life expectancy and quality of life for those in the military services.

1.2 Elements of the mine blast problem

Analysis of the mine blast problem involves examination of the interactions between high explosives, soil, air and either parts of the human body or structures such as the armored plates associated with commercial and military ground vehicles. The focus of this research was on the behavior of systems comprised of explosive, soil, and various simple structures (Fig 1.3).

The event begins when the solid explosive is detonated and very rapidly generates high pressure gaseous detonation reaction products. Subsequently the detonation products

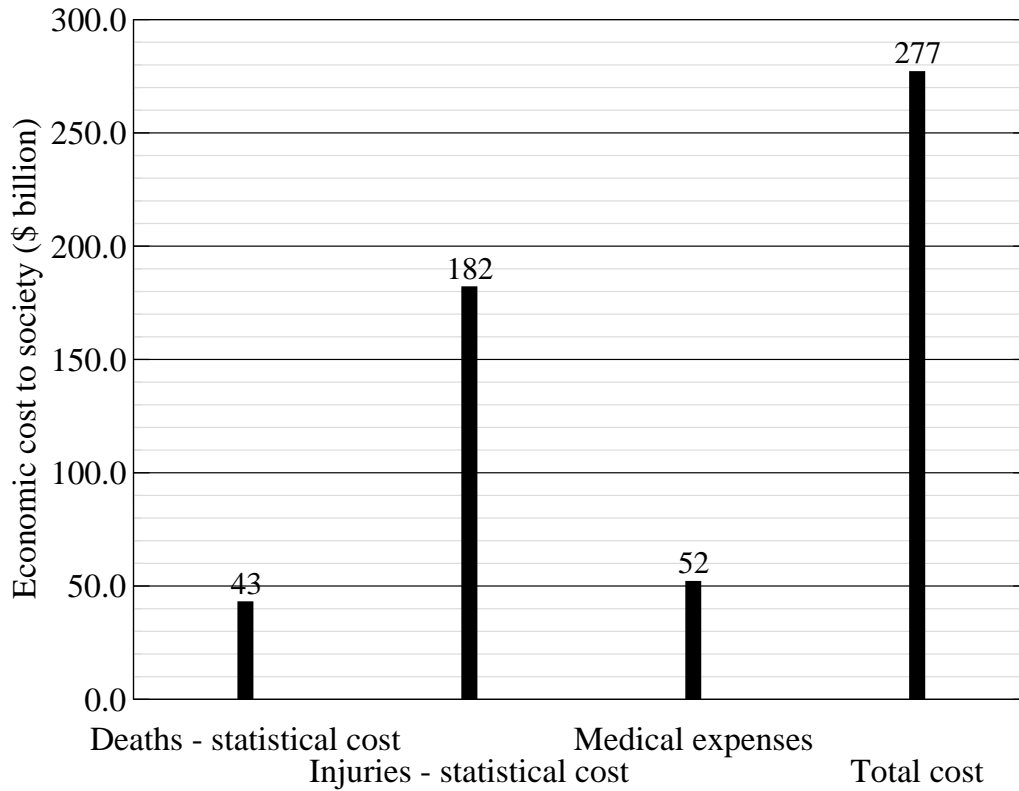


Figure 1.2: Economic cost of explosive device casualties (from Stiglitz and Bilmes (2008))

expand, thereby compressing and shearing the substrate - comprised of soil or water - which produces, via momentum transfer, significant tractions on adjacent surfaces of the structure. This thesis will involve the study and description, in some detail, of the primary mechanisms behind this momentum transfer from the explosive and its enclosing medium to solid structures.

1.3 Previous work

The mine blast problem is one that is very much interdisciplinary in nature. Various factors affect the behavior of the emplaced mine and must be properly identified and defined in order for one to best understand the mechanics associated with mine blast events. A review of the literature indicates that there is an opportunity to improve identification and integration of the various methodological elements required for a more thorough treatment of the problem. These elements include the physics of explosive detonation and certain

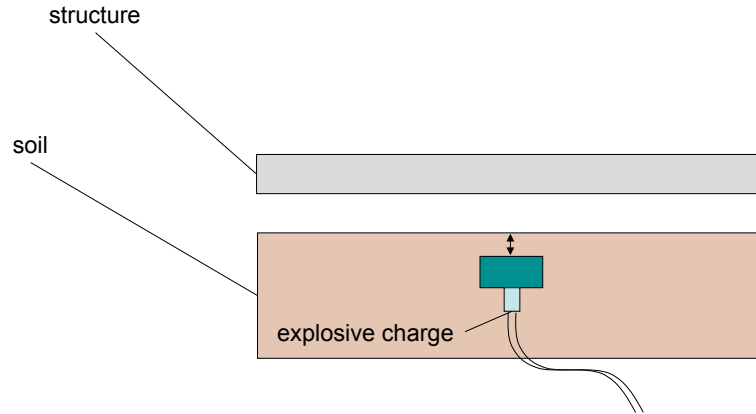


Figure 1.3: Components of the mine blast problem.

aspects of soil mechanics that most directly affect the amount of momentum transferred to a structure from a buried explosive.

Various empirical techniques have been devised and applied to the analysis of blast events. For example, Kingery and Bulmash (1984) collected and compiled air blast data from various sources and, based on these data, used Hopkinson-Cranz and Sachs scaling (Baker, 1973) for prediction of air blast phenomena such as reflected overpressure, shock discontinuity time of arrival, and reflected impulse at various scales for spherical free-air burst and hemispherical surface burst phenomena. Hopkinson-Cranz scaling can be used to scale blast effects based on the mass of high explosive involved in a blast event. Sachs scaling is similar to Hopkinson scaling but enables a correction for atmospheric pressure.

There has thus far been no analogous work that is able to so thoroughly describe and scale blast events that involve buried explosives and soil as a result of the relatively higher level of complexity of such phenomena. Nevertheless, researchers have applied various approaches to the investigation of problems involving explosives detonated while surrounded by various media. In fact, researchers have been investigating the problem of the response of continua comprised of water or geological materials to excitation by relatively shallow (Kolsky et al., 1949; Perkins, 1954) and by more deeply buried explosives (Friedman, 1950;

Lampson, 1946) for at least 60 years. However, it should be added that, over the course of this time, less research in this area has been conducted than one might expect.

This interest in the mechanics of explosive charges buried in water, soil, and rock has been motivated by various problems including crater formation (Nordyke, 1961), ground shock propagation (Jackson, 1969), and mine blast loading (Westine, 1972). For the case of explosive detonations in water, there has been investigation of such applications as damage to underwater structures (Cole, 1965) and the treatment of the blast field produced by submerged explosives (Malme et al., 1966). For problems involving the combination of soil and water, researchers have studied underwater channeling (Fourney, Taylor, and Robeson, 1999).

It has been observed that, for all of these problems, factors such as mass density, compressibility, water content, and strength of the medium surrounding the explosive as well as such things as problem geometry affect experimental outcomes. There has not been, however, an integrated approach combining constitutive data, experimental blast data, and computational analyses for differing soil types at various states that has been extensive enough to expose, to demonstrate, and to explain the fundamental reasons for parametric relations between the momentum of a rigid body and the nature of the medium surrounding a shallow buried explosive.

Various researchers have observed relationships between soil properties or initial state and phenomena associated with explosives buried in geological materials. Lampson (1946) used scaling laws to develop empirical ground shock models for explosive detonated in various soil types. He also investigated crater formation and tried to determine relations between the models and the response of simple buried structures. He observed that, for the soils studied, there was not much variation in the density but the degree of compaction, the water content, and the air filled void content affected the transmission of pressure waves through the soil media. Whitman (1964) recognized the relevance of compressive and shear response of soil to ground motion arising from explosive detonation in or near soil and

offered a detailed description of the nature of these soil behaviors and the tests used to determine them.

Fulmer (1965) performed experiments with 0.454 kg spherical trinitrotoluene charges buried to various depths in beds of wet and dry sand in order to determine the effective of water content on crater size as well as the effect of detonation on the particle size distribution of the sand. The dry sand contained about 0.5% water whereas the wet sand varied between 5.8 and 22% water. It was observed that the craters produced by buried and surface-laid explosive in wet sand were consistently larger than those produced in dry sand. It was also observed that there was some degree of particle size reduction after detonation.

Cherry (1967) performed calculations, using the TENSOR finite difference solver (Maenchen and Sack, 1963), in order to predict mound and cavity growth for very large scale blasts in desert alluvium. Mechanical properties such as density and sonic velocity were determined in the field. Other mechanical properties were determined in the laboratory. Tensile strength was used as the volumetric yield criterion for the alluvium and distortional strain energy as the determinant of the deviatoric yield. Pressure in the alluvium was determined experimentally as a function of specific volume.

DiMaggio and Sandler (1971) presented and validated, for certain quasi-static stress paths and using data for McCormick Ranch Sand, a constitutive treatment that they, in later work, used for prediction of ground shock during blast events. Loading and unloading elastic response of the soil was treated by the assumption of constant Young's and shear moduli. Inelastic behavior was modeled using the combination of a strain hardening cap and an exponential yield surface. The exponential yield surface, for lower levels of pressure, approximated a Drucker-Prager cone but at higher pressures asymptotically approached a Mises cylinder. Cap expansion and contraction was controlled by volumetric plastic strain.

Wenzel and Esparza (1972) performed air blast experiments as well as experiments involving explosives shallow buried in soil by measuring loading pressure on rigid plates by means of Hopkinson-Kolsky bars. They also measured specific impulse by using high

speed movie cameras to calculate the peak velocity of cylindrical plugs, originally mounted in the rigid plates, as they were propelled due to initial surface tractions on their bottom surfaces. They performed a few experiments in order to examine the sensitivity of pressure and impulse to soil water content and, for the case of buried explosive, noticed that wet soil produced significantly higher pressure loadings and specific impulse than that of dry soil.

In subsequent work Wenzel and Esparza (1974) used high speed video to capture the response of deformable plates to excitation by explosive buried in three types of soil - sand, topsoil, and clay - excited by explosive buried in soil at two water contents. They reported that soil type had no great effect on maximum mean permanent plate deformations or on peak global translational momentum imparted to the targets but that water content did have a significant effect as did a reduction in scaled ground clearance and scaled charge mass. They also observed that target dynamic deformation as seen in their high speed films was greater than permanent deformation and that global vertical translation of the center of mass of the plates did not occur until maximum dynamic deformation was reached.

Goodrich et al. (1976) performed computations using the SOC74 finite difference solver, based on an approach used by Terhune, Stubbs, and Cherry (1970) for rock, in order to examine the sensitivity of ground motion and energy coupling to variations in the bulk properties of geological materials. The bulk properties that were varied in the investigation were initial bulk density, initial bulk modulus, water saturation, and shear strength. The materials examined were representative of soil and weak rock. The calculations indicated that the most important parameter was the water saturation level followed by initial bulk density, strength, and initial bulk modulus.

Lottero and Kimsey (1978) used a finite difference Eulerian solver to examine, first, buried mine blast loading on a rigid flat plate and then, in combination with a finite difference structural response solver, to use the flat plate loading to look at the distortion of a deformable flat plate. The soil volumetric behavior, prescribed in terms of the Tillotson

equation of state (Tillotson, 1962), and other constitutive behaviors were not prescribed based on laboratory tests but were estimated based on the properties of dry tuff with water content less than or equal to 5%. The results of these computations, when compared with empirically derived relations agreed, to within 4.5 and 10%, respectively, of the values from the empirical estimates for total impulse and plate deformation.

Henrych (1979) published a compendium of blast technology which addressed such topics as stress wave theory, interactions of explosions with various media, air blast, ground shock, demolition, and explosions in soil. Solutions were derived for idealized examples of explosive effects, such as ground shock, cavities, and craters, but it was emphasized that there is significant variability in properties between different geomaterials and that these properties are critical for the accurate prediction of effects. For example, it was shown, based on experimental results (attributed to Lyakhov (1964)), that air filled void volume fraction had a significant effect on the amplitude of stress waves in sand.

Drake and Little (1983) provided an analysis of data from numerous experiments involving the effect of ground shock on buried structures from explosive detonated near or beneath the ground. Data for various relative densities of granular soils and for various air filled void contents of cohesive soils were provided in a tabular form (see Table 1.1). They indicated that the peak impulse from a shock transmitted through the ground could be predicted according to the scaled empirical relation

$$\frac{I_0}{W^{\frac{1}{3}}} = 1.1 f \rho \left(\frac{R}{W^{\frac{1}{3}}} \right)^{-n+1} \quad (1.1)$$

where I_0 is the peak impulse, W is the explosive charge mass, f is the ground shock coupling factor, ρ is the bulk or wet density of the soil, R is the distance from the explosive charge, and n is the attenuation coefficient. The ground shock coupling factor, f , was defined as the ratio of the ground shock magnitude from partially to shallow buried explosive to the ground shock magnitude from a fully buried burst in the same medium. It varies between

0 and 1 and was parametrized as a function of the scaled depth of burst of the explosive.

The attenuation coefficient n was a function of the seismic velocity since ground shock attenuation depends on relative density for granular soils and on air filled voids content in more cohesive soils, both of which strongly influence seismic velocity. It was also observed that the peak pressure and seismic velocity were proportional to one another. One of the most notable aspects of this work was the way that the authors examined and demonstrated the relationship between the blast-related behavior and the carefully determined mechanical properties of the geological materials used in the experiments.

Westine et al. (1985) applied a scaling approach, using the Buckingham pi theorem, to the development of an empirical model for the prediction of structural impulse loading from explosives detonated in soil. Empirical constants for the relation were estimated based on results from experiments performed for this study as well as on the results developed by Wenzel and Esparza (1972). Although an estimate was made of the speed of sound and the initial bulk, or wet, density of the soil used, no measurements were made of the particle size distribution, water content, porosity, or other characteristics of the soil that was used for the experiments and it was suggested that there was little variation of soil bed properties between experiments.

The empirical model related the scaled peak momentum imparted to the targets to specific or local impulse, mechanical energy available from the explosive, soil bulk density, vertical distance from center of mine to bottom of structure, burial depth of center of mine, cross sectional area of mine (the land-mine was presumed to be pancake-shaped), and lateral distance from center of mine to impulse prediction location on the surface of the structure. It is notable that effects based on soil water content were not deemed important although some of the data from the work by Wenzel and Esparza were used for the modeling effort, and Wenzel and Esparza had indicated, based on their data (Wenzel and Esparza, 1972), that soil water content had a significant effect on target loading.

Artyunov, Grigoryan, and Kamalyan (1985) found that soil moisture content has a

Table 1.1: Effect of soil properties on ground shock parameters (adapted from Drake and Little (1983)).

Soil description	Dry density (kg/m ³)	Wet density (kg/m ³)	Air filled voids (%)	Seismic velocity (m/s)	Acoustic impedance (kg/m ² s)	Attenuation coefficient n
Dry desert alluvium and playa, partially cemented	1,390	1,490 - 1,600	> 25	640 - 1,280	8.9 X 10 ⁵ - 2.05 X 10 ⁶	3.0 - 3.25
Loose, dry, poorly graded sand	1,280	1,440	> 30	180	2.9 X 10 ⁵	3.0 - 3.5
Loose, wet, poorly graded sand - free standing water	1,550	1,860	10	150 -180	2.8 X 10 ⁵ - 3.3 X 10 ⁵	3.0
Dense, wet sand, poorly graded	1,590	1,670	32	270 - 400	4.5 X 10 ⁵ - 6.7 X 10 ⁵	2.5 - 2.75
Dense, dry sand, poorly graded - free standing water	1,730	1,990	9	300	6.0 X 10 ⁵	2.75
Very dense dry sand, relative density = 100%	1,680	1,750	30	490	8.6 X 10 ⁵	2.5
Silty clay, wet	1,520 - 1,600	1,920 - 2,000	9	210 - 270	4.0 X 10 ⁵ - 5.4 X 10 ⁵	2.75 - 3.0
Moist loess, clayey sand	1,600	1,960	5 - 10	300	5.9 X 10 ⁵	2.75 - 3.0
Wet sandy clay, above water table	1,520	1,920 - 2,000	4	550	1.06 X 10 ⁶ - 1.10 X 10 ⁶	2.5
"Saturated" sand - below water table in marsh	- -	- -	1 - 4	1,490	2.57 X 10 ⁶	2.25 - 2.5
"Saturated" sandy clay - below water table	1,250 - 1,600	1,760 - 1,990	1-2	1,520 - 1,830	2.68 X 10 ⁶ - 3.64 X 10 ⁶	2.0 - 2.5
"Saturated" sandy clay - below water table	1,600	2,000	< 1	1,520 - 2,010	3.04 X 10 ⁶ - 4.02 X 10 ⁶	1.5
Saturated stiff clay saturated clay shale	- -	1,920 - 2,080	0	> 1,520	2.92 X 10 ⁶ - 3.16 X 10 ⁶	1.5

significant effect on irreversible deformation, with the effect rising to a peak then descending again with increasing moisture. The authors conducted experiments in a loess-like loam with cylindrical horizontal charges in order to examine the relation between water content and crater cut depth, width, and cross-sectional area. Water content varied between 12 and 27 percent in several steps. They suggested, based on their results, that increasing water content caused the soil to become more prone to flow because the increased levels of water content caused the soil to become less compressible and more elastic, in the volumetric sense, as a result of the relatively lower compressibility of water and soil mineral constituents as compared to that of air.

An hybrid elastic plastic (HEP) soil constitutive model was developed, based on a combination of high pressure quasi-static and shock test results for various geological materials such as soil, rock, and concrete (Wagner et al., 1986; Akers and Stelter, 1991; Zimmerman et al., 1992, 1993; Akers et al., 1995), in order to predict ground shock effects using the finite element method. The high pressure quasi-static testing (of the order of 10^2 MPa) for definition of the constitutive behavior of the geological materials was performed at the US Army Engineer Research and Development Center in Vicksburg, MS.

The HEP model soil behavior uses advanced pressure-volume models and accurately represents the high pressure stress strain characteristics of materials such as soil. The model uses a constant Poisson ratio treatment, uses a two invariant exponential yield surface, and has been extensively validated against explosive field tests (Danielson et al., 2008). In fact, the constitutive models used for the soil computations discussed in this thesis are based directly on material test data generated for the HEP model.

Bergeron et al. (1998) performed blast studies using 106 gram explosive charges on dry, poorly graded sand with the goals of, first, increasing the understanding of the physics behind landmine detonation and of, also, producing a consistent set of data for validation of computational solid and fluid mechanics solvers. They recognized the tremendous influence of test bed definition and preparation on blast mechanics and placed particular emphasis

on the characterization of the soil they were using and on the careful examination of test bed properties before and after tests to improve the consistency between the various tests that were performed and the accuracy of their results.

The tests involved measurement of the movement of the sand and explosive detonation products using high speed film and flash x-rays. Air blast and ground shock pressure histories were also taken using sensors above and within the soil bed. The x-rays and high speed film records showed that, for all cases except for those cases where the top of the explosive was initially placed in the same plane as the top surface of the soil, the detonation products produced a bubble of gas encased in soil which expanded until, at some point, the top of the soil layer opened and the gases escaped (cf. Figure 1.4), and the soil that comprised the boundary of crater and the inner boundary of the soil enveloping the detonation products was eroded by shear stresses produced by the movement of the detonation products escaping the cavity.

It was also observed that the velocity of expansion of the soil cap decreased with increased depth of burial of the explosive. Each of the experiments was repeated at least three times; based on relatively high estimates of variance between the repetitions, and despite the extreme care taken to maintain consistency in the experimental setup, it was noted that the behavior of these types of blast events varies considerably even for cases involving an identical prescription of experimental conditions. For example, the displacement field of the soil subsequent to detonation did not display perfect axial symmetry. Figure 1.4 shows results from two separate test series and gives a sense of the lack of symmetry that was observed.

Wang (2001) performed calculations, using the LS-DYNA finite element solver multiple material arbitrary Lagrangian Eulerian capabilities (Livermore Software Technology Corporation, 2012), and compared the results with some of the experimental data produced by Bergeron et al. (1998). Clear details were not given regarding the identity and characterization of the soil used in the models but computations were performed for two depths

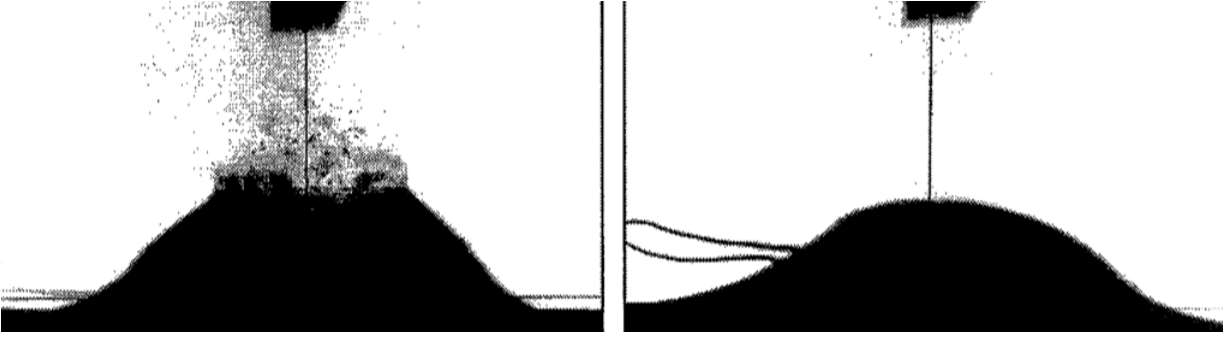


Figure 1.4: Flash x-ray images of early time soil surface deformation (from Bergeron et al. (1998)).

of explosive burial. For the first case, the explosive was buried beneath the soil surface and for the other case, its top was positioned to be flush with the soil surface.

Results of finite element method calculations were compared, for both cases, with experimental results for air blast pressure pulse time of arrival, peak over pressure, and positive phase impulse as measured by pressure transducers located at two positions above the soil surface. The time of arrival calculations closely matched the experimental results whereas the peak pressures were under predicted and the impulses were over predicted. Visualization results from the computations were also compared quantitatively with the experimental results as reported by Bergeron et al. (1998). Predictions of the geometry of explosive bubble expansion and soil movement were similar to what was seen in the experiments.

Braid (2001) performed experiments with the objective of determining the effects of charge size, depth of burial, and soil type on the output of anti-personnel land mines. These investigations involved the use of 50, 100, and 200 gram explosive charges and of two types of soil - a poorly graded medium sand and a well graded silty sand. Both soils were tested in a dry state. The author noticed that the poorly graded sand was not easy to compact whereas the silty sand compacted very readily. This would not be unexpected since a well graded soil with fines - the silty sand - would, by virtue of its increased range in distribution of particle sizes, fill air voids more readily before the onset of close packing

with the concomitant increase in inter-grain forces.

Failure surface, in terms of friction angle, and bulk density were estimated for each soil type at three qualitative levels of compaction. The yield behavior was determined at relatively low pressures - the maximum pressure of the direct shear tests was 189 kPa. Particle size distributions were also determined for the two soils. All of the blast experiments were conducted using what was described as a loose and uncompacted soil state although it was noted that after each test only the densified soil in the vicinity of the explosive was removed and replaced for the subsequent test since it was difficult to remove all of the soil in the test container after each test.

It was observed that the velocity of propagation through the soil was less for the silty sand than for the poorly graded sand. The near-field peak pressures in the soil were higher for the poorly graded sand than for the silty sand but the far field pressures were approximately the same for both soil types. The impulse, however for the silty sand was higher than that for the poorly graded sand. Increased charge size engendered greater ejecta flow velocity and, as would be expected, higher blast energies and pressures. Finally, increased depth of burial yielded greater ejecta velocities and crater sizes.

Gupta (2001) performed calculations, using the CTH solver (McGlaun et al., 1990), in order to better understand the momentum loading on a plate from a mine buried in saturated and dry sand which were assumed to be bounding cases of wet and dry soil. A tabular equation of state for fused quartz was used for the dry sand calculations; a tabular equation of state based on a mixture model previously developed by Kerley (1999) was used for the case of saturated sand. It was assumed that yield strength was independent of pressure. Furthermore, it was supposed that the saturated sand had no yield strength and that a reasonable estimate for the yield strength of the dry sand would be 100 MPa.

It was observed, based on the computational results, that the saturated sand transferred significantly more momentum to the steel plate than did the dry sand. A comparison of the equations of state for the saturated and dry sand showed that, due to its greater porosity, the

dry sand expended a greater proportion of the explosive's available mechanical energy in its compression and therefore less was available for transfer to the plate. It was suggested that further investigation should to be done in order to more clearly identify which mechanisms have the most influence on plate loading.

Laine and Sandvik (2001), by adapting a constitutive model that was originally developed to describe the behavior of an incendiary powder (Moxnes et al., 1999), predicted phenomena associated with shallow-buried blast events involving a sand from the southern Swedish village of Sjöbo. Their initial intent was that the model would be used for ground shock predictions; it was also applied to investigation of a problem that involved demining equipment (Laine et al., 2002).

The soil response was defined in terms of the soil density, a pressure-volume relation, a pressure dependent yield surface, a density dependent sound speed, a density dependent shear modulus, and a relatively low tensile failure limit. The compressive and deviatoric behavior of the soil, prior to void closure, was determined experimentally by means of triaxial tests. The soil properties beyond this point were estimated.

Relatively dry sand was tested to confining pressures of 60 MPa and then the hydrostatic behavior was estimated for pressures beyond this level using a fifth order polynomial fit. The pressure-dependent yield surface was predicted by first performing triaxial shear tests to a pressure of 102 MPa. Next a line was extrapolated to intersect a horizontal line constructed at a deviatoric stress of 225 MPa - the yield strength of Pike's Peak granite.

Kerley (2001, 2002, 2005) performed studies involving various soil types and experimental geometries and in them used the p-alpha model for porous compaction. He defined the volumetric behavior of the soils by combining tabular equations of state for the water and the skeletal constituents. He variously used elastic-perfectly plastic, zero strength, and perfect plasticity strength models similar to that of DiMaggio and Sandler (1971), but without a cap, to define deviatoric behavior. The results of sensitivity studies that he performed (Kerley, 2002) indicated that, within the context of his work, the deviatoric strength of the

soils was the most important determinant of the amount of linear momentum imparted to stationary targets.

Hlady (2004) performed experimental work using explosive buried in two soil types - Suffield prairie soil and concrete fine aggregate sand. It was demonstrated that the energy released by such an arrangement varied significantly with the soil condition. Energy transfer was measured by means of displacement of a target-piston apparatus that was mounted above the buried explosive. Variables that were examined included soil moisture content, soil type, thickness of the soil layer above the explosive, and distance between top of the soil and the target.

Hlady found that, for the sand in general, moisture content between 0 and 10 percent did not have a significant effect on energy transferred to the target but for a test involving what the author called saturated sand, the energy transfer to the target was significantly increased as compared to that for the cases with dryer sand. For the prairie soil, with moisture content varying between 5 and 20 percent, it was observed that the energy transfer increased considerably with increasing soil water content. Energy transfer increased markedly with decreased distance between the soil surface and the target while the transfer of energy increased to a maximum then diminished to nothing with a rising degree of soil overburden.

Fourney et al. (2005) performed small scale experiments, using 203 mg, 609 mg, or 3.3 g explosive charges buried in partially saturated, poorly graded, sand and targets consisting of metal or plexiglass plates and measured the momentum transfer to the plates using high speed video. These tests were performed in order to support a related effort involving 2.3 and 4.5 kg explosive scale tests (Taylor, Skaggs, and Gault, 2005), to support the development of computational tools for the prediction of mine blast effects (Wardlaw et al., 2003; Szymczak, 2005), and to better understand relationships between effects observed at different experimental scales.

Once appropriate corrections were made and appropriate scaling rules were applied,

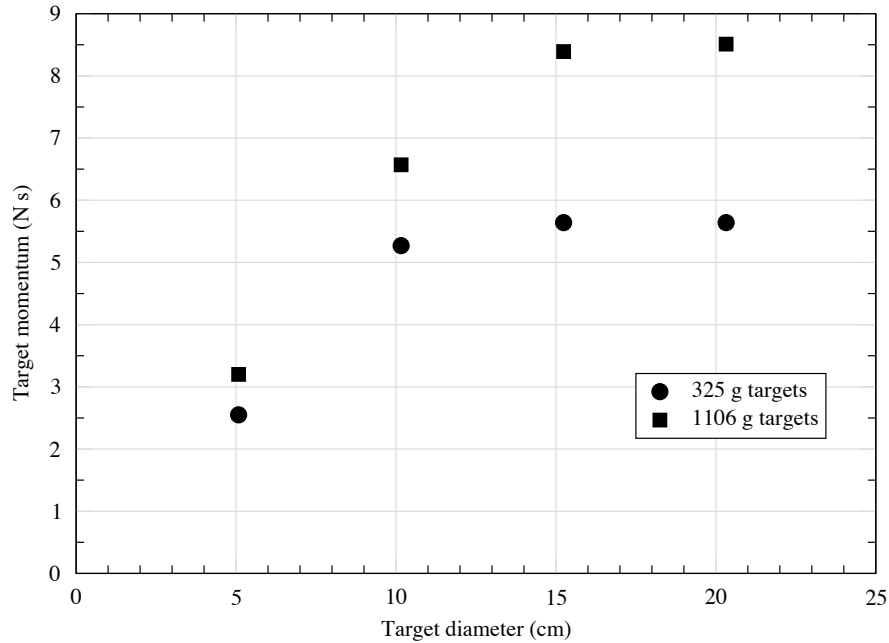


Figure 1.5: Variation of momentum transferred to round plates as a function of plate diameter and plate mass (adapted from Fourney et al. (2005))

it was determined that the momentum transfer results from the small scale tests were proportional to those from the larger, 4.54 kg, tests. The authors also examined, using small scale tests, the effect of momentum transferred to round plates with variable plate surface area and mass. It was observed that momentum transfer increased with increasing surface area and with increasing mass (Figure 1.5).

Szymczak (2005) performed computations and compared them with some of the small and large scale experimental results described, respectively, by Fourney et al. (2005) and Taylor, Skaggs, and Gault (2005). The computations were performed, with the assumption that the partially saturated sand behaved as a Bingham plastic, by means of an incompressible visco-plastic constitutive treatment for the sand.

Constitutive model parameters for the sand had previously been estimated, based on fits (Szymczak and Rogers, 2000) to data from quasi-two dimensional experiments meant to investigate channeling behavior in sand submerged below water (Fourney, Taylor, and Robeson, 1999). The displacement vs. time histories from Szymczak's computations com-

pared fairly closely with the small and the large scale experimental results for ratios of target stand-off distance to explosive depth of burial less than approximately 1.5.

Foedinger and Caiazzo (2006) tested explosive buried in wet and dry clayey sand. It was observed that the initial velocity of the upper boundary of the expanding dome of soil above the explosive was higher, for an intermediate depth of burial, for the wet soil than it was for the dry soil. For a greater depth of burial, the initial velocities were the same for both soil states. Zakrisson et al. (2008) looked at the loading on a relatively massive rigid metal plate from an explosive that was buried in wet and dry sand. They observed that the wet sand imparted more momentum to the plate than the dry sand did.

Genson (2006) performed experiments, using 460, 609, and 636 mg explosive charges buried in partially saturated poorly graded sand, to investigate the influence of various factors on the amount of momentum transferred from the buried explosive to solid structures. The factors that were varied included depth of explosive burial, distance from the soil surface to the bottom of the target structure, and the shape of the bottom of the structure (Figure 1.6).

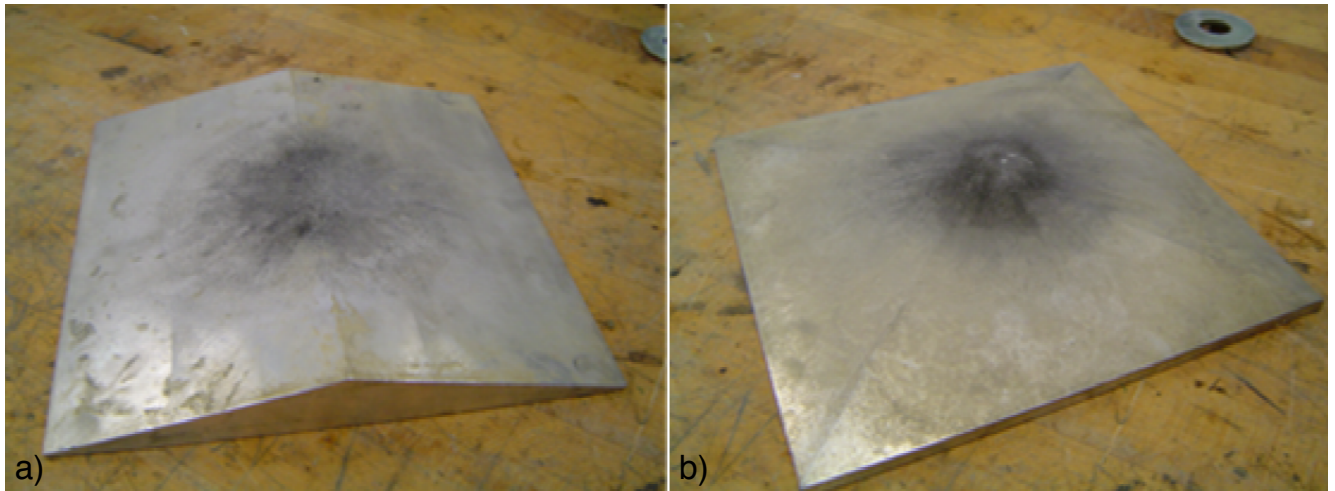


Figure 1.6: Bottom surfaces of rigid target structures (from Genson (2006)). a) Bihedral. b) Pyramidal.

The responses of several relatively rigid structures were examined including a flat plate,

downwardly convex pyramids with different angles between the faces, downwardly convex bihedra with various angles between the faces, and flat plates with grids of multiple downwardly convex pyramids on their bottom faces. Momentum transfer was, in general, found to be a decreasing function of increasing depth of explosive burial and increasing vertical distance between structure and the explosive. The excitation of the downwardly pyramidal and dihedral structures was less pronounced than that of the flat plate.

The momentum transferred to the dihedra was generally less than that transferred to the flat plate; the reduction became less marked as the initial distance between the explosive and the bottom of the structure increased. When the target plates laid directly on the surface of the soil, less momentum was transferred to the structures with pyramidal faces than to those with bihedral faces. For distances between structure and explosive greater than this, however, there was little difference between the pyramidal and the bihedral faces. Finally, the structures with pyramidal arrays on their bottom faces, when placed directly on the soil surface, underwent less momentum transfer than did the flat plates. At elevated placements, the momentum transfer was similar to that to the flat plates.

Neuberger, Peles, and Rittel (2007) performed a combination of experiment and computation in order to examine the scaling of flat plate deformation caused by excitation from large explosive charges flush buried in dry sand. Their computations were performed using the arbitrary Lagrangian Eulerian technique and agreed closely with experiment. The dry sand was modeled by means of a generalized Mohr- Coulomb model. The computational and experimental results showed that the blast response of targets to detonation of large explosives flush buried in dry sand followed a scaling relation.

Williams et al. (2008) used hybrid elastic-plastic soil models to predict the response of a flat target to the blast from a shallow-buried explosive buried in dry sand, clayey sand, and clay. The computational results were such that the impulse imparted to the target increased with decreasing soil compressibility and yield strength. Anderson et al. (2010, 2011) performed blast tests involving explosive shallow buried in sand that was emplaced

at three different levels of water content - 7, 14, and 22 percent. It was found that the peak momentum imparted to a flat, rigid target increased with increasing water content.

Deshpande et al. (2009) demonstrated a computational approach toward integration of the regimes of rapid and slow granular flow. The slow flow regime was essentially described, for the case of their example calculations, as the sum of a granular micro-inertial dynamic contribution and a more traditional contribution given by the prescription of a bulk modulus for volumetric behavior and of zero strength in shear once a critical bulk density was met or exceeded. If the bulk density becomes less than a critical value, then the behavior follows the rapid flow regime, which is a function solely of the granular micro-inertia.

This approach was used to examine the one-dimensional dynamic behavior of a slug of sand and it was calculated that the momentum transmitted to a target was dependent upon the initial density of the sand but not upon the coefficient of restitution used for the modeling of the collisions between individual grains. Calculations were also performed in which the explosive spherical behavior of wet and dry sand were contrasted. These computations resulted in clumping of the wet sand, as opposed to dispersion of the dry sand. The clumping was found to be attributable to the relatively higher initial bulk modulus of the wet sand.

Ehrgott et al. (2011a) combined carefully constructed test beds with known density, known water content and known associated soil mechanical properties to measure rigid target momentum, soil crater formation, and above-ground pressure generation. The target momentum was measured using a novel impulse measurement device which consisted of a 914 mm diameter hardened steel plate attached to a piston device. The soils were characterized by the U.S. Army Engineer Research and Development Center in a specially constructed high pressure triaxial test cell.

It was found that crater size increased and side angle decreased as the medium went from clay to intermediate soil to sand - as did measured target impulse from the buried charge. Interestingly, the air blast pressure measurements showed a reverse trend with the

air blast impulse occurring in the dry sand and the smallest air blast impulse occurring in the wet clay. The research also showed an increase in focusing or air blast pressure in the intermediate silty sand and wet clay compared to the dry sand, indicating an improved lateral confinement due to soil properties.

Chapter 2

Overview of the present work

2.1 Research objectives

Although, as was shown in Chapter 1.3, air blast and ground shock phenomena have been very thoroughly researched and tools are available for predicting their effects, many details regarding the physics associated with loading from buried land mines are not nearly so well understood. This work, will integrate a combination of experiment, computation, and theory to more carefully identify and examine the determinants of mine blast loading on structures.

Once this has been accomplished, these findings will be applied to establish a methodology for prediction of the response of various structures to loading from explosive charges that are buried in several types of soil with differing initial water content and initial density and to validate these methods against experimental results. A review of previous work has shown that there has not, to date, been an intensive examination of momentum transfer from buried explosives to structures that involves the careful definition and independent characterization of soil properties for numerous emplacement conditions and soil types.

An investigation will be performed, with independent testing of the constitutive behavior of the soils used in the work, and which will combine experiment and computation in order to better understand the extents to which such soil properties as yield surface, hydrostat (pressure-volume relation), and initial density influence the loading on structures. The nature of gas-particle flow will be investigated. This type of flow could later prove to, in some cases, engender significant blast effects by virtue of the erosion and flow of the ejecta from craters. Finally, the methodology established in this report will be used to predict the momentum transfer to several structures subjected to varied loading conditions.

2.2 Thesis outline

In Chapter 3 the rheology of sand-like, small glass particles in a fluidized bed will be examined. This might, in the future, prove to be a flow regime that is relevant to crater erosion phenomena. Conservation relations and an Eulerian finite difference treatment will be used to predict the behavior of the fluidized particles in a Couette flow regime. Next, experimental results will be used to validate the solution technique and then, finally, parametric studies will be performed using the finite element solver in order to examine the way that particle shape and particle diameter affect the rheology of the fluidized bed.

Next, in Chapter 4 there is an examination of the mechanics of momentum transfer from explosive charges buried in dry poorly graded sand, partially saturated poorly graded sand, and water to rigid plates. This is accomplished by performing two computational factorial studies - one that compares the behavior of wet sand and dry sand and another that compares the behaviors of wet sand and water - to identify and rank the importance, relative to the momentum transfer to rigid structures, of the various constitutive behaviors of the beds in which the explosives are placed. The results of the factorial studies and computations are analyzed and provide insight into reasons for the relative influence of the constitutive behaviors - yield surface, Poisson ratio, pressure-volume relation, and density - on momentum transfer.

Chapter 5, involves the investigation of momentum transfer to plates by means of explosive buried in a variety of media - including water, poorly graded sand, silty sand, and clayey sand - and buried in a number of emplacement conditions - in other words, buried in a number of combinations of water content and density. Experimental and computational results are compared for a new parametric relation between momentum transfer to round plates and initial containing medium air filled void volume fraction. Computations are then performed in order to determine the relative sensitivities of momentum transfer to the containing medium's hydrostatic behavior, yield behavior, and initial bulk density. Finally, based on theory and computational results, there is an examination of the reasons for the

observed sensitivities.

Chapter 6 is an analysis of experimental results and computational predictions for more complex loadings to structures with various geometries. This study involves the momentum transfer from explosive buried in partially saturated sand to flat targets, targets with bottom surfaces that are downwardly convex, and targets with bottom surfaces that are downwardly concave. There is also an analysis of the effect of varying explosive charge lateral position beneath the target. Finally, Chapter 7 contains a summary of the research findings from this work as well as an outline of future research directions.

Chapter 3

Erosion phenomena: Couette flow in a fluidized bed

3.1 Overview of fluidized bed flow investigation

Multi-phase flow has been investigated and analyzed for treatment of problems with flow regimes that exhibit some similarities to the mine blast soil-air mixture. These analyses were performed for application in fields as diverse as coal fraction separation (Zhao and Wei, 2000), chemical processing (Anjaneyulu and Khakhar, 1995), and the study of emissions of granular solids - in various concentrations in mixture with air and water - from volcanoes (Dartevelle, 2004). Some of the seminal theoretical development in the field of multiphase flow was published by Anderson and Jackson (1967) for the description of domain-averaged flow of solid particle-gas systems and by Ishii, originally in 1975, and later significantly updated and expanded (Ishii and Hibiki, 2006) for the description of gas-liquid flows.

For the purposes of the present study, the constant particle viscosity methodology (Enwald et al., 1996; Johansson et al., 2006) was modified appropriately, validated by use of experimental results reported by Anjaneyulu and Khakhar (1995) then subsequently used in conjunction with soil parameters from the data assembled and presented by Cho et al. (2006) in order to put forward a first step toward the development of a methodology for more appropriately treating a portion the soil-air rheology that may be applicable to mine blast. The tools developed during this project will hopefully represent a step toward a better understanding and quantification of mine blast soil ejecta.

3.2 The gas-particle flow model

Following the development presented in Johansson et al. (2006), the governing continuity and momentum balance equations, developed by Ishii and Hibiki (2006), that were used for the particle-air flow are

$$\frac{\partial}{\partial t}(\epsilon_g \rho_g) + \nabla \cdot (\epsilon_g \rho_g \mathbf{U}_g) = 0 \quad (3.1)$$

$$\frac{\partial}{\partial t}(\epsilon_g \rho_g \mathbf{U}_g) + \nabla \cdot (\epsilon_g \rho_g \mathbf{U}_g \mathbf{U}_g) = \nabla \cdot \epsilon_g \boldsymbol{\tau}_g + \epsilon_g \rho_g \mathbf{g} - \epsilon_g \nabla P - \beta(\mathbf{U}_g - \mathbf{U}_p) \quad (3.2)$$

for the gaseous, air, component (denoted by the subscript g), and

$$\frac{\partial}{\partial t}(\epsilon_p \rho_p) + \nabla \cdot (\epsilon_p \rho_p \mathbf{U}_p) = 0 \quad (3.3)$$

$$\frac{\partial}{\partial t}(\epsilon_p \rho_p \mathbf{U}_p) + \nabla \cdot (\epsilon_p \rho_p \mathbf{U}_p \mathbf{U}_p) = \nabla \cdot \epsilon_p \boldsymbol{\tau}_p + \epsilon_p \rho_p \mathbf{g} - \epsilon_g \nabla P - \nabla P_p + \beta(\mathbf{U}_g - \mathbf{U}_p) \quad (3.4)$$

for the particulate components. ϵ is the volume fraction, ρ is the density, \mathbf{U} is the velocity vector, $\boldsymbol{\tau}$ is the viscous stress tensor, \mathbf{g} is the gravitational acceleration vector, P is the static pressure, β is the interphase momentum transfer coefficient and P_p is an estimate of the particle-particle interaction force. The total volume fraction is equal to 1, that is to say that $\epsilon_g + \epsilon_p = 1$.

The viscous shear stress tensor was modeled, for each phase, by

$$\boldsymbol{\tau}_k = (\xi_k - \frac{2}{3}\mu_k)(\nabla \cdot \mathbf{U}_k)\mathbf{I} + 2\mu_k \mathbf{S}_k \quad (3.5)$$

where ξ_k represents bulk viscosity, μ_k is the dynamic viscosity, and \mathbf{S}_k is the rate of deformation tensor

$$\mathbf{S}_k = \frac{1}{2}[\nabla \mathbf{U}_k + (\nabla \mathbf{U}_k)^T] \quad (3.6)$$

The correlation for the interphase momentum transfer coefficient β that was used (van Wachem et al., 2001; Wen and Yu, 1966) was

$$\beta = \frac{3}{4} C_D \frac{(1 - \epsilon_p) \epsilon_p \rho_g |\mathbf{U}_g - \mathbf{U}_p|}{\phi d_p} (1 - \epsilon_p)^{-2.65} \quad (3.7)$$

where d_p is the mean particle diameter, ϕ is the particle sphericity, and C_D is the coefficient of drag for a single sphere. The correlation used for the single sphere drag coefficient C_D was (Rowe, 1961)

$$C_D = \begin{cases} \frac{24}{Re_p(1-\epsilon_p)} \{1 + 0.15[(1 - \epsilon_p) Re_p]^{0.687}\} & \text{if } (1 - \epsilon_p) Re_p < 1,000 \\ 0.44 & \text{if } (1 - \epsilon_p) Re_p \geq 1,000 \end{cases} \quad (3.8)$$

where Re_p is the particle Reynolds number

$$Re_p \equiv \frac{\phi d_p \rho_g |\mathbf{U}_g - \mathbf{U}_p|}{\mu_g}. \quad (3.9)$$

Finally, the scale of the particle-particle interaction force P_p was estimated by means of (Gidaspow and Ettehadieh, 1983)

$$\nabla P_p = G_0 e^{-c(\epsilon_g - \epsilon_{g,min})} \cdot \nabla \epsilon_p \quad (3.10)$$

where G_0 and c are empirically determined constants, ϵ_g is gas phase volume fraction, and $\epsilon_{g,min}$ is the smallest possible gas volume fraction. The viscosity of the particle phase was treated as a constant according to the so-called constant particle viscosity method (Johansson et al., 2006).

3.3 Model geometry

The geometry used in all cases is the geometry that was employed by Anjaneyulu and Khakhar (1995) in an experimental study of the rheological behavior of an air-glass bead fluidized bed (Fig. 3.1). A rotating cylinder imparts shear stress to an annular fluidized bed containing various mixtures of air and particles and the gross particle flow behavior is measured and deduced. Boundary conditions at the cylinder walls, are assumed to be no

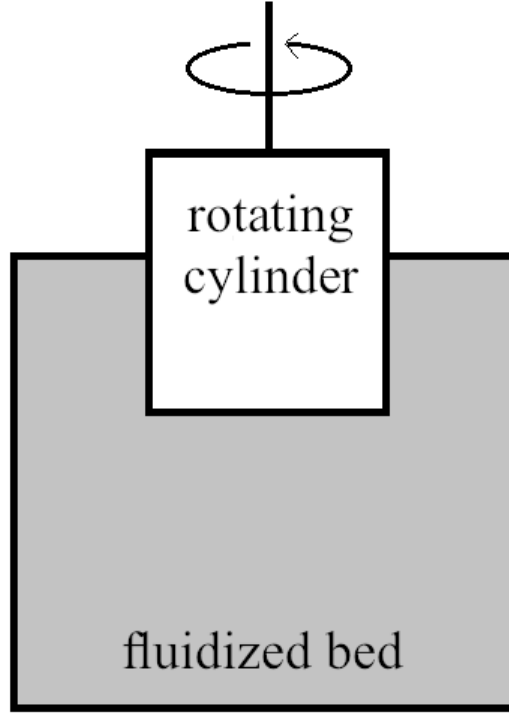


Figure 3.1: Simplified model geometry for analytical and numerical test cases, inner rotating cylinder radius = 6 mm, fluidized bed outer radius = 32.5 mm.

slip. The radius of the rotating cylinder was 6 mm; the outer radius of the bed was 32.5 mm. The cylinder rate of rotation was 5/6 revolutions/s.

3.4 Equations of motion for test cases

It was assumed, based on the reported experimental results (Anjaneyulu and Khakhar, 1995) that the flow was unidirectional azimuthal (θ -direction) flow. Based on the same findings it was also assumed that no slip boundary conditions could be applied and that there were no edge effects.

The continuity relations, Equations (3.1) and (3.3) vanish and, after some simplification, the fluid flow is defined using the following three relations:

$$-\rho_p \frac{u_{\theta,p}^2}{r} = G_0 e^{-c(\epsilon_g - \epsilon_{g,min})} \cdot \frac{\partial \epsilon_p}{\partial r} \quad (3.11)$$

$$\mu_g \left\{ \frac{\partial}{\partial r} \epsilon_g \left[\frac{1}{r} \frac{\partial}{\partial r} (r u_{\theta,g}) \right] \right\} - \beta (u_{\theta,g} - u_{\theta,p}) = 0 \quad (3.12)$$

$$\mu_p \left\{ \frac{\partial}{\partial r} \epsilon_p \left[\frac{1}{r} \frac{\partial}{\partial r} (r u_{\theta,p}) \right] \right\} + \beta (u_{\theta,g} - u_{\theta,p}) = 0. \quad (3.13)$$

3.5 Definition of boundary conditions

As stated before, it was demonstrated (Anjaneyulu and Khakhar, 1995) that there was no slip at the walls of the internal rotating cylinder or at the wall of the outer cylinder.

This leads to definition of the boundary conditions for the problem which are

$$u_{\theta,k}(r_i) = 2\pi r_i \Omega_0 \quad (3.14)$$

$$u_{\theta,k}(r_o) = 0 \quad (3.15)$$

where r_i , r_o , and Ω_0 are rotating cylinder radius, outer wall radius, and rotational speed of inner cylinder, respectively.

3.6 Physical properties for gas and particle phases

The experimental data from used in this work (Anjaneyulu and Khakhar, 1995) were those generated under minimum fluidization conditions, viz., under those conditions for which the pressure drop through the column matched the body force, from gravity, that was exerted on the material contained in the column. The choice for the value of ϵ_p was based on results reported in the literature for minimum fluidization conditions. For minimum fluidization, the particle volume fraction ϵ_p should be at least 0.54 (Olowson and Almstedt, 1991). For nearly spherical particles, ϵ_p should be approximately 0.55-0.60, decreasing a bit with increasing particle size (McCabe et al., 2001).

Based on the experimental conditions and the geometry, a scale analysis was performed on Equation 3.11. Order of magnitude estimates of the various quantities in Equation 3.11

are presented in Table 3.1.

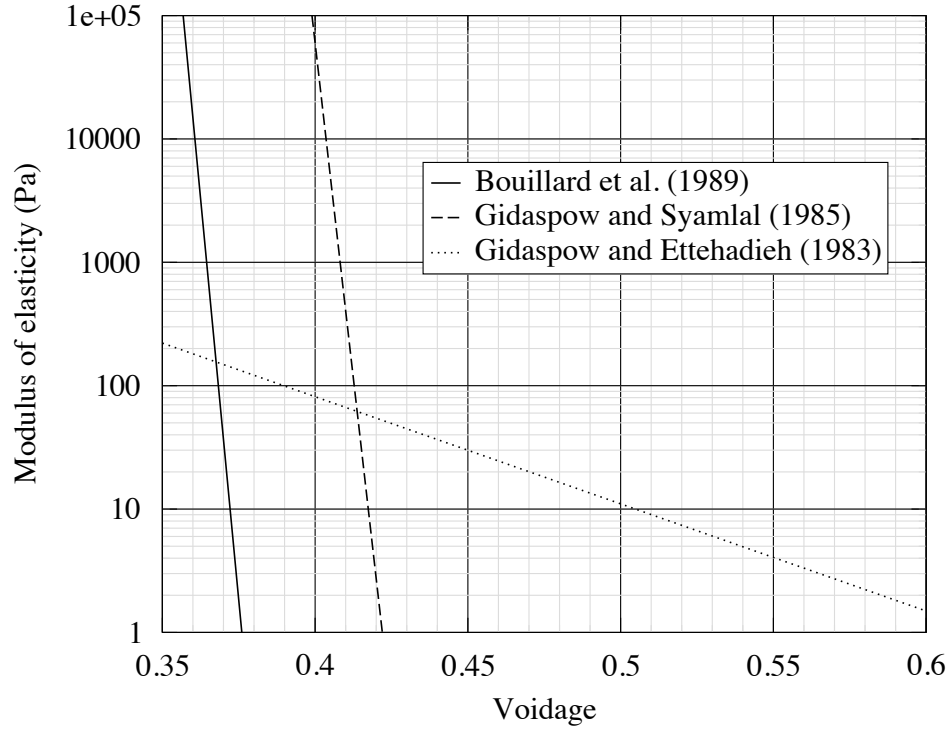


Figure 3.2: Correlations for $G_0 \exp[-c(\epsilon_{p,max} - \epsilon_p)]$. Note that voidage is the gas-phase gas fraction ϵ_g and is equal to $1 - \epsilon_p$ (adapted from Enwald et al. (1996)).

Using these estimates, it was determined that the radial variation of the particle volume fraction $\Delta\epsilon_p$ across the bed was of the order of 10^{-3} , whereas the order of magnitude of ϵ_p was 10^{-1} . The scale of $G_0 \exp[-c(\epsilon_{p,max} - \epsilon_p)]$ was based on the results of Gidaspow and Ettehadieh (1983) as presented in Enwald et al. (1996) (Figure 3.2). The results from Gidaspow and Ettehadieh were chosen rather than those from Gidaspow and Syamlal (1985) or Bouillard et al. (1989) since only the results reported in Gidaspow and Ettehadieh yielded elastic moduli for volume fractions assumed relevant to the current problem. Values for other physical properties associated with the flow problem test case are given in Table 3.2.

Table 3.1: Parameter orders of magnitude for the estimate of radial variation of particle volume fraction ϵ_p .

Parameter	Scale	Units
ρ	1×10^3	kg/m ³
u^2	1×10^{-4}	(m/s) ²
R	1×10^{-2}	m
$G_0 \exp[-c(\epsilon_{p,max} - \epsilon_p)]$	1×10^2	N/m ²
Δr	1×10^{-2}	m
ϵ_p and $\epsilon_{p,max}$	1×10^{-1}	dimensionless

Table 3.2: Physical properties of glass beads and air.

Property	Air (at 20 °C)	Glass beads	Units
Sphericity ϕ	—	1.00	dimensionless
Mean particle diameter d_p	—	9.00×10^{-4}	m
Viscosity μ	1.20	—	Pa s
Density ρ	1.88×10^{-5}	2.50×10^3	kg/m ³
Volume fraction ϵ	4.60×10^{-1}	5.40×10^{-1}	dimensionless

3.7 Discretization of equations of motion

Given the determination, via scale analysis, that ϵ_p was relatively constant across the radial position of the bed, expansion and rearrangement of Equations 3.12 and 3.13 yields the two relations that were used for the discretization.

$$\frac{\partial^2 u_{\theta,g}}{\partial r^2} + \frac{1}{r} \frac{\partial u_{\theta,g}}{\partial r} - \left(\frac{1}{r^2} + \frac{\beta}{\epsilon_g \mu_g} \right) u_{\theta,g} + \frac{\beta}{\epsilon_g \mu_g} u_{\theta,p} = 0 \quad (3.16)$$

$$\frac{\partial^2 u_{\theta,p}}{\partial r^2} + \frac{1}{r} \frac{\partial u_{\theta,p}}{\partial r} - \left(\frac{1}{r^2} + \frac{\beta}{\epsilon_p \mu_p} \right) u_{\theta,p} + \frac{\beta}{\epsilon_p \mu_p} u_{\theta,g} = 0 \quad (3.17)$$

First and second derivatives were approximated using central differences in order to limit the truncation error to be of the order of $(\Delta r)^2$.

$$\frac{\partial^2 u_{\theta,g}}{\partial r^2} = \frac{u_{\theta,g,i+1} - 2u_{\theta,g,i} + u_{\theta,g,i-1}}{(\Delta r)^2} + O[(\Delta r)^2] \quad (3.18)$$

$$\frac{\partial^2 u_{\theta,p}}{\partial r^2} = \frac{u_{\theta,p,i+1} - 2u_{\theta,p,i} + u_{\theta,p,i-1}}{(\Delta r)^2} + O[(\Delta r)^2] \quad (3.19)$$

$$\frac{\partial u_{\theta,g}}{\partial r} = \frac{u_{\theta,g,i+1} - u_{\theta,g,i-1}}{2(\Delta r)} + O[(\Delta r)^2] \quad (3.20)$$

$$\frac{\partial u_{\theta,p}}{\partial r} = \frac{u_{\theta,p,i+1} - u_{\theta,p,i-1}}{2(\Delta r)} + O[(\Delta r)^2] \quad (3.21)$$

Substitution of these expressions for the derivatives into Equations 3.16 and 3.17 led, after some rearrangement, to the discretized equations that were implemented in the code:

$$u_{\theta,g,i} = K_1 u_{\theta,g,i+1} + K_2 u_{\theta,g,i-1} + K_3 u_{\theta,g,i} \quad (3.22)$$

$$u_{\theta,p,i} = K_4 u_{\theta,p,i+1} + K_5 u_{\theta,p,i-1} + K_6 u_{\theta,p,i} \quad (3.23)$$

where $K_1 - K_6$ are coefficients that are combinations of the various factors and parameters in Equations 3.16 - 3.21 that depend upon the values of the radial position as well as upon the particle and air velocities.

3.8 Solution method

The Gauss-Seidel iteration method was used for the numerical solution of the flow equations, with the boundary conditions for the particle and gas velocities at r_i and r_o enforced by constraint of the velocity values to constant values at these radial locations.

3.9 Comparison of numerical and analytical results

The accuracy of the flow problem solution method was investigated by comparing numerical results from the code with the analytical solution for the single component, Newtonian

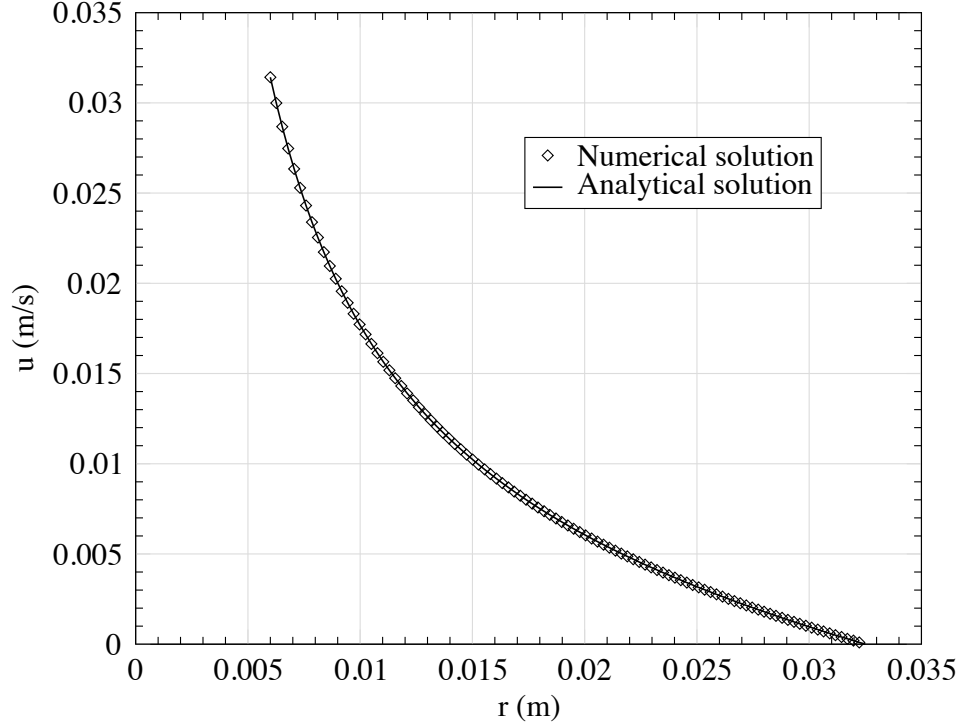


Figure 3.3: Comparison of numerical and analytical solutions to the single component Newtonian flow problem.

viscosity problem. The problem statement, for this case, is

$$\mu \left\{ \frac{\partial}{\partial r} \left[\frac{1}{r} \frac{\partial}{\partial r} (ru_{\theta}) \right] \right\} = 0 \quad (3.24)$$

$$u_{\theta}(r_i) = 2\pi r_i \Omega_0 \quad (3.25)$$

$$u_{\theta}(r_o) = 0 \quad (3.26)$$

with the analytical solution

$$u_{\theta}(r) = \frac{\Omega_0 \kappa r_o}{\left(\kappa - \frac{1}{\kappa}\right)} \left(\frac{r}{r_o} - \frac{r_o}{r} \right) \quad (3.27)$$

where $\kappa = r_i/r_o$.

The analytical and numerical solutions to this problem are compared in Figure 3.3. It can be seen that the numerical results very closely matched the analytical solution. It is noteworthy that the radial velocity distribution is determined only by radial position, inner radius value, outer radius value, and angular velocity of inner cylinder and that flow behavior is not dependent on fluid intrinsic properties such as viscosity or density.

3.10 Parameter identification: air velocity distribution

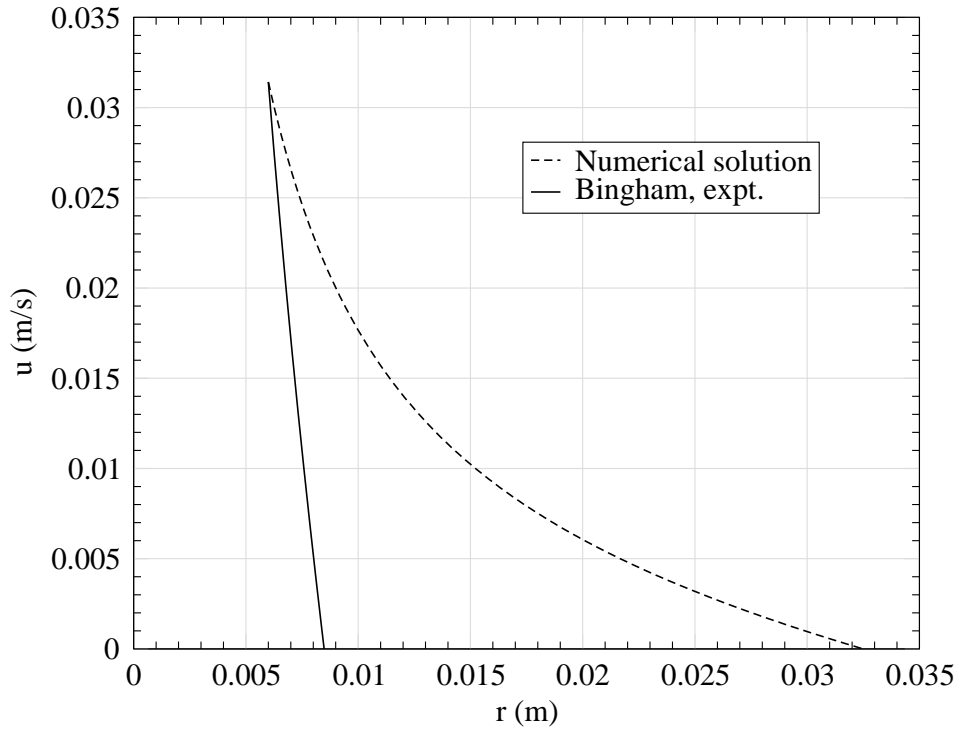


Figure 3.4: Comparison of experimental results with initial numerical solution derived with air velocity calculated using Equations 3.22 and 3.23.

As a result of the nature of the algorithm used to solve Equations 3.22 and 3.23, it was found that the solutions for both the air and particle phases converged identically - independent of the input values for air or particle viscosities, for particle sphericity, for particle diameter, and for air density - to the analytical solution represented by Equation 3.28 and shown in Fig. 3.3. This was found to be a result, during solution convergence, of

the tendency of the air and particle velocities to converge toward one another. This caused the scale of the coupling coefficients β_i to grow large and forced the velocity distributions for the two components to completely converge to one another. This result did not match the Bingham plastic experimental results as modeled and reported (Anjaneyulu and Khakhar, 1995) (cf. Figure 3.4).

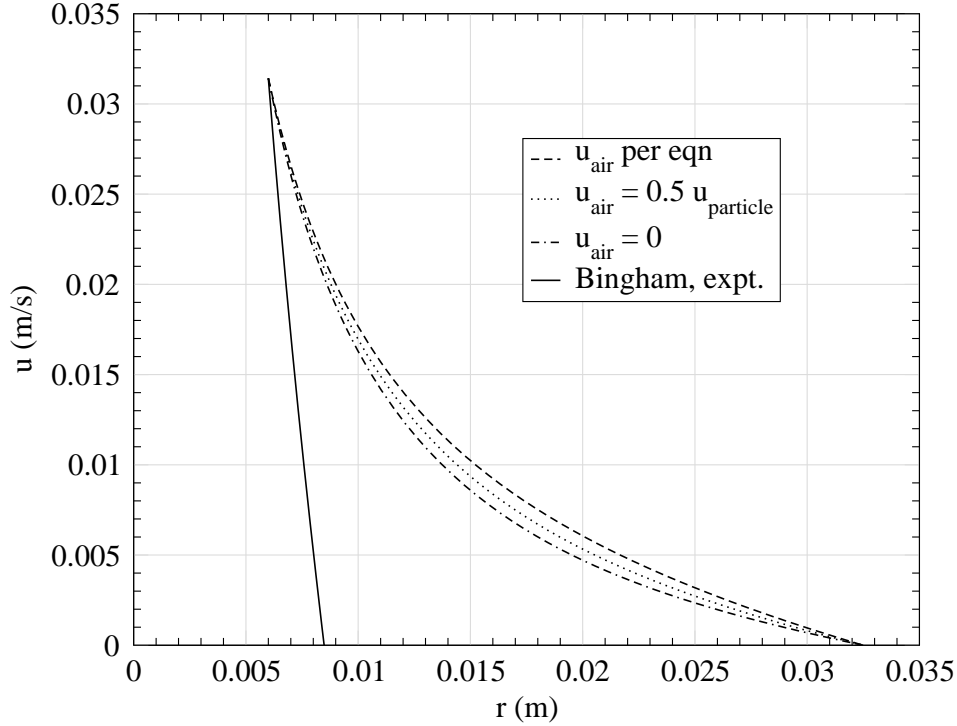


Figure 3.5: Effect of decreasing the air-phase velocity for the case of particle viscosity $\mu_p = 1.0$ Pa s.

In an effort to better determine the velocity distributions without completely revamping the solution algorithm, the values for the air velocity were constrained to be multiples of the velocities of the solid fraction, viz., $u_{\theta,g,i} = K u_{g,p,i}$, where K is a constant. The results for $K > 1$, i.e., for air velocity greater than particle velocity did not, in general, converge to yield any physically plausible results. Neither did the solutions for $K=1$.

Some results for various values of $K < 1$ are shown, in Figures 3.5 and 3.6 for particle viscosity values set to 1.0 and 0.01 Pa S. For the case of particle viscosity set to 1.0 Pa s

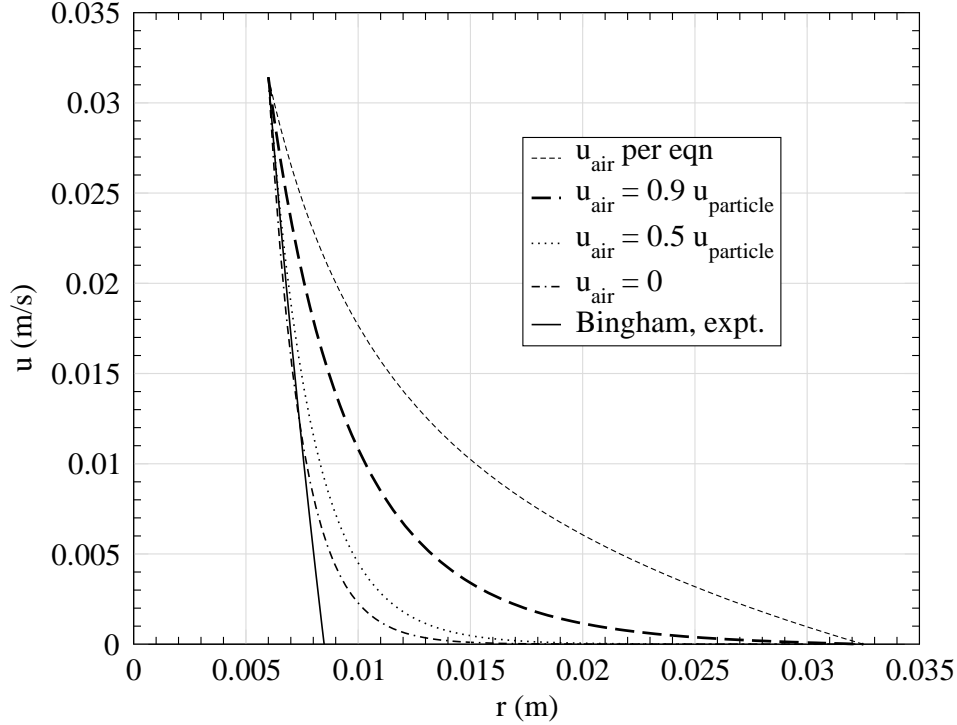


Figure 3.6: Effect of decreasing the air-phase velocity for the case of particle viscosity $\mu_p = 0.01$ Pa s. The particle velocity distribution appears to approach the experimentally determined velocity distribution.

(Fig. 3.5), it can be seen that, as K decreases from 0.9 to 0.0, there is moderate movement toward the experimental results. For the case of particle viscosity set to 0.01 Pa s (Fig. 3.6), it can be seen that as K decreases toward a value of 0.0, the particle velocity distribution seems to fairly closely converge to the experimental result.

Although, the results appeared to converge toward the experimental result, more work needs to be done in order to be sure that the particle velocity distributions approach each other as a result of the physics rather than simply as a result of the mathematical behavior of the current model. It is not, at this point, clear that the azimuthal air velocity, in this physical situation, would necessarily tend toward 0 or even that it would necessarily be lower than the particle velocity. To this end, future investigation will be conducted and will involve the numerical solution of Equations 3.16 and 3.17 using other discretization schemes. For now, however, the behavior of the model will be investigated with K , and

thus the azimuthal air velocity, set to 0.0.

3.11 Parameter identification: particle velocity

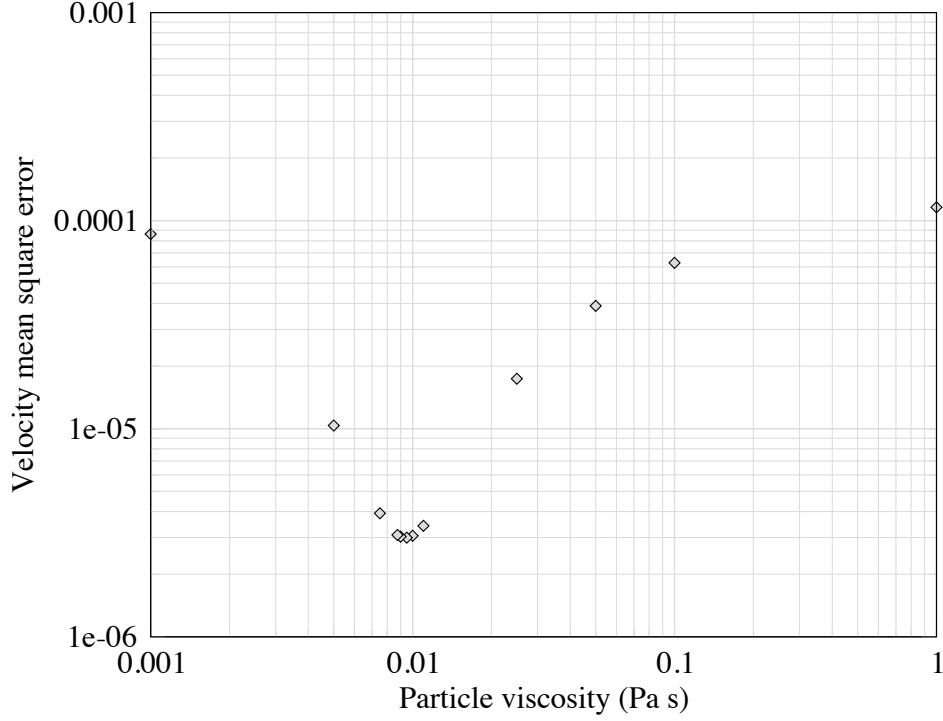


Figure 3.7: Material identification for the best value of particle viscosity based on mean-square error between experiment and model. The best value of particle viscosity was about 0.0095 Pa s.

A statistical technique was employed to determine the value for particle viscosity that would enable the numerical solution to most closely match, using the measure of mean square difference from the experimental results. Mean square error (MSE) was calculated as

$$MSE = \frac{\sum_{j=1}^m (u_{experimental,j} - u_{numerical,j})^2}{m} \quad (3.28)$$

where $u_{experimental,j}$ and $u_{numerical,j}$ are the experimentally reported and numerically calculated values of particle velocity, j is as used in the discretization, and $j=m$ is the value of

the radial position for which the value of the experimentally reported particle velocity is less than about 10% of its maximum value. The level of particle viscosity that allowed the numerical solution to most closely approach the experimentally determined solution was 0.0095 Pa s (Fig. 3.7).

3.12 Effect of grid spacing on solution

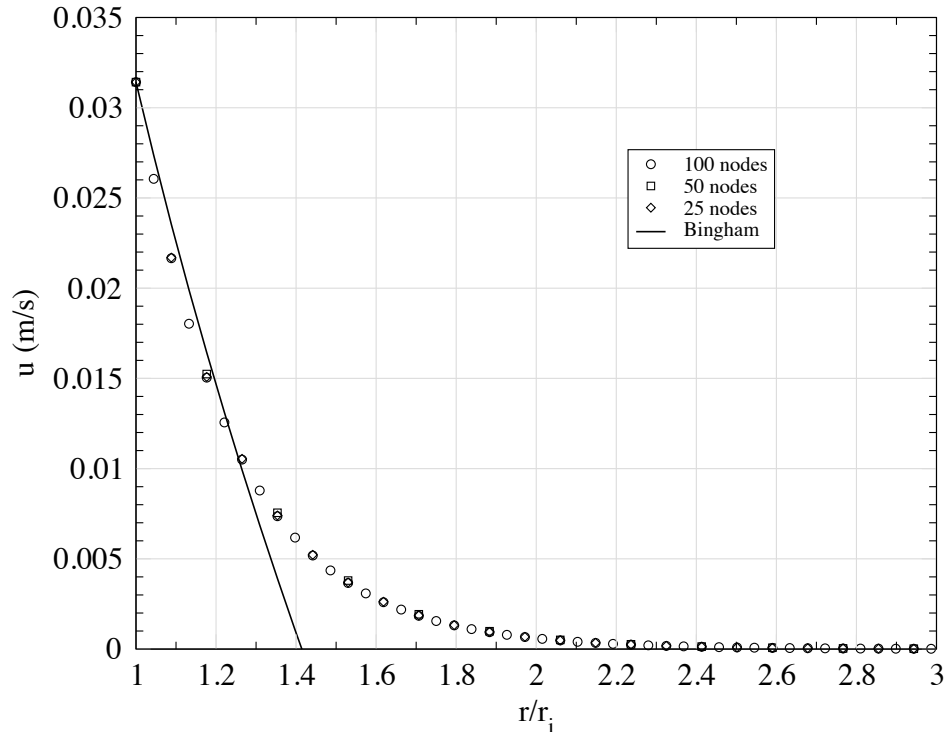


Figure 3.8: Comparison of numerical results for various mesh sizes versus experimental (Bingham plastic) results.

A comparison of solutions generated by means of different grid spacing is presented in Figure 3.8, for solutions involving 25, 50, and 100 grid points. It can be seen that similar convergence was achieved for all three levels of spacing between grid points and that all three regimes seemed to approach the experimental result in a similar fashion.

3.13 Iteration convergence

The convergence of the iterated solution was measured by means of the root mean square error (*RMSE*) between iterations according to

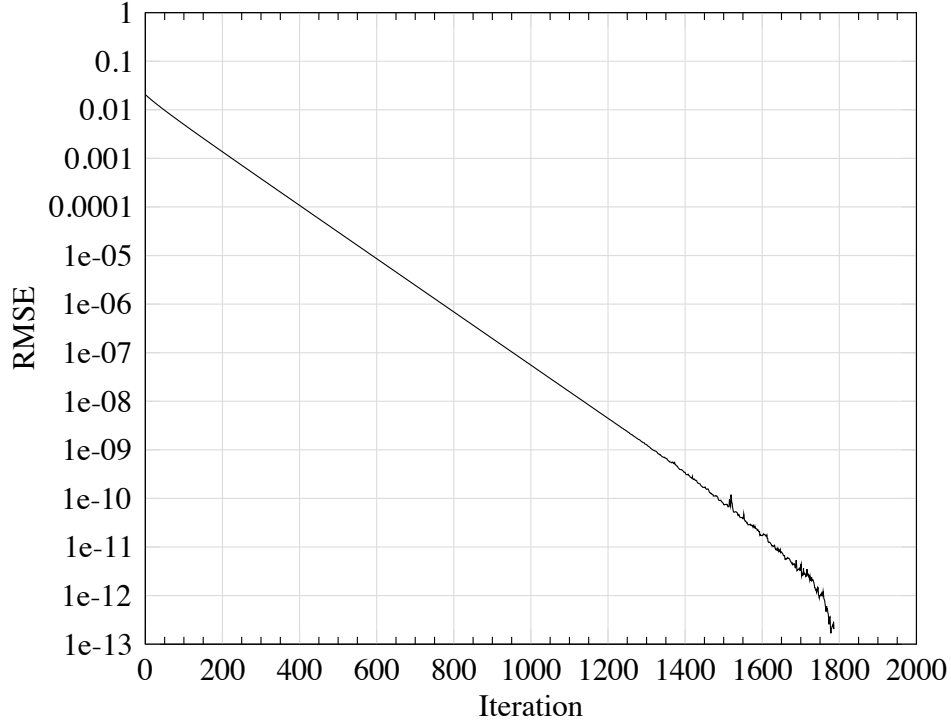


Figure 3.9: Convergence of iterations for the case of particle viscosity 0.0095 Pa s and 100 grid points.

$$RMSE = \sqrt{\frac{\sum_{i=1}^{n-1} (u_k - u_{k-1})^2}{n-1}} \quad (3.29)$$

where k refers to the k th iteration, i corresponds to the radial position r_i , and n corresponds to the maximum value of i , viz., the maximum radius is denoted, within the FORTRAN code as r_n . The iteration results are shown in Figure 3.9, where it can be seen that, for the case of 100 grid points and particle viscosity 0.0095 Pa s, excellent convergence appears to have occurred after about 400 iterations, i.e., at that point $RMSE < 1\%$.

3.14 Summary of experimental results

The experimental results (Anjaneyulu and Khakhar, 1995) were given in terms of the Bingham plastic parameters

$$\tau_{r\theta} = \begin{cases} \tau_y + \mu\dot{\gamma} & \text{for } \tau_{r\theta} > \tau_y \\ \tau_y & \text{for } \tau_{r\theta} \leq \tau_y \end{cases} \quad (3.30)$$

where $\dot{\gamma}$ is rate of deformation, $\tau_{r\theta}$ is shear stress, μ is viscosity, and τ_y is yield stress, viz., the level of shear stress below which no deformation will occur. The data are summarized in Table 3.3. $r_{interface}$ is defined as that value of the radius for which the shear stress falls to the level of τ_y for which the fluid begins to behave as a solid. Anjaneyulu and Khakhar (1995) estimated the Bingham plastic parameters using least squares techniques and noted that a significant difference was measured between the theoretical (Bingham model) and directly observed ratio of critical radius to inner cylinder radius, viz., the theoretical ratio was 1.41 whereas the ratio that was actually observed was 2.2.

Table 3.3: Summary of experimental data (Anjaneyulu and Khakhar, 1995).

Parameter	Value	Units
Particle diameter	9.00×10^{-4}	m
Inner cylinder radius	6.00×10^{-3}	m
Yield stress	4.50	Pa
Viscosity	2.00×10^{-1}	Pa s
Shear stress at inner wall	9.00	Pa s
Rotational velocity	8.33×10^{-1}	dimensionless
Theoretical $r_{interface}/r_i$	1.41	dimensionless
Actual $r_{interface}/r_i$	2.2	dimensionless

It should be noted that the computational model seemed to show results for this apparent disparity in critical radius that fit the experimental data better than did the Bingham model as evidenced by the approximate intersection point of the two phase computational result with the r/r_i axis (Fig. 3.10).

3.15 Flow effects resulting from variation of sphericity and particle diameter

Comparisons, using the numerical model developed for this work, of flow behavior resulting from variation of sphericity and particle size were performed based on particle properties

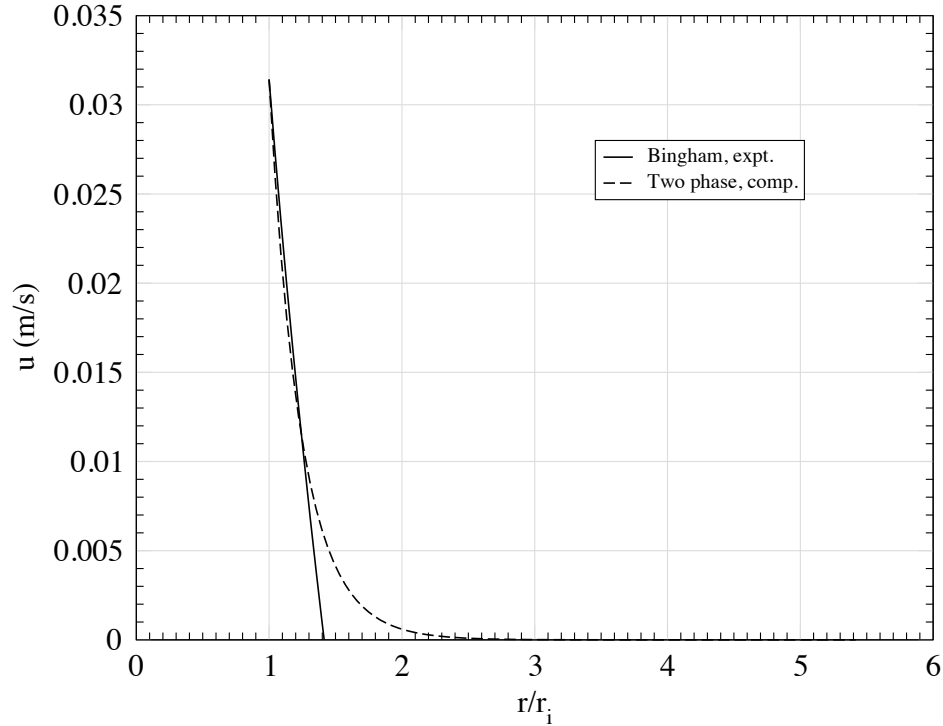


Figure 3.10: Comparison of experimental and numerical velocity distributions as a function of r/r_i . Note that the intersection of the CFD result with the r/r_i axis seemed to match the experimental results in Table 3.3 better than the Bingham fluid model.

reported in the literature (Cho et al., 2006). Sphericity is defined to be the diameter of the largest sphere that can be inscribed on a particle relative to the diameter of the smallest sphere that can be circumscribed on a particle.

The results of these calculations are shown in Figures 3.11 and 3.12. The calculations seemed to show that resistance to flow increased with decreasing particle size and that resistance to flow increased with decreasing sphericity. Figure 3.13, which shows results for several real materials also appears to exhibit the same trend of increasing flow resistance with decreasing particle size and sphericity. The reason for this can be deduced based on inspection of Equations 3.8, 3.9, and 3.10. As either sphericity or particle size decreases, the particle Reynolds number, coefficient of drag, and coupling factor will increase, thereby increasing the resistance to flow. It should not be tacitly concluded that this trend is correct simply based on the correlations. Future work will involve more extensive comparison of

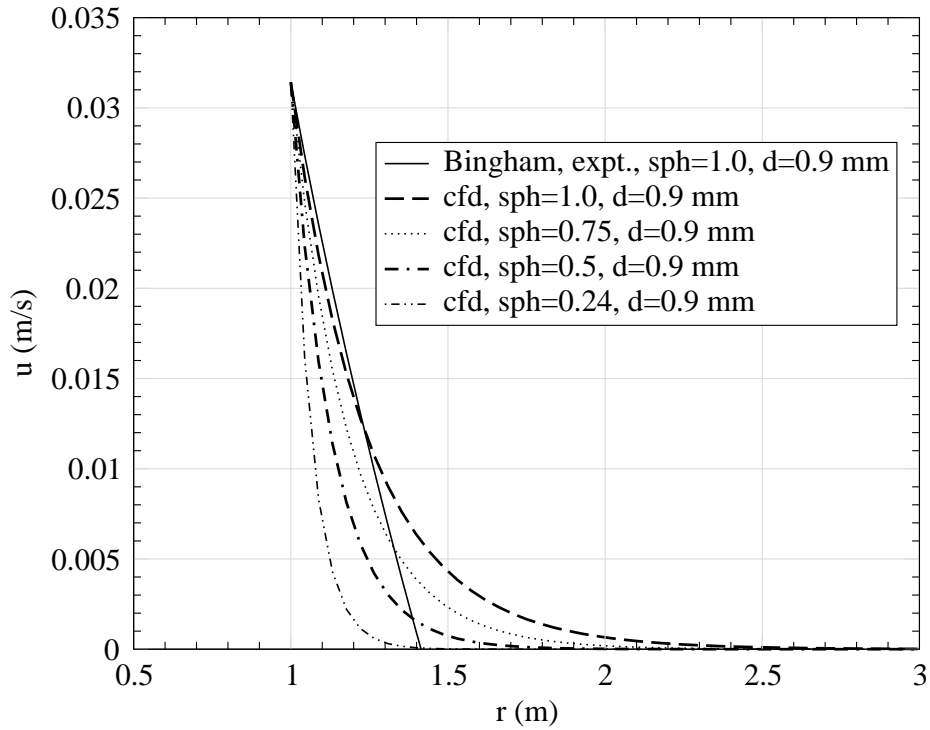


Figure 3.11: Effect of sphericity on velocity distribution and resistance to flow. As sphericity decreased, the calculated resistance to the flow increased.

these results with relevant experimental results, if they are available, in order to more fully verify whether the current model adequately predicts two phase fluid flow behavior.

Extensive searches for relevant comparison data have, to date, not been successful. If adequate data cannot be found, a different physical regime, for which more extensive validation data can be identified, will be modeled using the techniques developed for this work. It is not inconceivable that the effects of sphericity and average particle diameter might depend on the geometry and other characteristics of the flow regime and particle and fluid components.

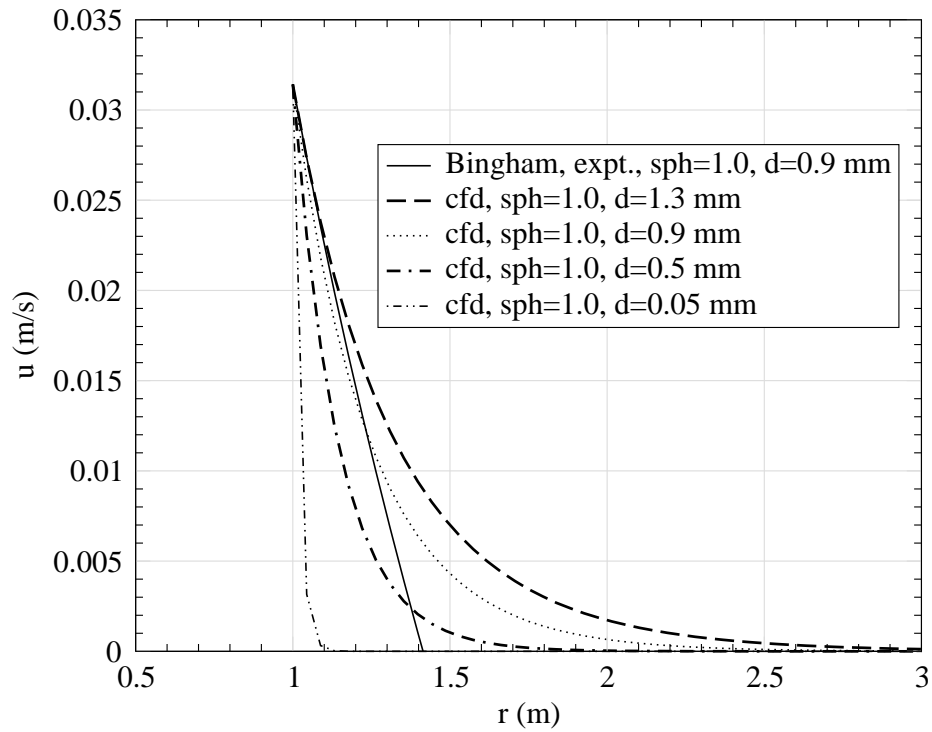


Figure 3.12: Effect of average particle diameter on velocity distribution and resistance to flow. As particle diameter decreased, calculated resistance to the flow increased.

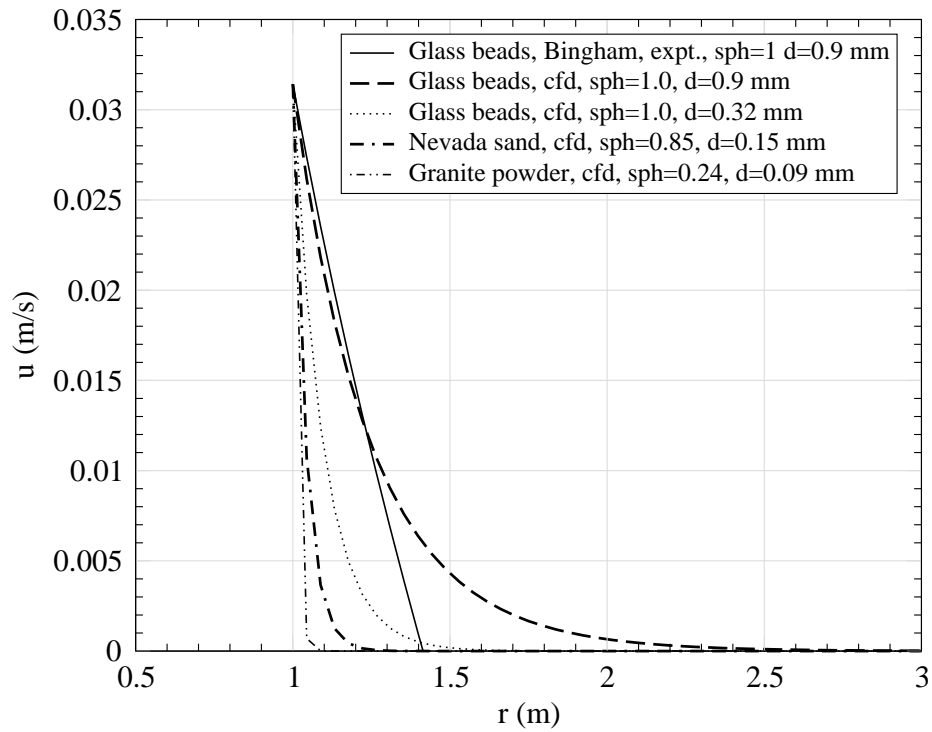


Figure 3.13: Effect of sphericity and average particle diameter, for several real materials, on velocity distribution and resistance to flow. As these parameters decreased, calculated resistance to the flow increased.

Chapter 4

The excitation of structures by explosive buried in sand and water

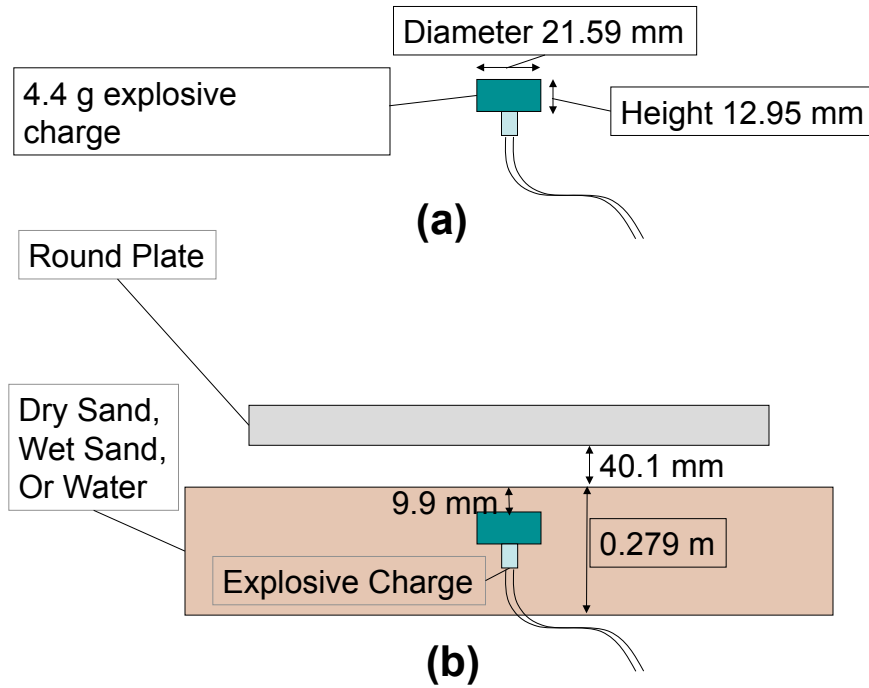


Figure 4.1: Experimental setup used (Fourney et al., 2010) to measure plate response to excitation from shallow buried explosive. a. Charge geometry. b. Test bed setup.

4.1 Overview of the sand- and water-based investigation

A combination of soil characterizations, computations and small-scale experiments were carefully analyzed in order to better understand the behavior of shallow-buried explosives. The constitutive behavior of the soils, developed based on the literature (Zimmerman et al., 1992), was determined using a combination of high pressure quasi-static tests and effective stress theory; the motion of rigid objects impacted by the material flow resulting from blast experiments was measured by use of high-speed digital video photography. Computations that simulated the blast experiments were performed by use of an arbitrary Lagrangian

Eulerian (ALE) treatment in a nonlinear finite element code. A factorial design approach was used to deduce the underlying mechanics of such systems. Using this approach, it was determined that, for water and for dry and partially saturated granular materials lower deviatoric yield strength was a key factor which caused sand or water to flow more readily thereby producing higher levels of momentum loading to bodies in close proximity to the buried explosive. It was also observed that higher bulk stiffness and mass density were moderately important factors although they were less significant than was the shear strength of the medium containing the explosive.

In the present work, experimental results from small-scale tests performed by Fourney et al. (2010) are compared with computational investigations in an attempt to gain insight into the physics behind the excitation of targets by shallow-buried explosives. The targets used for this work were disk-shaped, relatively rigid, aluminum targets and were excited by explosive buried in water, wet sand, or dry sand. First, there is a description of the experimental setup and computational approach including a detailed explanation of the constitutive behavior of the materials that were modeled.

Next, there is a description of the factorial experimental designs used to separate and compare the effects of some of the modeled bed substrate properties such as strength, density, and volumetric behavior. Subsequently there is an analysis of the results from the factorial computational experiments and an examination of possible explanations for some of the observed behaviors.

4.2 Experimental setup

Figure 4.1 illustrates the experimental setup used by Fourney et al. (2010) to measure the response of the rigid aluminum plates to the excitation of shallow buried explosive. The 4.4 g explosive charges used for this work were constructed using Detasheet C and an RP-87 detonator. The cylindrical charges were inserted into a bed of water, wet sand, or dry sand so that their top faces were 9.9 mm below the top surface of the bed. The bottom face of the aluminum target plate was located 40.1 mm above the top surface of the bed. The

plate was constructed of aluminum alloy 6061 with mass 10.05 kg and behaved essentially as a rigid body in its response to the loading from the buried explosive. The translation of the target was measured by tracking the motion of the target using high-speed video in order to determine the velocity history; the plate momentum could then be calculated by forming the product of the velocity and the mass.

4.3 Computational model

4.3.1 Computational techniques

Computations involving solid mechanics are often performed using a Lagrangian description of the problem with a computational mesh that moves with the solid material. Computations involving fluids are typically performed using an Eulerian description with a mesh that is fixed in space.

As a result of the nature of the current problem, which involves coupling between fluid and solid constituents, computations were here performed using an arbitrary Lagrangian-Eulerian (ALE) approach for the fluids and the very highly deformed soil coupled with a Lagrangian approach for the solid target. If a purely Lagrangian finite element approach had been used, this would have been an appropriate choice for the part of the problem involving only the solid target, but mesh distortion resulting from large displacements caused by the explosive, soil, and fluid motions would have caused the calculations to become unstable.

An Eulerian approach would have been a good choice of continuum treatment for the explosive and the fluid and soil components but the accuracy of the treatment of the solid target would have been sacrificed. The ALE approach used here offers the advantages of the moving mesh for handling the transport of mass, momentum, and energy for the fluid and soil constituents and can be easily coupled to the solid target, which is given a purely Lagrangian treatment.

Given a moving mesh such as the one that is used for the ALE computations, the conservation equations, neglecting thermal effects, for the transport of mass, momentum,

and energy, respectively, are

$$\frac{\partial \rho}{\partial t} = -\rho v_{i,i} - (v_i - u_i)\rho_{,i} \quad (4.1)$$

$$\rho \frac{\partial v_i}{\partial t} = t_{ji,j} + \rho b_i - \rho(v_i - u_i)v_{j,i} \quad (4.2)$$

$$\rho \frac{\partial e}{\partial t} = t_{ij}d_{ij} + \rho b_i v_i - \rho(v_i - u_i)e_{,i} \quad (4.3)$$

where ρ is the mass density, u_i the mesh velocity vector, v_i the material velocity vector, t_{ij} the stress tensor, b_i the body force vector, e the internal energy, d_{ij} the rate of deformation tensor, and where, for any quantity Q ,

$$Q_{,i} \equiv \frac{\partial Q}{\partial x_i} \quad (4.4)$$

Computations involving the explosive detonation products, air, and bed material either wet sand, dry sand, or water - were performed numerically by means of a multi-material ALE technique as implemented in the LS-DYNA explicit finite element solver. The behavior of the materials that were handled using the ALE method and the behavior of the aluminum target, treated by means of explicit Lagrangian finite element calculations, were coupled by means of a penalty method.

A cylindrical geometry was chosen for the computational domain. The mesh size for the ALE domain was varied by radial position in the circular plane of the domain. In the region closest to the center, the mesh size was approximately 1 mm; toward the outer radius of the domain, the mesh size gradually increased to about 0.1 m. The distance between nodes in the vertical, axial, direction was approximately 2 mm, but in the region of the domain initially filled with air this distance was gradually increased between this distance and 6.4 mm between the top of the target (in its initial position) and the top of the computational

domain. The axially symmetric computational domain contained approximately 20,000 elements.

The nominal mesh size of 1 mm that was in the central region of the ALE domain was well within the converged range of mesh sizes determined for computations previously used to investigate a problem involving the wet sand but with a 636 mg explosive charge that was an order of magnitude smaller than the 4.4 g charge used in the current study. It is assumed, therefore, that this mesh configuration was sufficiently converged to preclude spurious predictions based on mesh sensitivity.

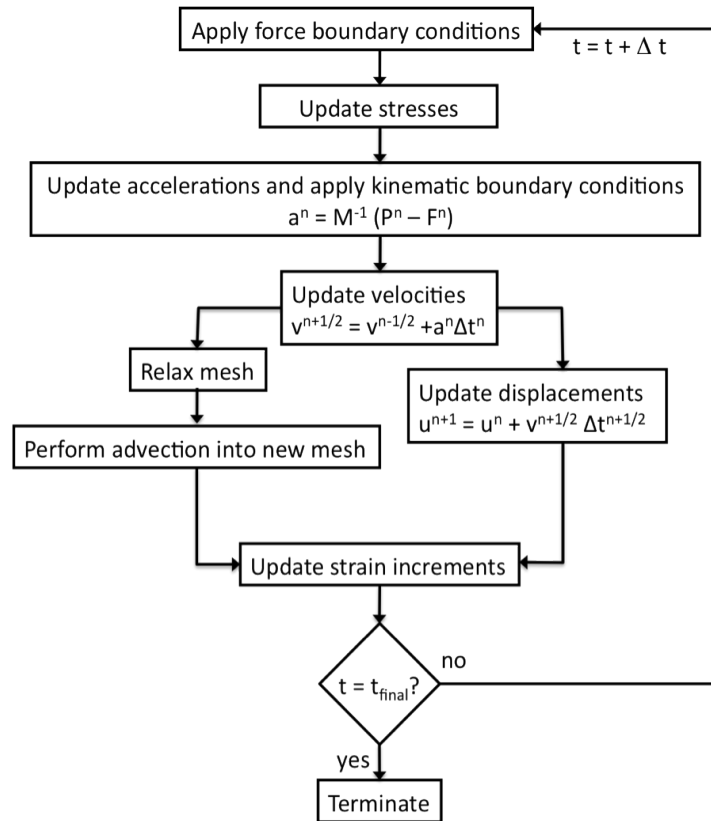


Figure 4.2: Flow chart of ALE time integration loop.

The ALE calculations were performed as follows. For each time step, a split operator technique was used to solve the transport equations for the mass, momentum, and energy

transport of the air, detonation product, and soil constituents of the problem (Fig. 4.2). In Fig. 4.2, the a^n , v^n , and u^n , are the nodal accelerations, velocities, and displacements, respectively, at time step n . M refers to the nodal mass matrix whereas P^n and F^n refer to the body forces and the stress divergence. The donor cell algorithm, a first order upwind scheme, was used to perform the advection step. For each time step, the temporal integrations were performed explicitly using a second order accurate central differencing scheme.

For the purposes of the present work, the description of the multi-phase mixture of detonation products, soil, and air was handled in a relatively simple manner that is often used for ALE computations. Each element within the ALE computational domain could be populated with more than one material. For each time step, the strain rates for all materials within an element were set to the value of the average strain rate for the element. Subsequently, the stress state of each element was determined by summing the products of the volume fraction and stresses of each constituent of the element. Beyond this, no assumptions were made regarding the coupling of the soil and gaseous components of the mixture. Benson (2010) has reported that this method, is simple, robust, and conserves energy exactly.

The interface between the rigid target and the fluids was treated as having infinite slip. At the outer surfaces of the computational domain the default zero force boundary condition was used. For this boundary condition, outflow is not prevented and inflow to cells is constrained to be composed of the same material that is present in the cells. It should be noted, though, that the ALE computational domain was sufficiently large and that the pressures at the internal boundary of the domain were of sufficient positive magnitude that it was unlikely that prescription of this particular boundary condition, for this set of computations, had much of an effect on the results.

Table 4.1: Explosive model parameters (adapted from Dobratz (1981) as reported in Cooper (1997)).

Parameter	Value
Initial density (kg/m ³)	1,480
Detonation velocity (m/s)	7,000
Chapman-Jouget pressure (Pa)	1.95 X 10 ¹⁰
Jones Wilkins Lee (JWL) parameter A (Pa)	3.490 X 10 ¹¹
JWL parameter B (Pa)	4.524 X 10 ⁹
JWL parameter C (Pa)	5.204 X 10 ⁸
JWL parameter R ₁ (dimensionless)	4.1
JWL parameter R ₂ (dimensionless)	1.2
JWL parameter ω (dimensionless)	0.30

4.3.2 Constitutive models

The 6061 aluminum alloy that comprised the targets was modeled as a rigid solid. The behavior of the reaction products from the detonation of Detasheet C, the high explosive used for this work, was defined in terms of initial density, Chapman-Jouget pressure, detonation velocity, and a Jones Wilkins Lee (JWL) equation of state for description of the adiabat. The form of the JWL equation of state that was used for this work was

$$p = A \left(1 - \frac{\omega}{R_1 V} \right) e^{-R_1 V} + B \left(1 - \frac{\omega}{R_2 V} \right) e^{-R_2 V} + \frac{\omega E'}{V} \quad (4.5)$$

V in this equation is defined as the ratio of the volume of the detonation reaction products to the initial volume of the explosive. E' is the energy per unit volume. p is pressure. A , B , ω , R_1 , and R_2 are constants. The values of the JWL parameters used in these models were adapted from Dobratz (1981) as reported in Cooper (1997) and are shown in Table 4.1. The JWL coefficient C was modified slightly to ensure that the equation of state more closely reflected the known amount of available specific chemical potential energy of the Detasheet C explosive. The air was modeled as having Newtonian viscosity and an ideal gas equation of state; air properties are shown in Table 4.2.

For computations involving pure water, without any soil, as the material surrounding

Table 4.2: Fluid model parameters (Mie-Gruneisen parameters are from Steinberg (1987)).

Parameter	Water	Air
Initial density at 20 °C (kg/m ³)	998.2	1.204
Tensile cutoff (Pa)	-0.01	-1.0
Dynamic viscosity at 20 °C (N s/m ²)	1.002 X 10 ⁻³	1.82 X 10 ⁻⁵
Equation of state type	Mie-Gruneisen	Ideal gas
Specific heat ratio	–	1.4
Gruneisen Γ_0	0.50	–
Mie-Gruneisen EOS C (m/s)	1,480	–
Mie-Gruneisen EOS S ₁	2.56	–
Mie-Gruneisen EOS S ₂	-1.986	–
Mie-Gruneisen EOS S ₃	0.2268	–
Mie-Gruneisen EOS a	2.67	–

the explosive, the water was treated as being a simple Newtonian fluid. Its properties are also shown in Table 4.2. The approach to the water equation of state was based on what was reported and used by Steinberg for modeling spherical explosions in water (Steinberg, 1987). The Mie-Gruneisen equation of state was used to model the compressive behavior of the water. This equation can be written as

$$p = \frac{\rho_0 C^2 (V_0/V) \left[1 + \left(1 - \frac{\Gamma_0}{2} \right) (V_0/V) - \frac{a}{2} (V_0/V)^2 \right]}{\left\{ 1 - (S_1 - 1) (V_0/V) - S_2 \frac{(V_0/V)^2}{(V_0/V)+1} - S_3 \frac{(V_0/V)^3}{[(V_0/V)+1]^2} \right\}} \quad (4.6)$$

where p is the pressure, Γ_0 is the Gruneisen constant, a is the linear correction to the Gruneisen constant. C , S_1 , S_2 , and S_3 define the intercept and the slope of the experimentally determined shock velocity - particle velocity curve for a given material. Here, V/V_0 is the ratio of the volume V of the water while it is in any particular state relative to a reference volume V_0 . The values of the various coefficients used for the equation of state are shown in Table 4.2. The hydrostatic behavior calculated using this equation of state and assumed for the water is shown in Figure 4.3.

The amount of momentum transferred from a system comprised of shallow buried explosive in soil to an external target is dependent on the characteristics of the high explosive

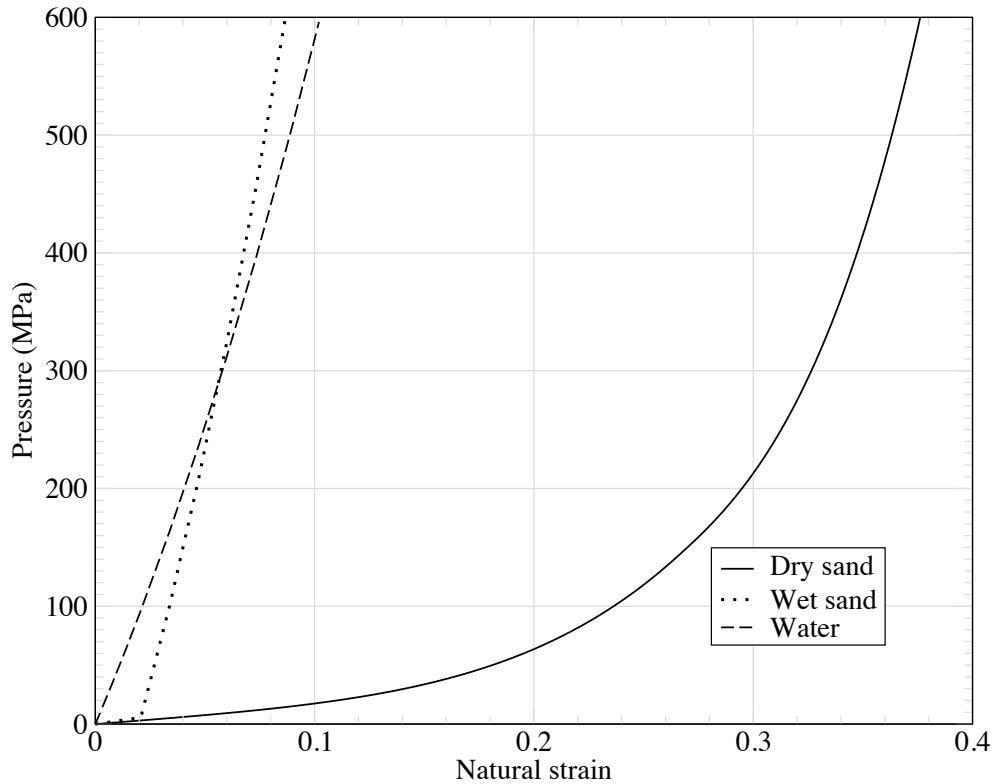


Figure 4.3: Compressive behavior of dry sand, wet sand, and water.

but is also very much a function of the properties of the soil. The definition of the properties of wet and dry sand as applied in this work was based on soil constitutive properties generated for the work that was done to develop hybrid elastic-plastic soil models used for the prediction of ground shock (Zimmerman et al., 1992; Akers et al., 1995). The volumetric and yield relations used to predict the sand behavior were developed based on a combination of quasi-static test results and effective stress theory (Zimmerman et al., 1993).

The particle size distributions for the poorly graded sand used in the blast experiments and for the poorly graded sands that were mechanically tested to determine the continuum properties used to define the constitutive models used in the computations are compared in Figure 4.4. Although the sands used in the computations were a little bit more coarse than that used for the blast experiments, the three sands are considered to be very similar

(Ehrgott et al., 2011a; Windham, 2013; Ehrgott, 2013).

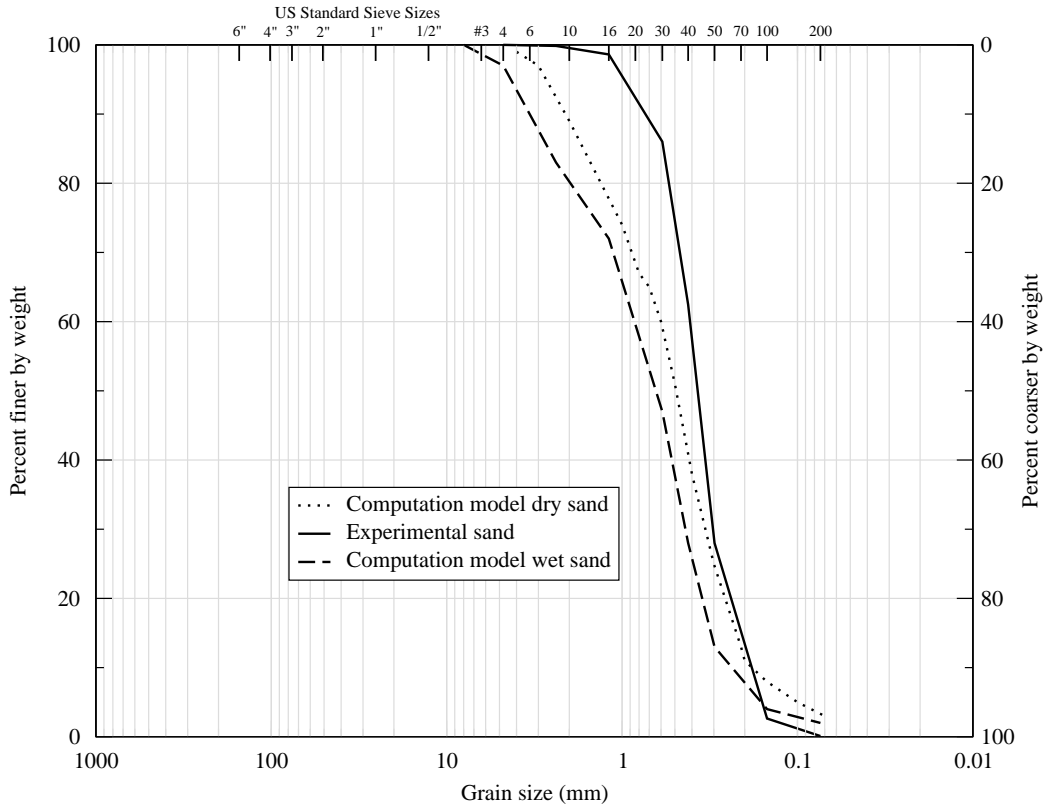


Figure 4.4: Particle size distributions for sand used in blast experiments and for sands that were tested to define the constitutive models used in the computations. Although the computational sands were a little bit coarser, the sands were very similar (Ehrgott, 2011b; Windham, 2013; Ehrgott, 2013).

The physical properties used to model the dry sand were based directly on the hybrid elastic-plastic models used in SABER (Akers et al., 1995). Constitutive properties were available in SABER for partially saturated sand with air filled void contents of 1% and of 5% but were not available for sand with an air filled void content at an intermediate level characteristic of the sand used in the small scale blast experiments. As a result, the pressure-volume relation, yield surface, and other physical soil parameters used for this sand were estimated using the method of bisection (Gear, 1978) and were subsequently validated successfully against various small-scale blast experiments.

The application of the method of bisection was straightforward. First, there was use of

the available 1% and 5% air filled void properties as well as properties that were estimated, as explained below, for a value of air filled voids at the midpoint between the two available levels, viz., at the level of 3% air filled voids content, to perform a computation to predict the maximum impulsive loading on a flat target.

These results were compared with experiment and it was observed that the peak experimental value of target momentum was somewhere between the levels that were computed for sand with 1% and 3% air filled void content. Next the properties of a soil with air filled voids content midway between 1% and 3% were estimated and subsequently this bisection process was performed repeatedly until the computed value for target momentum converged to the experimental value.

At this point, the constitutive properties determined for the converged level of air filled void content were used to perform computations that gave reasonable agreement with experiments involving various alternate target geometries and loading conditions. The experiments used previously for evaluation of the wet sand material model were, in some respects, similar to the current experiments but the scale and target geometry for those experiments was, in some cases, different from those employed in the current work.

Figure 4.5 shows the pressure-volumetric strain relations for the 1% and the 5% air filled void content sands as well as the relation for the converged value (2.09% air filled voids) found via the bisection method. A careful examination of the hydrostats for the 1% and 5% air filled void content sands revealed several things.

Each of the two soils exhibited two regimes of compressibility. The first regime existed at lower levels of strain and was found to give an excellent fit, for both soils, to a linear relation between pressure and volumetric strain and to exhibit a significantly lower stiffness than the regime which existed at higher levels of strain. The second regime existed at levels of strain that exceeded the strain at which the air filled void content would be expected to become vanishingly small, exhibited a significantly higher stiffness than the first regime, and was found to fit a quadratic relation between strain and pressure.

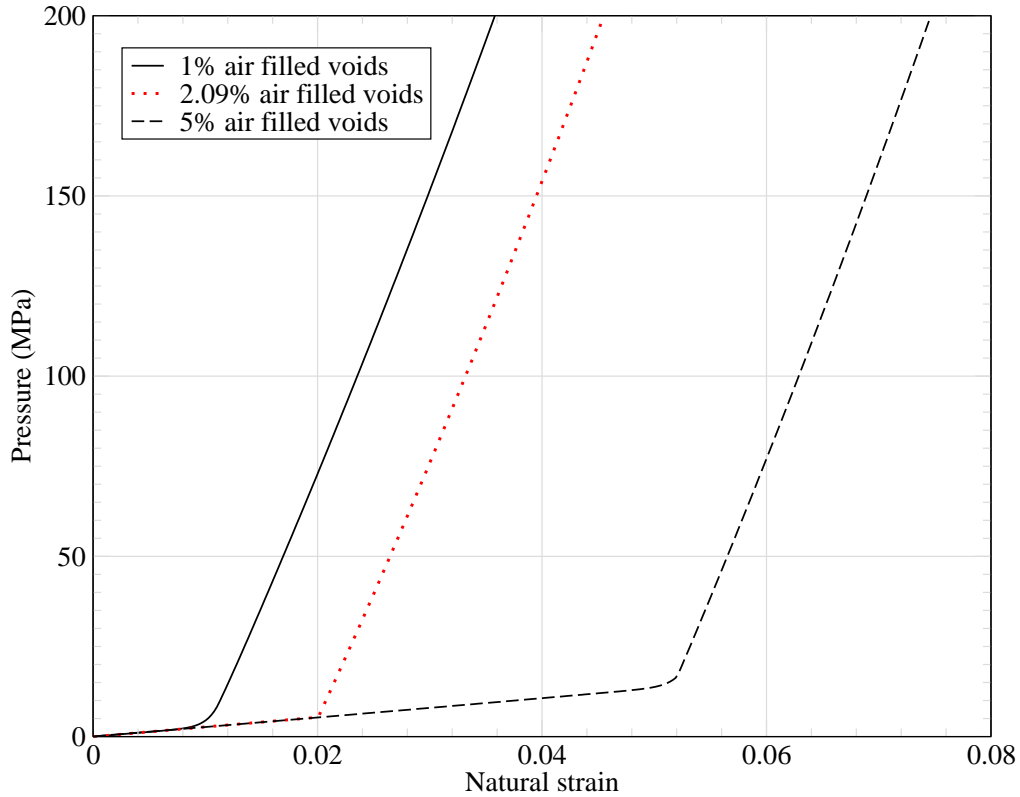


Figure 4.5: Pressure - volumetric strain relations for the 1% and 5% air filled void content sands as well as for the converged value (2.09% air filled voids) found via the bisection method.

In addition, it was noticed that the low pressure relations for the two soils were co-linear and that the relations for the high pressure regimes, if translated along the line that defined the low pressure regime, were found to overlay one another. These results were used to estimate the pressure-volumetric strain behavior of the soil, at various levels of air filled void content, in the application of the bisection method to the identification of constitutive properties of the wet sand used in the blast experiments.

The yield surfaces for the 1% and 5% air filled void content sand as well as the surface for the converged air filled void content are shown in Figure 4.6. The hydrostats (pressure-volumetric strain relations) for air filled voids contents between 1% and 5% exhibited a linear relation between pressure and air filled void content. The asymptotic yield behavior exhibited at higher pressures by the 1% and 5% air filled voids content sands begins when

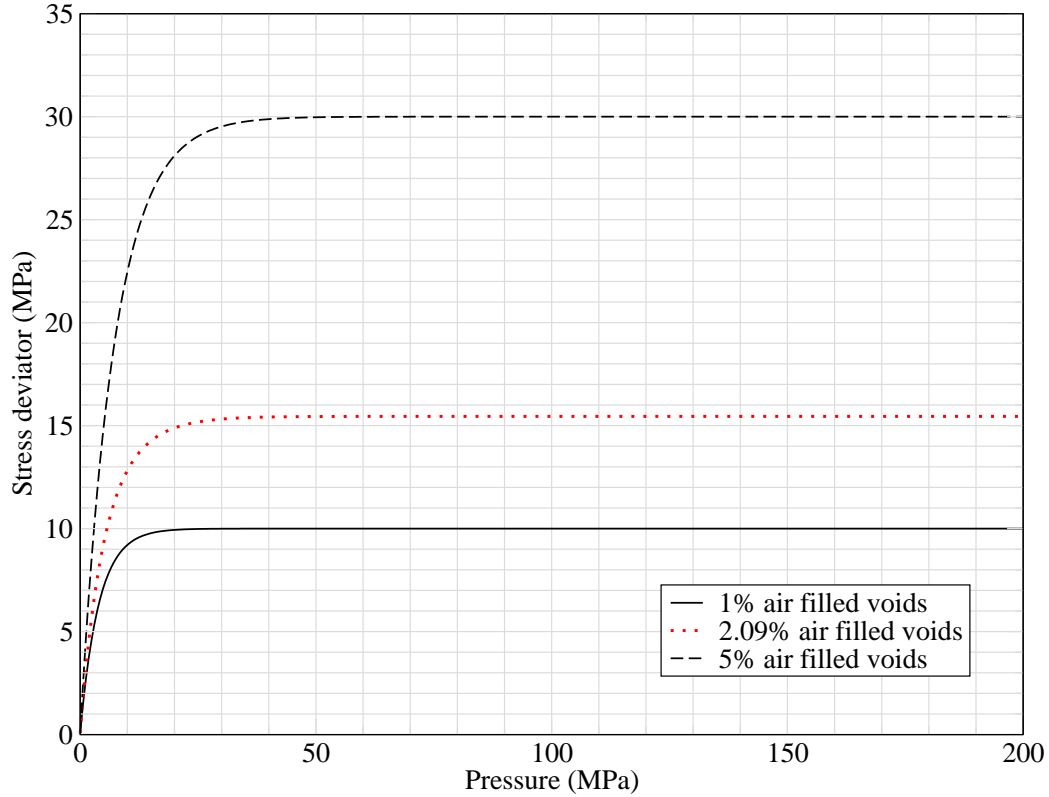


Figure 4.6: Yield relations for the 1%, 5% sands and for the converged value (2.09% air filled voids) sand estimated by means of the bisection method.

the pressure forces the air filled void content to become vanishingly small.

Beyond this level of pressure, the water carries the additional hydrostatic stress which essentially limits the friction - and the yield - to a constant level, for undrained conditions, as pressure continues to increase (cf. Lambe and Whitman (1968)). Furthermore, the testing that resulted in the yield surfaces for the 1% and 5% air filled voids sand was, by design, more accurate at higher pressures than at lower pressures. As a result, the yield surface was estimated for sands with various air filled void contents using linear interpolation.

Since the sand used in the blast experiments was poorly graded, granular in nature, and had a particle distribution that was similar to that used to prepare the 1% and 5% air filled voids constitutive models, a relatively constant dry density was assumed between the soils and the resulting relationship between bulk or wet density ρ_{bulk} and air filled voids

volume fraction α_{air} (Lambe and Whitman, 1968):

$$\rho_{bulk} = \rho_{dry} + \rho_{water} (1 - \rho_{dry}/G_s - \alpha_{air}) \quad (4.7)$$

where ρ_{dry} was the dry density of the soil, ρ_{water} was the density of water in the soil, and G_s was the specific gravity of the soil particles. The bulk density varied linearly with the air filled void content and was calculated directly for a given volume fraction of air voids. Finally, the values used to estimate tensile cutoff and Poisson ratio for levels of air filled content intermediate between 1% and 5% were calculated by means of linear interpolation. The values of Initial wet density, Poisson ratio, and tensile cutoff for 1%, 5% and converged (2.09%) air filled void volume fraction are summarized in Table 4.3.

Table 4.3: Converged wet sand properties. Properties for 1% and 5% air filled voids sands were interpolated to their converged values for 2.09 air filled voids.

Parameter	1% air filled voids sand	2.09% air filled voids sand	5% air filled voids sand
Initial wet density (kg/m ³)	2,117	2,106	2,077
Poisson ratio	0.48	0.47728	0.47
Tensile cutoff (Pa)	-27,784	-24,820	-16,937

Some of the general properties of the soil models are given in Table 4.4. The tensile failure of the soils, which generally occurs at very low levels of stress, was prescribed to occur as a function of the times during which the maximum principal stress in an element was in tension and exceeded the value of tensile cutoff given in Table 4.3.

Table 4.4: Miscellaneous soil model parameters.

Parameter	Dry sand	Wet sand
Initial wet density (kg/m ³)	1,750	2,106
Poisson ratio	0.34	0.47728
Tensile cutoff (Pa)	-24,500	-24,820

The behavior of the soil was described using a hypoelastic, variable modulus treatment (Nelson and Baron, 1971; Rohani, 1977). The relationship between the stress increments $d\sigma_{ij}$ and the strain increments $d\epsilon_{ij}$ was defined as

$$d\sigma_{ij} = K d\epsilon_{kk}\delta_{ij} + 2 G \left(d\epsilon_{ij} - \frac{1}{3}d\epsilon_{kk}\delta_{ij} \right) \quad (4.8)$$

where K was the variable bulk modulus, and a constant Poisson ratio ν was used so that the variable shear modulus $G(K, \nu)$ was calculated as

$$G(K, \nu) = \frac{3K(1 - 2\nu)}{2(1 + \nu)}. \quad (4.9)$$

The volumetric constitutive properties of the soils were input to the solver in tabular form. The data pairs input to the table consisted of soil pressure levels that corresponded to various states of natural volumetric strain. These data for the wet and dry sand, which are shown graphically in Figure 4.3 and compared with the pressure volume behavior of the water, were differentiated numerically by the solver to yield the bulk and shear moduli that were used for the finite element calculations.

The yield behavior of the soil was defined by a two invariant exponential yield surface defined by the pressure and the stress deviator (DiMaggio and Sandler, 1971) such that the yield function f was given by

$$f(J_1, J_2') = \sqrt{3J_2'} - [A - C \exp(B J_1/3)] = 0 \quad (4.10)$$

with J_1 and J_2' referring to the first stress invariant and the second deviatoric stress invariant, respectively, and where A, B, and C were experimentally fitted constants. At lower levels of pressure the yield surface approximated a Drucker-Prager cone but at higher pressures asymptotically approached a Mises cylinder. The deviatoric yield behavior of the wet and dry sand are shown in Figure 4.7.

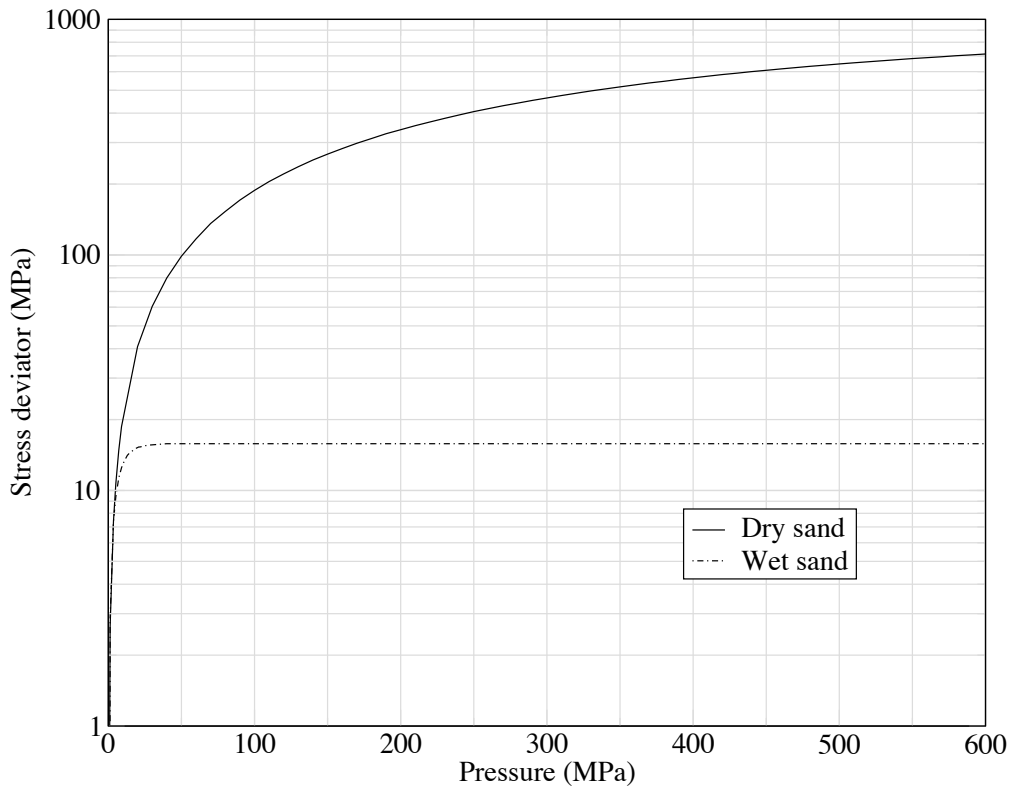


Figure 4.7: Yield surfaces for wet and dry sand.

4.4 Results and analysis

Figure 4.8 shows a comparison of computational and experimental results for momentum imparted to rigid targets of various diameters. The experimental work was performed by Fournay et al. (2010). The computations and best fit curves were performed as a part of the present work. Best fit curves were determined using least squares fits to quadratic polynomials for the water and the wet sand and cubic splines for the dry sand. For all three substrates - dry sand, wet sand, and water - target momentum increased with target disk diameter. The experimental results were reported to have been accurate to within +/- 10% of their true values (Fournay, 2013a). It can be observed that the values of calculated momentum, for any particular combination of disk size and substrate, were very close to the experimentally determined values.

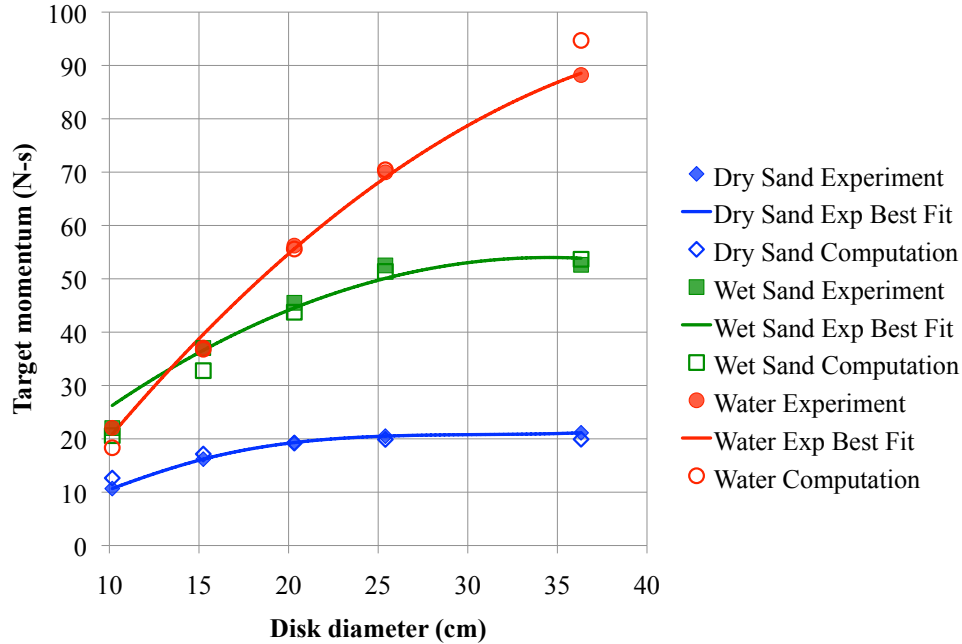


Figure 4.8: Comparison of experiment and computation for various target sizes. Best fit curves were determined using least squares fits to quadratic polynomials for the water and wet sand and using cubic splines for the dry sand.

Figure 4.9 shows, based on the computations, for the progression of 25.4 cm target loading as a function of time for the case of explosive buried in wet sand. In Figure 4.9a-d, the gold body represents the rigid target, the brown region comprises the sand, the green region contains the expanding gaseous detonation products, and the light blue region is the air. Figure 4.9e shows the computational vertical acceleration-time history for the target.

Figure 4.9a is taken 40 μs after detonation and shows the initial contact between the sand and the target with the resulting initial rise in target acceleration. Figure 4.9b shows the conformation of the system at 68 μs , the time at which peak acceleration occurs. It should be noted here that the development, after the initial contact at 40 μs , of an annular region of soil which expands radially and continues to transfer momentum to the target at 1 ms (Figure 4.9c) and which at 2 ms, the time at which the target acceleration has essentially ended, has expanded beyond the circumference of the target and, as a result, has ceased to supply momentum to the target (cf. Figure 4.9d and Figure 4.9e).

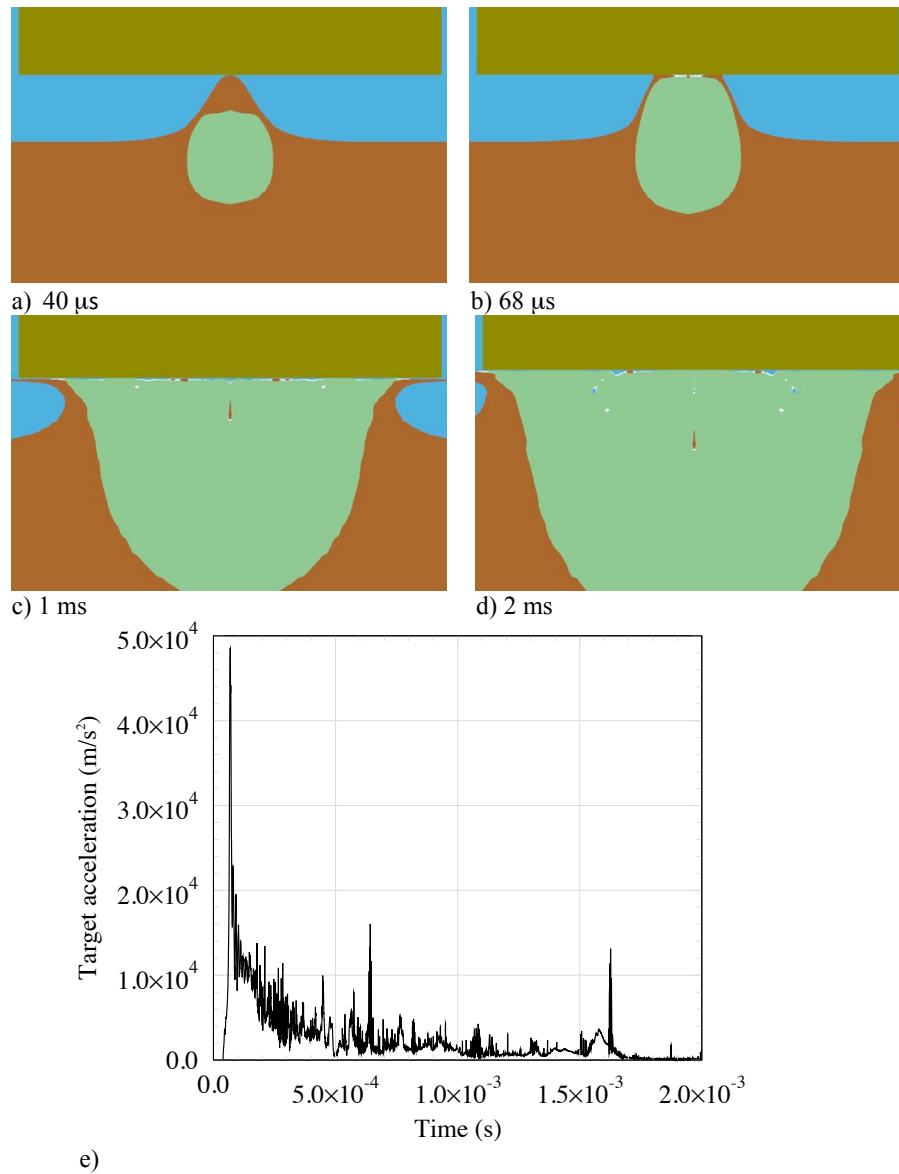


Figure 4.9: Computations for 25.4 cm target loading with wet sand. (a) 40 μs - initial contact of sand with target. (b) 68 μs - peak target acceleration. (c) 1 ms - target acceleration continues. (d) 2 ms - target acceleration has ended. (e) Acceleration - time history. The target is yellow, the sand is brown, the detonation products are green, and the air is blue.

As a result of the close agreement between the computational models and experiment, it was considered that it might be possible to deduce something about the target loading mechanisms by the application of appropriately designed computational factorial comparisons whereby various components of the material models for the test bed substrates are combined in various ways in order to determine which of the material properties might have the greatest effect on the amount of momentum transferred to a target (Montgomery, 1991). Two such groups of computations were performed. First the behavior of water and wet sand were compared by performing a 2^3 full factorial design for which the effects of initial wet density, the volumetric relation, and the yield surface were compared. There was also a comparison of the behavior of dry sand and wet sand by means of a 2^4 full factorial design for which the effects of wet density, pressure-volume behavior, yield surface and Poisson ratio were measured and compared. For both sets of investigation, results were examined for a fixed target diameter of 25.4 cm.

Table 4.5: Computational results for the water-wet sand comparison.

Run	Density Relation	Pressure volume relation	Yield surface	Peak target momentum (N s)
1	wet sand	wet sand	wet sand	51.38
2	wet sand	wet sand	water	86.14
3	wet sand	water	wet sand	57.15
4	wet sand	water	water	88.66
5	water	wet sand	wet sand	41.92
6	water	wet sand	water	69.45
7	water	water	wet sand	47.20
8	water	water	water	70.44

The effect of a particular factor - for example, density - in the comparison between wet sand and water, was measured by taking the difference between the mean target momentum with water density and the mean target momentum with wet sand density

$$c_p = \bar{y}_{wet\ sand} - \bar{y}_{water} \quad (4.11)$$

where c_ρ denotes the momentum effect due to density ρ , $\bar{y}_{wet\ sand}$ is the mean momentum calculated using wet sand density, and \bar{y}_{water} is the mean momentum calculated using water density.

The normalized effects were calculated by dividing each of the effects by the effect possessing the greatest magnitude. For both comparisons, viz., that between wet sand and water as well as that between wet sand and dry sand, the factor that had the greatest effect on target momentum was yield surface type. Therefore, the normalized effects were calculated by dividing each effect in each of the two comparisons by the effect calculated for yield surface. The raw results from these computations are shown in Table 4.5.

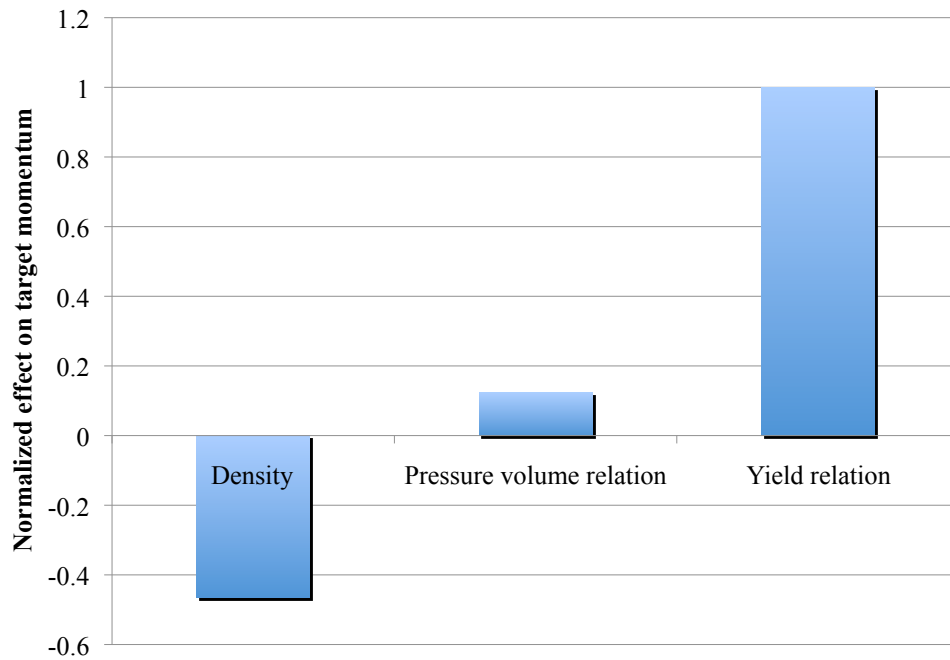


Figure 4.10: Normalized response from the water - wet sand comparison.

When the behavior of the water and wet sand was compared (Figure 4.10), it was observed that, in the mean, the factor that had the greatest effect on the amount of momentum imparted to the target was the yield relation. For this factor, as well as for the other two factors, a positive effect was one that was a result of the water behavior being, in the mean, larger than the effect associated with the unsaturated sand. Thus when the

effect of yield strength on target momentum was examined, the effect of the yield strength of water was greater than the effect of the yield strength of wet sand. The yield surface for the wet sand is shown in Figure 4.7; the water, of course, has no strength, so it can be inferred that the momentum imparted by the material with no strength - the water - was greater than that imparted by that with the higher strength - the wet, partially saturated sand.

Table 4.6: Computational results for the dry sand-wet sand comparison.

Run	Density Relation	Pressure volume relation	Yield surface	Poisson Ratio	Peak target momentum (N s)
1	dry sand	dry sand	dry sand	dry sand	19.89
2	dry sand	dry sand	wet sand	wet sand	47.19
3	dry sand	wet sand	dry sand	dry sand	22.38
4	dry sand	wet sand	wet sand	wet sand	48.77
5	wet sand	dry sand	dry sand	dry sand	20.42
6	wet sand	dry sand	wet sand	wet sand	49.93
7	wet sand	wet sand	dry sand	dry sand	23.67
8	wet sand	wet sand	wet sand	wet sand	51.38
9	dry sand	dry sand	dry sand	wet sand	39.42
10	dry sand	dry sand	wet sand	dry sand	41.43
11	dry sand	wet sand	dry sand	wet sand	42.34
12	dry sand	wet sand	wet sand	dry sand	43.87
13	wet sand	dry sand	dry sand	wet sand	41.59
14	wet sand	dry sand	wet sand	dry sand	43.58
15	wet sand	wet sand	dry sand	wet sand	45.33
16	wet sand	wet sand	wet sand	dry sand	46.65

The difference in the inertial effect of the substrate material resulting from the difference in initial density - 998 kg/m^3 for water versus $2,106 \text{ kg/m}^3$ for the unsaturated sand - also showed a fairly significant effect. For this case the material with the higher density - the sand - imparted more momentum than did the material with the lower density. The effect based on the difference in stiffness (cf. Figure 4.3) seemed to produce an effect with more momentum imparted by the stiffness associated with water - although this was the smallest

effect of the three.

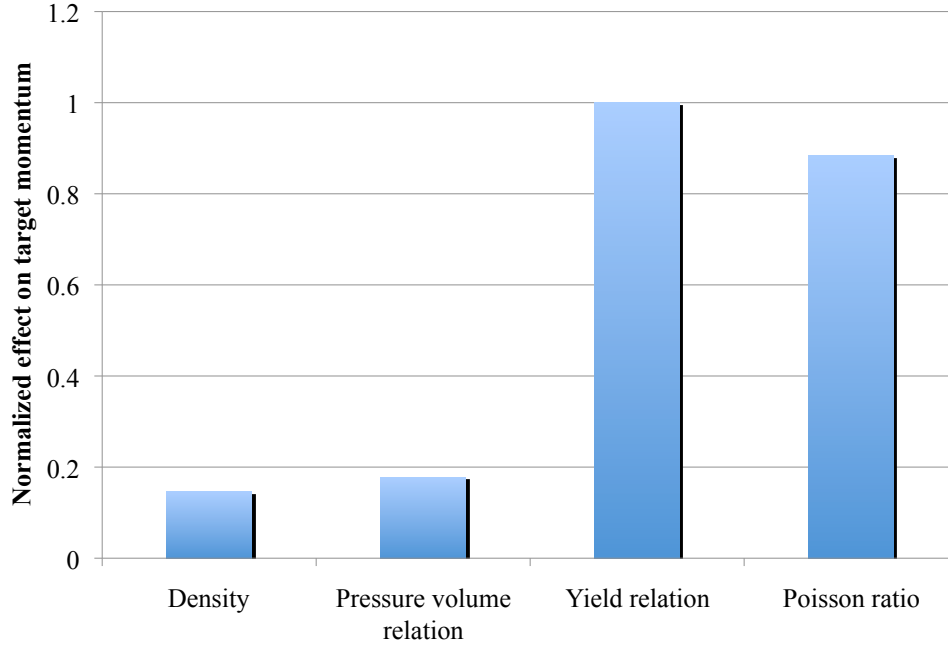


Figure 4.11: Normalized response from the wet sand - dry sand comparison.

A similar approach was used to compare the magnitudes of the mean effects of the properties of wet saturated and dry sand on the amount of peak momentum transferred to a 25.4 cm target. For this case, a 2^4 full factorial design was used to look at the effects of initial density, yield surface, volumetric behavior, and Poisson ratio. The raw results are shown in Table 4.6; a comparison of the normalized effects is shown in Figure 4.11. For this case, the greatest effect was also that due to yield. In Figure 4.11, normalized effects greater than zero - in this case, all of the effects - are those due to the effect of the property associated with wet sand being greater in absolute value than the effect resulting from same property for the dry sand:

$$c_{[\cdot]} = \bar{y}_{wet\ sand} - \bar{y}_{dry\ sand} \quad (4.12)$$

where $c_{[\cdot]}$ denotes the effect on momentum transfer due to property $[\cdot]$, $\bar{y}_{wet\ sand}$ is the mean momentum calculated using the property associated with partially saturated sand, and

$\bar{y}_{dry\ sand}$ is the mean momentum calculated using the property associated with dry sand.

therefore it can be seen that the lower strength of the unsaturated sand resulted in greater target momentum than did the higher strength of the dry sand (see Figure 4.7). It was noticed that the effect of Poisson ratio was also very significant with the higher Poisson ratio of the wet sand 0.48 producing greater target momentum than that of the dry sand 0.34. The effects due to the pressure-volume behavior and the initial bulk density were less pronounced than those from the strength and Poisson ratio. The volumetric behavior for the two initial states of the sand is shown in Figure 4.3; the initial densities of the unsaturated and the dry sand were 1,750 and 2,150 kg/m³, respectively.

Figure 4.12 compares fringes of the rate of shear strain and flow pathlines for (b) dry sand, (c) wet sand, and (d) water. Figure 4.12(a) shows the initial state of all three systems. Figure 4.12 illustrates several things; four of them are germane to the present discussion. First of all, the crater size 150 μ s subsequent to detonation increases as substrate material changes from dry sand to wet sand and, then, to water. Secondly, it can be seen that, based on the pathlines, the overall amount of flow seems to vary with substrate type in the same way as the crater size.

Thirdly, the volume of material involved in substrate flow, as evidenced by the shear strain rate contours, seems to increase with decreasing strength and increasing target momentum as substrate type changes from dry sand to wet sand and then to water. Finally, it appears that the seal created by annular walls of substrate seems to open earlier for dry sand than for wet sand and water perhaps thereby allowing earlier release and expansion of the high pressure detonation product gases that drive the movement of substrate which, ultimately, results in a lower momentum increase of the rigid target.

When the first order interactions between the factors were examined, it was noticed that the only really significant interaction was that between the strength and the Poisson ratio. This interaction was such that the effect of Poisson ratio was fairly minimal when the wet sand yield surface was used but became significant when the strength model was that

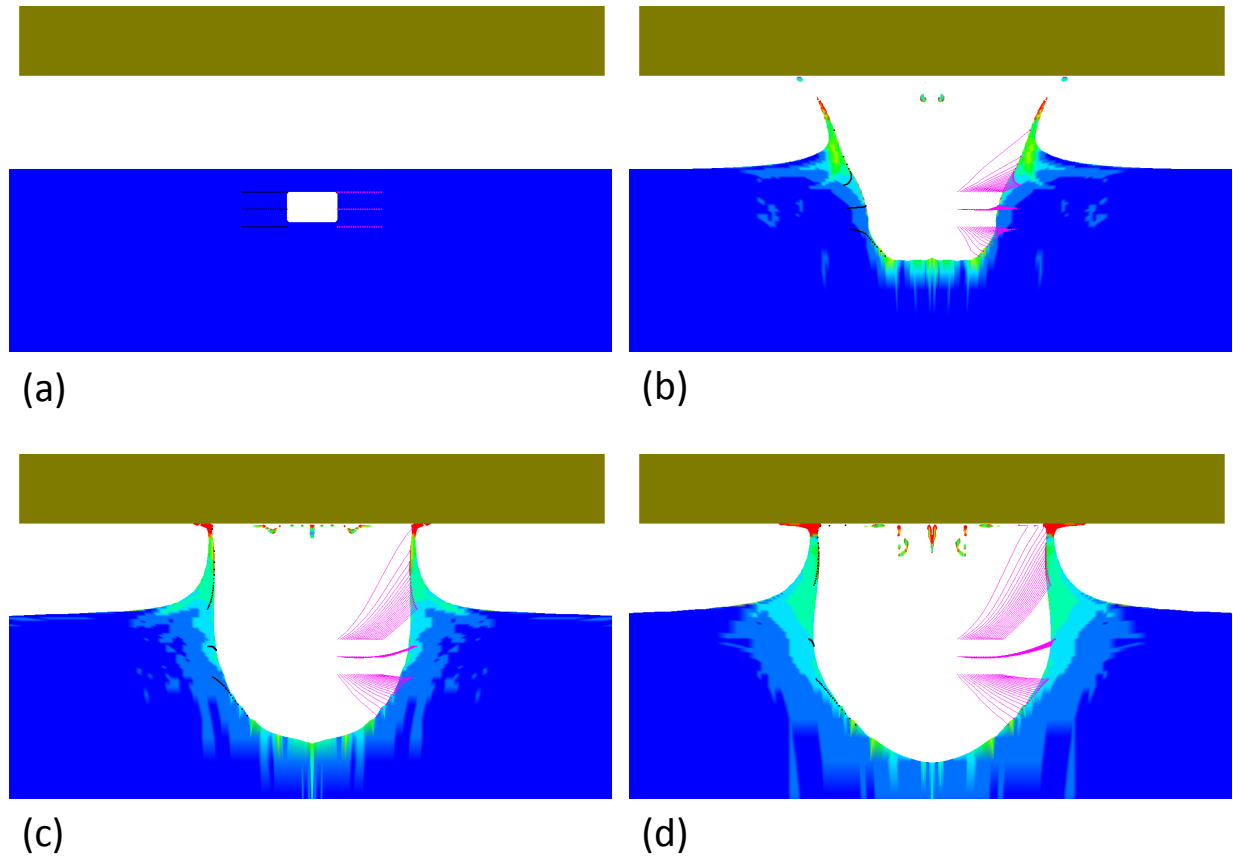


Figure 4.12: Comparison of computational deviatoric strain rate and substrate flow $150 \mu\text{s}$ after detonation for dry sand, wet sand, and water. (a) Initial state for all three substrates. (b) Dry sand. (c) Wet sand. (d) Water. The gold body is the rigid target; the fringed body is the deforming substrate. Magenta traces are pathlines of tracers initially embedded in substrate. Flow and deviatoric strain rate increased while strength decreased in the order dry sand- wet sand - water. Strain rate increases as fringe changes from blue to red.

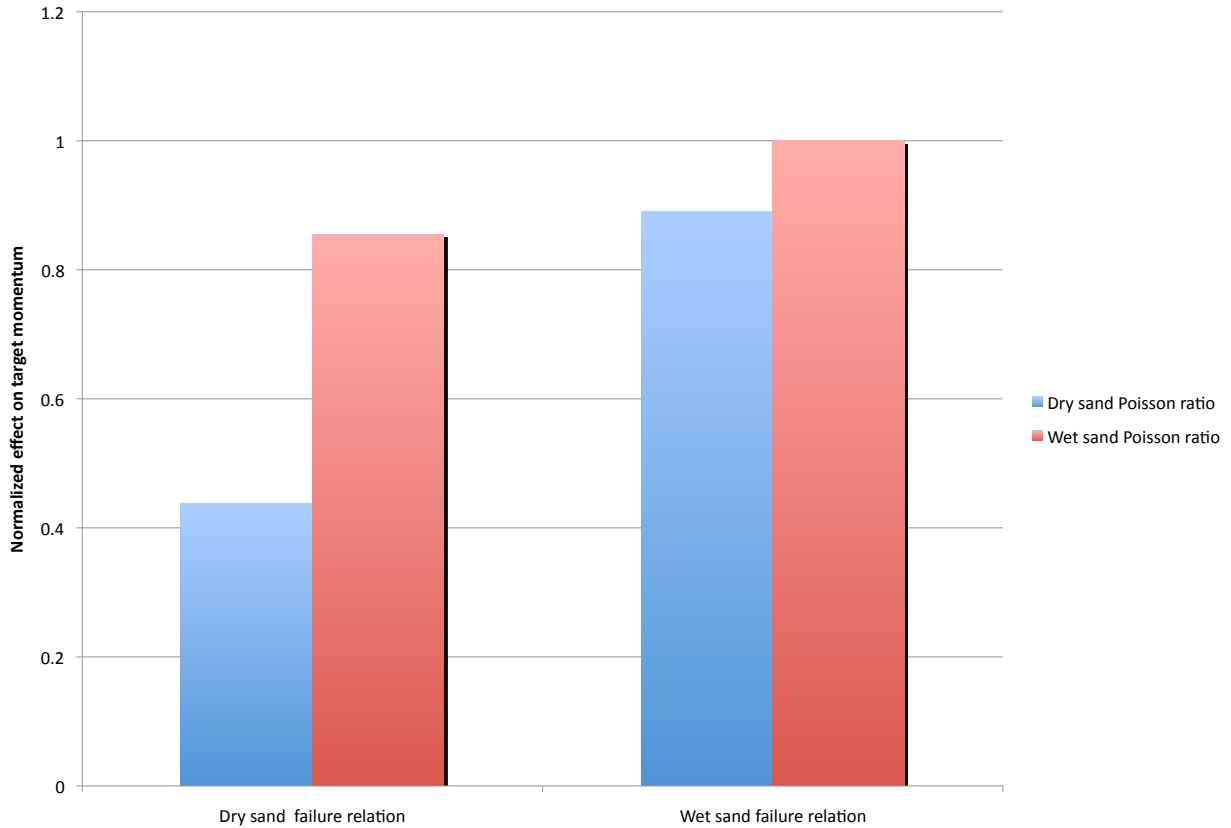


Figure 4.13: First order interaction between yield surface type and Poisson ratio.

for the dry sand (Figure 4.13). The interaction between Poisson ratio and yield relation for sand was analyzed by first calculating and comparing the effect of the two types of Poisson ratio for the cases involving the dry sand yield relation and then repeating this process for the cases involving the wet sand yield surface. The other, relatively insignificant, first order interactions were estimated in a similar fashion.

A comparison of the yield surfaces and the behavior of the various combinations of Poisson ratio and strength model for a simulated uniaxial strain test (Figure 4.14) give some insight into the reasons for the first order interaction. First of all, the larger Poisson ratio prescribed for the behavior of the wet sand results in higher lateral stresses in reaction to an increased axial stress for an applied uniaxial strain test. The pressure in Figure 4.14 is given by $p = (\sigma_a + 2\sigma_l) / 3$ while the Mises or effective stress, σ_{eff} is defined to be equal

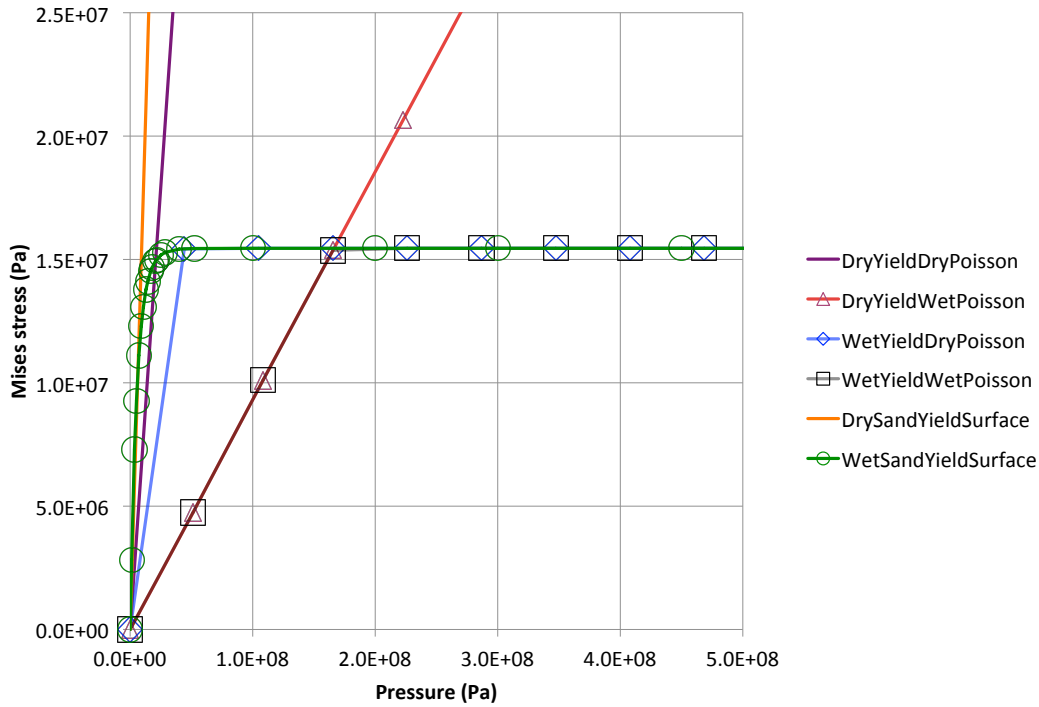


Figure 4.14: Uniaxial strain stress path response for various combinations of Poisson ratio and yield surface.

to the difference $\sigma_a - \sigma_l$ where σ_a is the axial, applied stress and σ_l is the lateral stress. Therefore a higher effective stress implies, at any given pressure and for a uniaxial strain path with applied axial compression, a lower lateral stress since for this strain path the magnitude of the axial stress will always be greater than or equal than that of the axial stress.

The wet sand yield surface, at all pressures, causes yielding at a significantly lower level of effective stress than does the dry sand yield surface. It can be seen, from Figure 4.14, that the lower yield stress of the wet sand yield surface limits the large differences in lateral stress, particularly at higher levels of pressure, that might be caused by a difference in Poisson ratio. On the other hand, for the case of the dry sand yield surface the difference in Poisson ratio can cause, particularly at higher pressures, significantly higher lateral stresses which, for a substrate in an unconfined state such as the sand on the sides of and on top of the cavity filled with the expanding explosive detonation products, will cause greater lateral

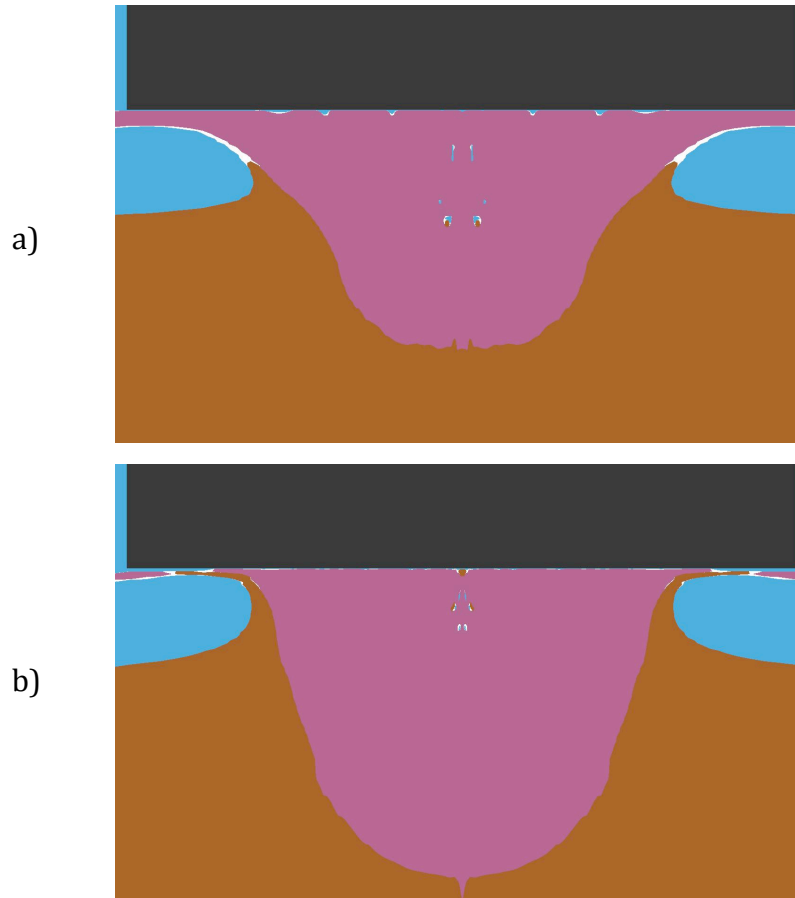


Figure 4.15: Effect of Poisson ratio for dry sand $750 \mu\text{s}$ after detonation. a) Dry sand. b) Dry sand pseudo-material with wet sand Poisson ratio. The pseudo-material, due to its higher Poisson ratio and resultant higher induced lateral stresses supplied more momentum to the target. The rigid target is dark grey. The air is blue, the detonation products are violet, and the sand is brown.

expansion of the sand surrounding the explosive bubble thereby creating larger tractions at the interface with the target and thus, in the end, imparting more momentum to the target.

Figure 4.15 compares the behavior of the system with dry sand with that of the system with the dry sand pseudo-material with wet sand Poisson ratio $750 \mu s$ after detonation. It can be seen that the higher Poisson ratio resulted in, due to the higher level of induced transverse stress in the substrate, more containment of the detonation product gases. The higher level of containment caused less of the mechanical energy available in the compressed detonation product to vent to the atmosphere, more of it to be available to increase the momentum supplied to the target, and more of the momentum of the moving sand to be imparted to the target.

Chapter 5

Momentum transfer involving sand and soils containing fines

5.1 Overview

It has been observed that factors such as mass density, compressibility, water content, and strength of the medium surrounding the explosive as well as such things as problem geometry affect experimental outcomes. However, there has not been an integrated approach combining constitutive data, experimental blast data, and computational analyses for several soil types at various states that has been extensive enough to expose, to demonstrate, and to explain the fundamental reasons for parametric relations between the momentum transferred to a rigid body and the nature of the medium surrounding a shallow buried explosive.

Small-scale dynamic experiments were performed by the University of Maryland Dynamic Effects Laboratory using explosive charges shallow buried in water or in various soil types at differing initial states (Fourney, 2013b). Using the results from these experiments, it was discovered that the amount of momentum transferred to a rigid target is relatively independent of soil type but that it mostly depends on the initial air-filled void content of the soil and on the effect that water content has on the yield strength of the soil. Data from quasi-static tests of soils at a number of initial states along with known results for the higher pressure behavior of water-quartz mixtures were combined to construct soil models at various initial states for silty sand (SM), clayey sand (SC), and poorly graded sand (SP).

The present chapter focuses primarily on the application of computation and analysis to examine and clarify the mechanisms behind the experimental observations. Computations were performed in order to evaluate the sensitivity of rigid plate loading to various facets of constitutive behavior described in the soil models in order to better understand the causes for the newly revealed parametric relationships. The computations closely matched the experimental results, thereby supporting theories regarding the parametric relations. The

results from the computations offered significant insights into the mechanics behind the parametric relations.

Section 5.2 describes the blast experiment setup, the blast experiment test bed preparation procedures, and the soil characterization methods. Section 5.3 explains the representation of soil and water behavior that was used to examine the blast behavior for various combinations of soil density and water content. Next, Section 5.4 discusses the experimental and computational results and shows, for both, the strong correlation between peak target momentum and the test bed material initial air filled void content. Subsequently, Section 5.5 presents an examination of the sensitivities to soil air filled voids content, water content, and initial density.

5.2 Experimental Setup

5.2.1 Blast test setup

The blast experiments discussed, used for analysis, and used for validation in this work were performed, with some direction by the author - with regard to prescribed soil properties and parameter variation - by colleagues at the University of Maryland Dynamic Effects Laboratory (Fourney, 2013b). The setup for the small scale blast tests performed at the University of Maryland Dynamic Effects Laboratory was similar to that described in section 4.2 except for a few differences. First, only one target geometry was used for the current investigations. The target was a 305 mm diameter, 50.9 mm thick plate constructed of aluminum alloy 6061 with mass 10.05 kg that behaved essentially as a rigid body in its response to the loading from the buried explosive. Also, as will be discussed in more detail, the test bed preparation procedures for the various soil emplacements were different than those used for the work discussed in Chapter 4.

The translation of the target was measured using high-speed video in order to determine the displacement history from which the velocity was determined. The plate momentum was calculated as the product of the vertical translational velocity (over the first 25.4 mm of travel distance) and the plate mass. Figure 5.1 shows photographs of the apparatus that

was used at the University of Maryland for the small scale blast tests.

5.2.2 Test bed preparation

For the case of the water test bed, a 1.8 m by 1.8 m by 0.30 m deep tank was filled with water, the explosive and plate were positioned appropriately (see Figure 4.1), and the explosive was detonated. For the cases involving soil test beds, the soil was first completely dried in an oven at 110 °C. Subsequently the soil was brought to the desired water content by careful hand mixing and gradual addition of water in a 0.076 m³ bucket. Water content w is defined according to the civil engineering convention

$$w = \frac{m_w}{m_s} \times 100 \quad (5.1)$$

where m_w and m_s are the masses of water and of soil solids, respectively, contained in a control volume of the soil.

Once the correct water content was achieved, the soil-water mixture was allowed to equilibrate for 24 hours and then was placed in a thick-walled hollow cylindrical aluminum container with 311 mm inner diameter and 237 mm depth in lifts (layers) that were approximately 25.4 mm in height. All of the layers of the soil in the container were compacted identically and the positions of their top surfaces were carefully measured with a caliper and then scarified before addition of the next layer in order to promote homogeneity of the test bed. Compaction was accomplished by means of a steel rod, 25.4 mm in diameter and 1.5 m long, and a 6.8 kg steel ball with a hole drilled into it which fit over the rod. The ball was dropped from a given height with a given number of impacts until the desired compaction level was achieved.

Air filled voids volume fraction α_a is defined as a proportion of the total volume of the individual constituents in a control volume of the soil:

$$\alpha_{air} = \frac{V_{air}}{V_{total}} \quad (5.2)$$

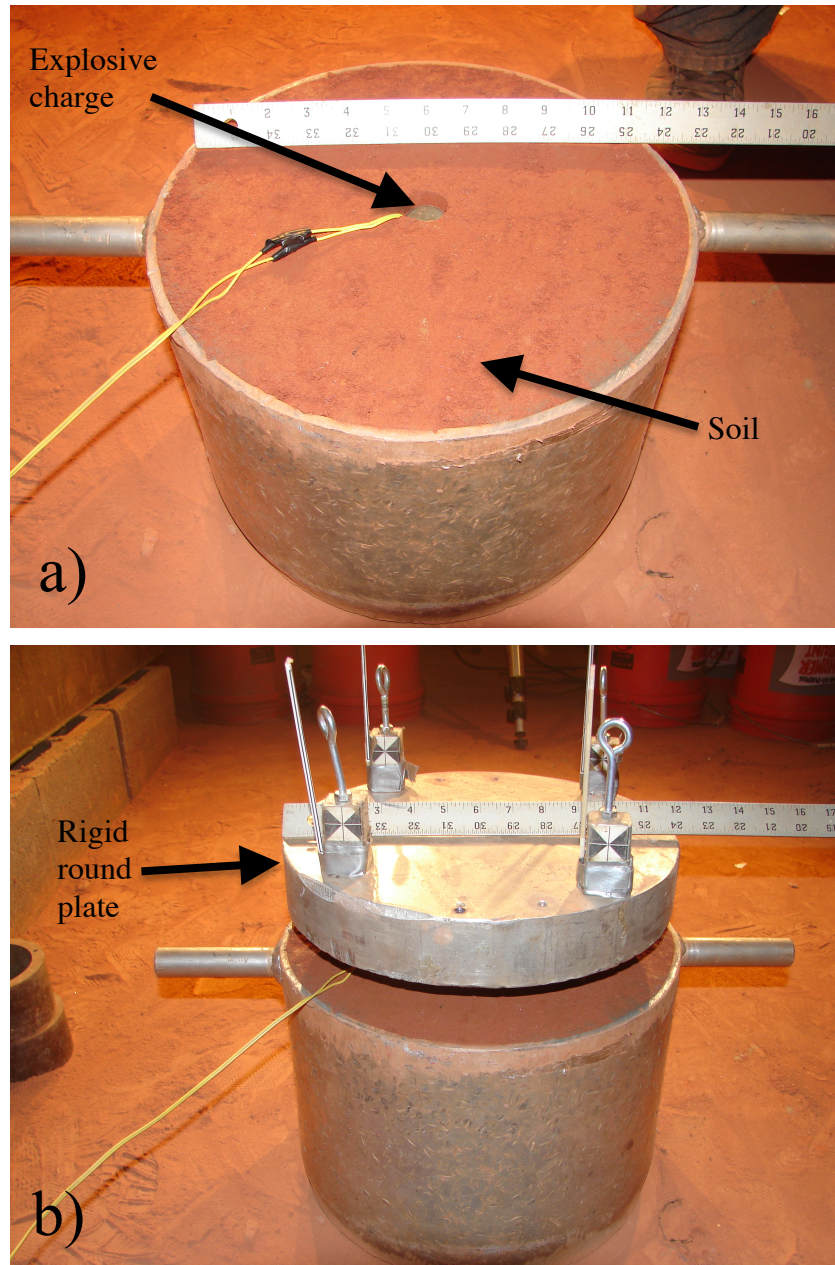


Figure 5.1: Apparatus for small scale blast tests (Fourney, 2013b). The scale of the large ruler is in inches (one inch = 25.4 mm). a. Soil test bed with uncovered explosive charge. b. Apparatus shown with rigid target (round plate) positioned above the soil bed.

Table 5.1: Soil emplacement conditions: poorly graded sand (SP).

Initial volume fraction air	Water content (%)	Initial wet density (kg/m ³)
0.071	19.4	1970
0.104	17.3	1930
0.142	17.3	1850
0.157	17.3	1820
0.167	12.8	1890
0.200	12.8	1810
0.206	17.3	1710
0.230	12.2	1760
0.268	8.8	1740

Table 5.2: Soil emplacement conditions: silty sand (SM).

Initial volume fraction air	Water content (%)	Initial wet density (kg/m ³)
0.059	13.8	2120
0.074	13.8	2080
0.081	11.3	2130
0.134	11.3	2000
0.148	11.3	1970
0.173	11.3	1910
0.209	8.8	1890
0.218	11.9	1800
0.222	8.8	1860
0.263	8.4	1770
0.265	9.7	1730
0.269	9.4	1730
0.273	8.5	1740
0.295	4.2	1790
0.295	4.2	1790
0.299	9.4	1660

or, expressed as a percentage,

$$\text{air filled voids content} = \frac{V_{air}}{V_{total}} \times 100 \quad (5.3)$$

where V_{air} is the volume of air and V_{total} is the total volume of the soil. The soil's total volume is the sum of the volumes of water, solid, and air components of the soil.

It was possible to weigh the entire test bed apparatus by use of a scale. In this way it was determined that it was possible to vary and measure not only the initial water content, but the initial density, which equates to the determination of the air filled voids content of the soil. Once the state of the soil in the test bed was determined, the explosive was placed in its correct position, the small cavity directly above the emplaced explosive was filled with soil and tamped to achieve a similar level of compaction to that of the soil throughout the rest of the bed, the target plate was put in place, and the explosive was detonated. The initial soil conditions for the soils used in the blast experiments are given in Tables 5.1, 5.2, and 5.3.

Table 5.3: Soil emplacement conditions: clayey sand (SC).

Initial volume fraction air	Water content (%)	Initial wet density (kg/m ³)
0.076	14.6	2030
0.092	14.9	1990
0.101	12.4	2020
0.119	10.9	2010
0.136	10.9	1980
0.189	10.9	1850
0.199	10.3	1850
0.206	9.1	1860
0.207	10.9	1810
0.226	10.4	1780
0.240	10.4	1750
0.246	10.9	1730
0.262	10.9	1690
0.292	11.1	1620

5.2.3 Soil Characterization

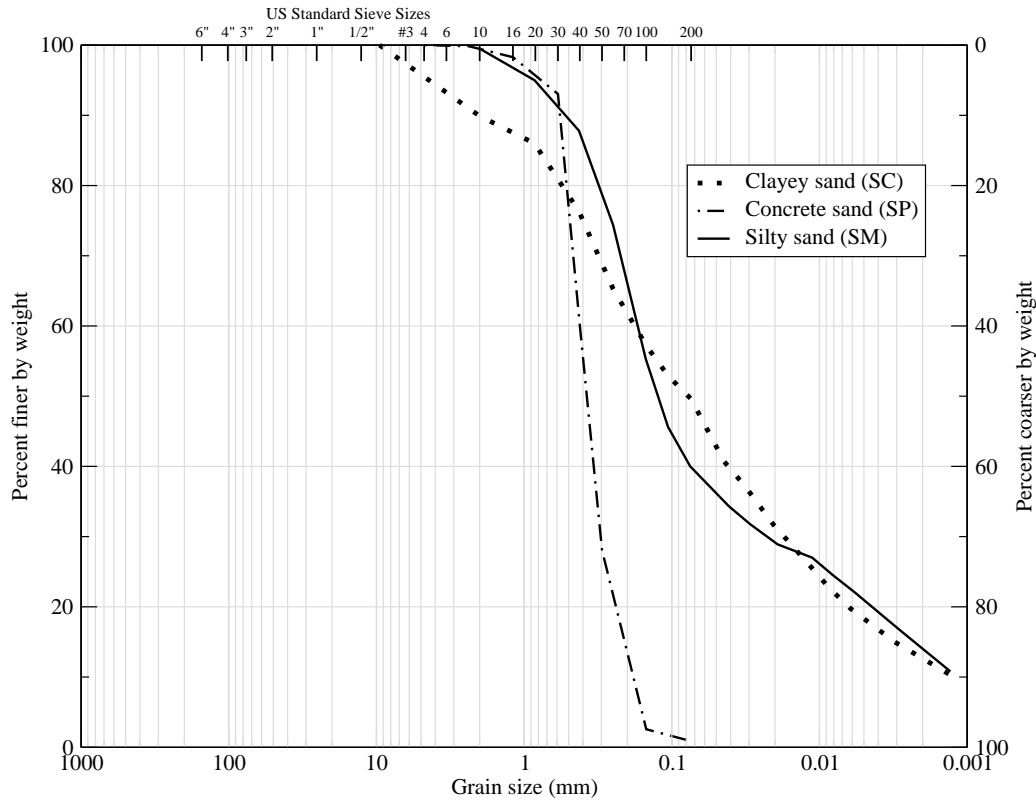


Figure 5.2: Particle size distributions for the three soils used in this work.

The soils used were poorly graded sand, silty sand, and clayey sand or, as defined according to the Unified Soil Classification System (USCS) ERDC (1960), soils designated as SP, SM, and SC, respectively. The USCS is a system used in geology and geotechnical engineering to characterize and compare soil and gravel based on their particle size distributions and consistencies.

Particle size distributions are determined using a vibrating platform by placing the soil on top of a series of progressively finer sieves and observing the proportion of the soil retained on each of the sieves and, subsequently, for determination of particle size distributions of particles less than a nominal size of 0.075 mm, using a hydrometer test. Figure 5.2, shows the experimentally obtained gradation plots for the skeletal materials of the three soils used in this work.

It can be seen that the particle size distribution of the the poorly graded concrete sand was much narrower than those of the other two soils. In other words there was much less diversity in particle size for the concrete sand than for the other materials. Furthermore, Figure 5.2 shows that both of the other soils, the silty sand and the clayey sand, contained large fractions of particles that were much finer than those that comprised the skeleton of the concrete sand.

Soil consistency is quantified in terms of plasticity index and liquid limit. The plasticity index is the the range of water contents for which the soil behaves like a plastic solid. The liquid limit is the water content at which the behavior of a soil changes from being predominantly like a plastic solid to being more like a fluid. The poorly graded sand and the silty sand used in this research exhibited no plasticity; the clayey sand exhibited a plasticity index of 8 and a liquid limit of 27.

Quasi-static experimental determination of the properties of various soils at various states was performed for related project work by colleagues at the US Army Engineer Research and Development Center (ERDC) (see, for example, Corps of Engineers (1980); Ehrgott (2011b)) in order to more accurately predict, computationally, the results of the blast experiments. All of the various soil mechanical property test data sets, used for the computations, were determined by means of tests that involved uniaxial strain (UX) stress-strain, stress path, and pressure volume relations and triaxial compression (TXC) failure relations. A minimum of 11 remolded soil specimens were tested for each soil type and emplacement condition for the purpose of determining mechanical properties used in the soil material models.

Prior to conducting the mechanical property tests, the height, diameter, and weight of each remolded test specimen were determined. These measurements were used to compute the specimen's wet or bulk density. Measurements of post test water content were conducted in accordance with procedures given in Corps of Engineers (1980). The values of dry density, porosity, degree of saturation, and volumes of air, water, and solids were calculated from

the values of post test water content, wet density, and specific gravity.

The laboratory mechanical property tests were performed under quasi-static conditions using axial strain rates between 10^{-4} and 10^{-5} sec^{-1} and times to peak load between 5 and 30 min. Mechanical property data were obtained using several stress and strain paths. Undrained volumetric stress-strain data were obtained during the hydrostatic loading phases of the triaxial compression tests and from the hydrostatic compression (HC) tests.

Shear and failure data were generated by means of unconsolidated-undrained TXC tests. One-dimensional compressibility data were obtained using undrained UX tests with lateral stress measurements. The terms undrained and unconsolidated refer to tests for which no pore fluid (liquid or gas) was allowed to escape or drain from the membrane-enclosed specimens.

Empirical relations were derived based on the experimentally determined water content and yield surfaces of the various soils. These relations were in the form of semi-logarithmic least squares fit between the mean yield strength and the water content of the soils. The yield strength of the soils was a function of the soil water content and decreased with increasing water content (Figure 5.3) to the limit of no strength that was observed for the case of pure water.

The relation between the mean yield strength of the poorly graded sand and its water content (with best fit relation $YS = 2609 \exp(-0.199w)$, where $YS \equiv$ yield strength and $w \equiv$ water content) was somewhat different than those for the clayey sand and the silty sand, both of which contained higher fines contents (with best fit relation $YS = 675 \exp(-0.474w)$). This was, in part, a result of some of the innate differences between the fabric behavior of the poorly graded sand and the more readily compressed fines-containing silty sand and clayey sand.

Part of this difference was also a result of the different approach required for modeling the yield strength of the poorly graded sand due to difficulties in triaxial test sample prepa-

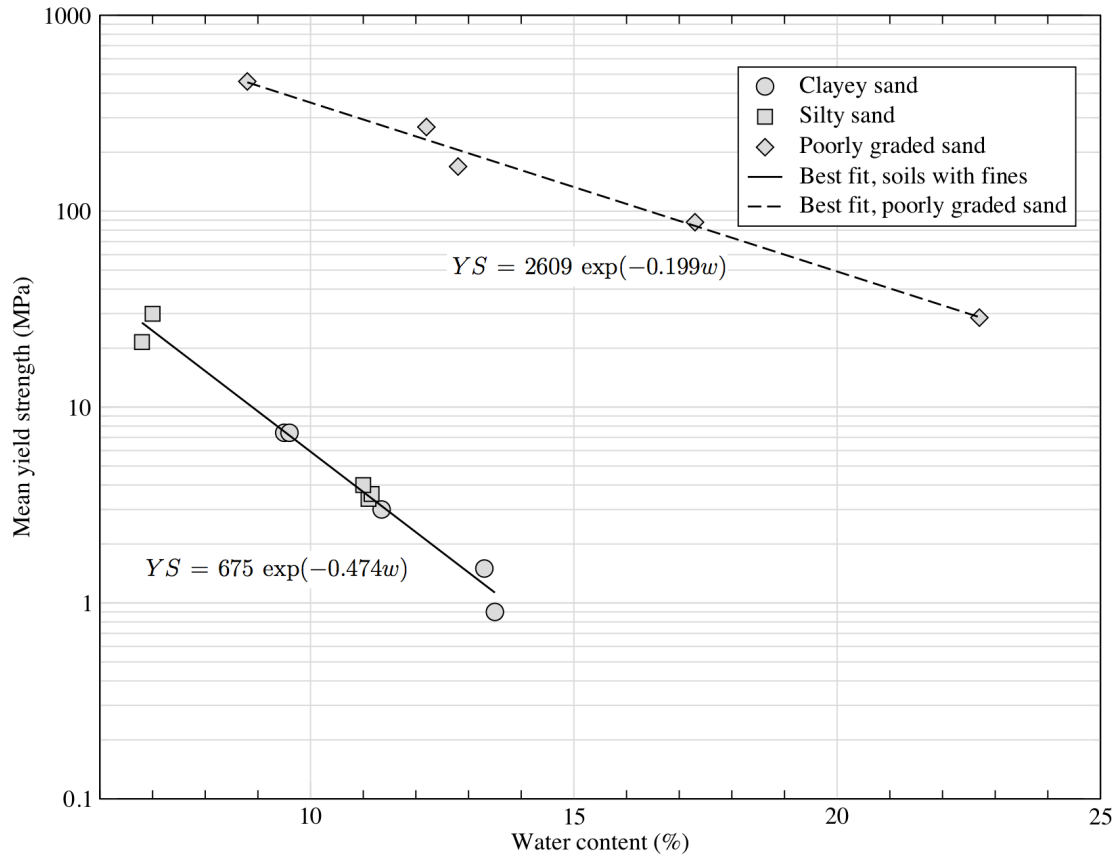


Figure 5.3: Relation between mean yield strength and initial soil water content. In the empirical best fit relations YS represents yield strength and w denotes water content.

ration because of the greater permeability of the more porous material to the interstitial flow of water. The silty sand and the clayey sand could be tested directly for determination of the yield surface. On the other hand, it was necessary to combine test results for relatively dry sand with effective stress theory in order to estimate the yield surface for various states of the poorly graded sand.

5.3 Computational approach

5.3.1 Computational procedures

The computational techniques and constitutive behavior descriptions used for the present analyses were similar to those described in Section 4.3.1 except for some of the details regarding the constitutive treatment of the soils for the various emplacement conditions. As was the case with the investigation of the excitation of sand and water in Chapter 4, it was possible to take advantage of the axial symmetry of the problem in order to use a two-dimensional mesh for calculations.

5.3.2 Constitutive models

The approach used for predicting above ground loads transmitted to above ground targets from shallow buried explosives was to model the explosive, the surrounding soil, the air above the soil and the above ground aluminum plate. The behavior of water, air, and explosive during these sorts of blast events was modeled in the same way as in Chapter 4.

The approach used for the constitutive treatment of the soil involved quasi-static experimental determination of the properties of various soils at various states (see Section 5.2.3) in order to emulate, computationally, the behaviors of the soils used in the blast experiments. Laboratory mechanical properties of the test bed soils were determined at various combinations of density, air filled voids volume fraction, and water content.

For the silty sand and clayey sand test bed materials a series of mechanical property tests were conducted by colleagues at the US Army Engineer Research and Development Center in Vicksburg, MS, for related project work, for density - water content - air void combinations intended to span the range of air filled voids contents used in the small scale

Table 5.4: Soil models used for computations. These were based on experimentally determined mechanical properties. Poorly graded sand properties were derived from experimentally determined dry sand properties using effective stress theory.

Soil type	Initial volume fraction air	Water content (%)	initial wet density (kg/m ³)
SP	0.047	22.7	1949
SP	0.142	17.3	1844
SP	0.200	12.8	1801
SP	0.230	12.2	1746
SP	0.268	8.8	1728
SM	0.047	11.1	2210
SM	0.142	11.16	1990
SM	0.191	11.0	1876
SM	0.219	6.8	1915
SM	0.260	7.0	1808
SC	0.096	13.5	2010
SC	0.199	13.3	1756
SC	0.209	9.5	1840
SC	0.212	11.35	1790
SC	0.268	9.6	1700

blast tests. For the case of the poorly graded sand, test results for sand evaluated at one emplacement condition - relatively dry with 4% water content and 30% air filled voids content - were used in combination with effective stress theory (Zimmerman et al., 1993) to calculate the mechanical properties used for the sand constitutive models in this work (Table 5.4), which were also intended to cover the range of air voids contents used in the blast tests.

In physical tests for determination of the soil properties, the volumetric behavior of various soils was examined using confining pressures to 200 MPa and then, beyond this level of pressure, volumetric behavior was defined using a fit based on the Hugoniot for water and for the solid constituents of the soil. The hydrostats used in the computational models went to pressures of 5 GPa. The soil constitutive models were implemented into LS-DYNA for subsequent blast calculations.

The hydrostat was defined by input of data pairs - pressure as a function of natural

volumetric strain - to the solver. The solver performed numerical differentiation of these tabulated data to calculate bulk modulus as a function of volumetric strain. The hydrostatic behavior was treated as being hypoelastic with variable bulk modulus and constant Poisson ratio.

Examples of the hydrostatic behavior of the various materials investigated are shown in Figures 5.4 and 5.5. Figure 5.4, shows a peak pressure scale of 200 MPa in order to help the reader to see the differences in lower pressure behavior between the soils with fines and the poorly graded concrete sand and to also notice the similarity in lower pressure behavior between the clayey sand and the silty sand.

The hydrostats for the partially saturated soils used in this work are very similar in form to the one used in the previous chapter for the partially saturated sand. In Figures 5.4 and 5.5, it can be seen that at lower levels of volumetric strain, the soil is more compliant and, at strains exceeding that at which the initially present air filled voids vanish and the soil reaches a state of saturation, the soil becomes much more stiff. It can also be seen that the level of strain, the saturation strain, at which this change in stiffness occurs is related to the initial air filled voids content of the soil.

The laboratory soil mechanical properties for various combinations of water and air filled voids content were implemented into LS-DYNA for subsequent blast calculations. The hydrostatic behavior was treated as being hypoelastic with variable bulk modulus and constant Poisson ratio (Rohani, 1977). The relationship between the stress increments $d\sigma_{ij}$ and the strain increments $d\epsilon_{ij}$ was

$$d\sigma_{ij} = K d\epsilon_{kk}\delta_{ij} + 2 G \left(d\epsilon_{ij} - \frac{1}{3}d\epsilon_{kk}\delta_{ij} \right) \quad (5.4)$$

where K was variable bulk modulus, and a constant Poisson ratio ν was used so that the variable shear modulus $G(K, \nu)$ was given by

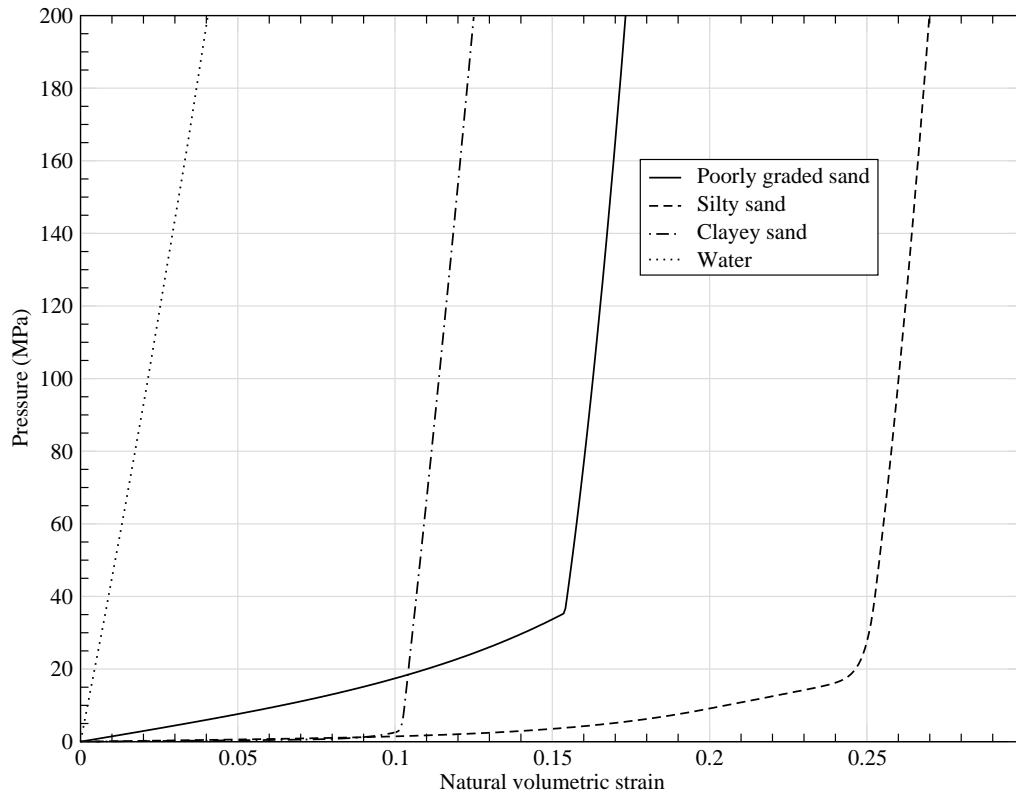


Figure 5.4: Typical soil hydrostats for pressures up to 200 MPa. Example hydrostats are shown for poorly graded sand (14.2% air filled voids, 17.3% water content), silty sand (21.9% air filled voids, 6.8% water content), clayey sand (9.6% air filled voids, 13.5% water content), and water.

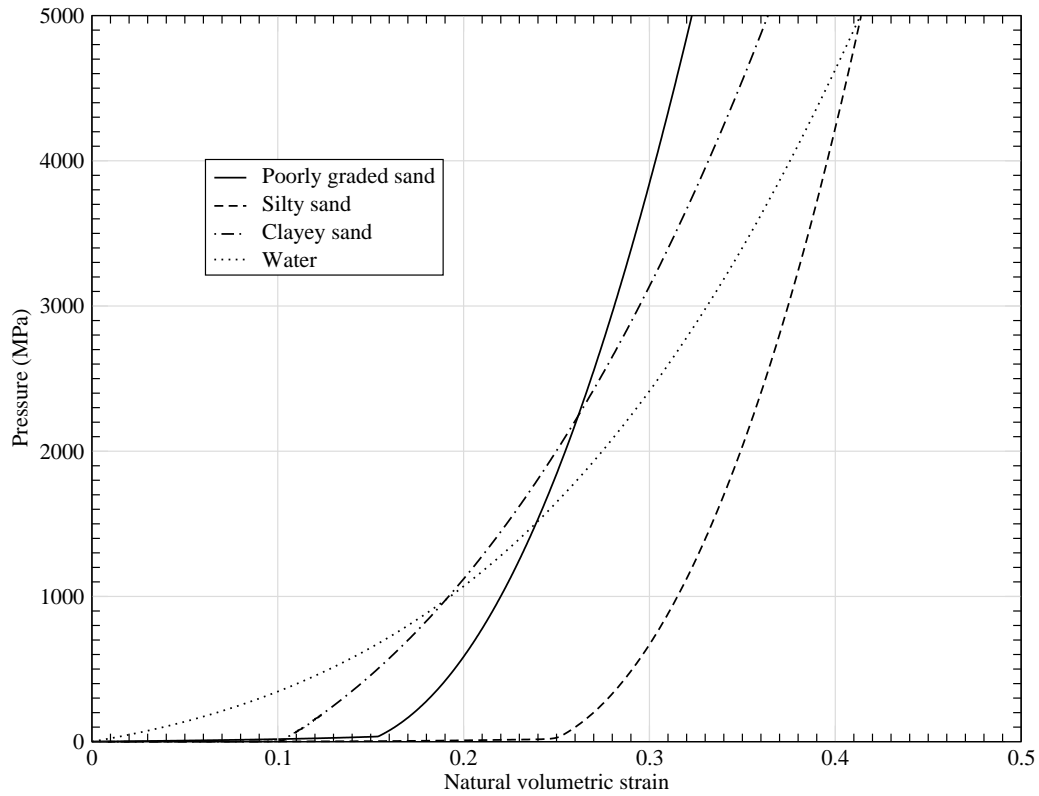


Figure 5.5: Typical soil hydrostats for pressures up to 5 GPa. Example hydrostats are shown for poorly graded sand (14.2% air filled voids, 17.3% water content), silty sand (21.9% air filled voids, 6.8% water content), clayey sand (9.6% air filled voids, 13.5% water content), and water.

$$G(K, \nu) = \frac{3K(1 - 2\nu)}{2(1 + \nu)}. \quad (5.5)$$

The volumetric constitutive properties of the soils were input to the solver in tabular form. The data input to the table consisted of pressure - natural volumetric strain pairs. These data for the soils were differentiated numerically by the solver to yield the bulk and shear moduli that were used in the ALE finite element calculations.

Figures 5.6 and 5.7 show examples of the deviatoric yield behavior of the fine-grained soils and the poorly graded sand that were examined. The soil behavior was elastic-perfectly plastic. The yield function for the silty sand and the clayey sand were given by (DiMaggio and Sandler, 1971)

$$f(p, J'_2) = \sqrt{J'_2} - [\alpha - \gamma \exp(\beta p)] = 0 \quad (5.6)$$

where p is the pressure, J'_2 is the second invariant of the deviatoric stress tensor, and α , β , and γ are constants for a given soil and soil state. α , β , and γ were, fit by means of results from unconsolidated, undrained triaxial test results.

The deviatoric behavior of the partially saturated poorly graded sand was estimated using effective stress theory based on the assumption that once air-filled void content becomes zero, the hydrostatic loading is carried primarily by the water and the effective stress - the stress imparted to the soil skeleton - increases only moderately with increases in total pressure (Zimmerman et al., 1993; Lambe and Whitman, 1968). As a result of this, the shear resistance of the soil skeleton increases much less at total pressures beyond the pressure at saturation compared to increases it would exhibit when dry. For the cases involving partially saturated, poorly graded sand, the yield surface was somewhat similar to that given in Equation 5.6 except that the yield relation beyond saturation was determined differently as is reflected in the somewhat different shape of the yield surface beyond saturation.

At pressures below saturation pressure, in the initially partially saturated sand, at

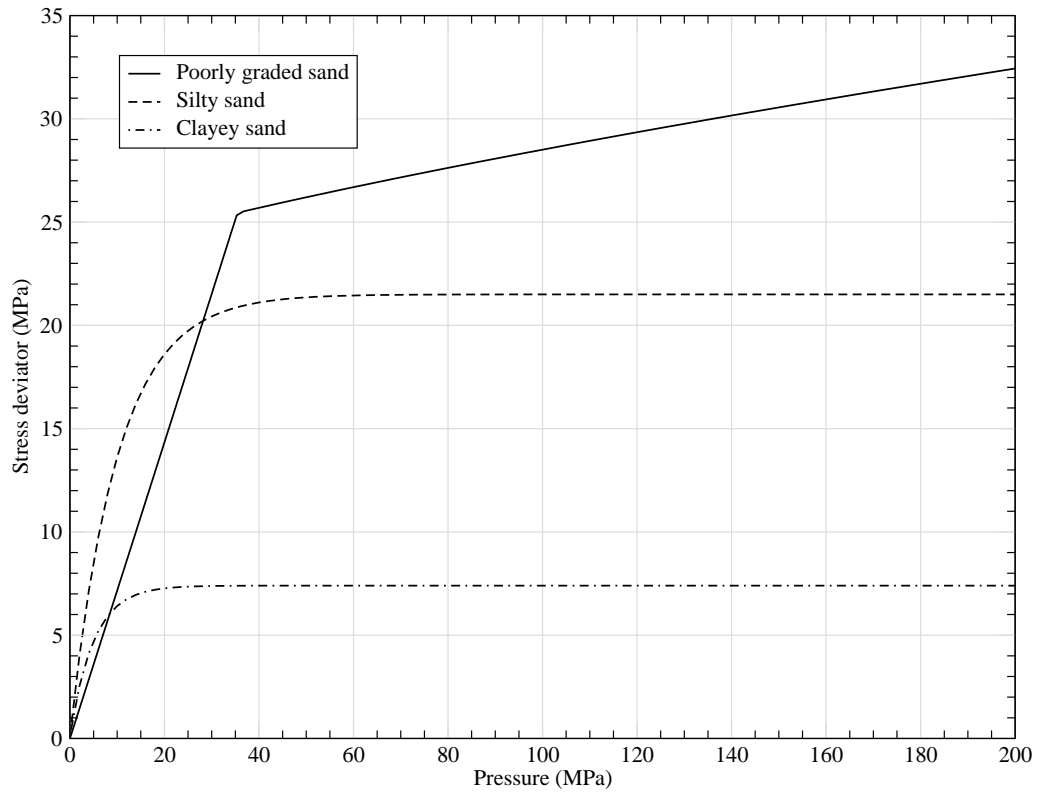


Figure 5.6: Typical soil yield surfaces up to 200 MPa pressure. Example yield surfaces are shown for poorly graded sand (14.2% air filled voids, 17.3% water content), silty sand (21.9% air filled voids, 6.8% water content), and clayey sand (26.79% air filled voids, 9.6% water content).

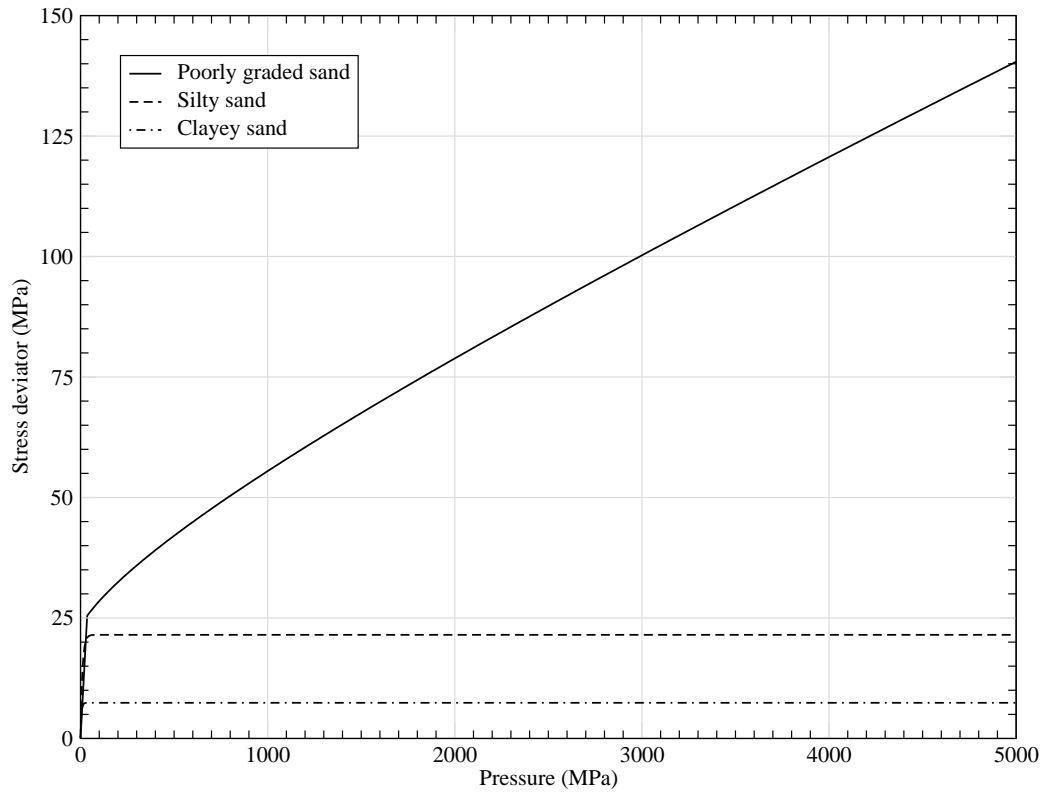


Figure 5.7: Typical soil yield surfaces up to 5 GPa pressure. Example yield surfaces are shown for poorly graded sand (14.2% air filled voids, 17.3% water content), silty sand (21.9% air filled voids, 6.8% water content), and clayey sand (26.79% air filled voids, 9.6% water content).

which the air filled voids disappear and the soil becomes saturated, the yield behavior is very similar to that of dry sand. At pressures beyond this point, the yield behavior is defined by the effective pressure, that is the pressure acting on the soil skeleton, defined as $p_e \equiv p_t - u$ where p_t is the total pressure and u is defined as the pressure supported by the water in the pores of the soil. Using effective stress theory, it was possible to estimate the yield behavior of the partially saturated sand at various combinations of water content and air filled voids content Zimmerman et al. (1993).

For the example soils shown in Figure 5.6, scaled to pressures up to 200 MPa, it can be seen that, at lower pressures, the yield surfaces could be represented, in principal stress space, as being similar to the pressure-dependent cones suggested by Drucker and Prager (1952), with yield strength increasing linearly with pressure. At higher pressures, the yield strength remained constant for the case of the silty and clayey sand models. For the case of the model used for the poorly graded sand it can be seen that at higher pressures the yield point increases much less rapidly than at lower pressures. Figure 5.7, shows the example yield surfaces scaled to pressures of 5 GPa, the upper limit of the prescribed pressure used in the tabulated LS-DYNA constitutive models.

5.4 Comparison of experimental and computational results

Figure 5.8 gives a comparison of the test bed air filled void content with experimentally determined target momentum results for beds containing water as well as for beds containing the three soils at various emplacement conditions. This figure also shows an estimate of the experimental data mean values, as a function of air filled volume fraction, which were calculated by means of a second order polynomial using a least squares fitting algorithm (Carnahan, Luther, and Wilkes, 1969), and the 95% prediction limits based on the second order polynomial (Oberkampf and Roy, 2010). It was observed that a relation between air filled voids volume fraction and momentum transferred to a target held, experimentally, for water, which was treated as having no air filled voids, as well as for all three of the soil types that were used in these investigations.

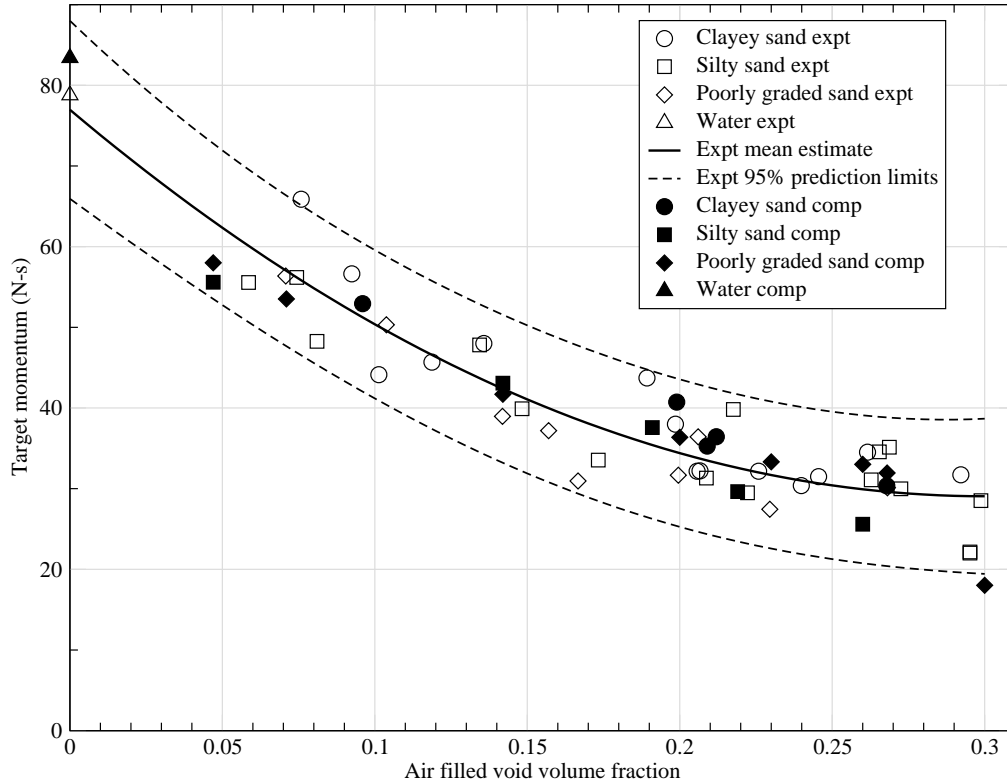


Figure 5.8: Comparison of experimental data, of predictions of experimental mean values, and of computational results for 304.8 mm diameter plates. Target momentum, independent of test bed material type, decreased with increasing air filled void volume fraction.

Based on analyses described below, this relationship was found to be, at least in part, associated with the behavior that involved a very large increase in the stiffness of the soil once its air void volume approached zero. The soils with lower initial air void volume fraction reached this point at lower levels of strain than did soils with higher initial air void volume fraction. This resulted in higher soil mass flow rates out of the soil beds and, as result, increased target momentum for soils with lower initial air filled voids content.

Computations were performed according to the setup in Figures 4.1 and 5.1, for water and for the three soils at various emplacement conditions and, again, it was seen that there was a very significant correlation between decreasing initial volume fraction of air filled voids and increasing target momentum. Figure 5.8 compares the results from the computations to the data and gives estimates for the mean values from the experiments.

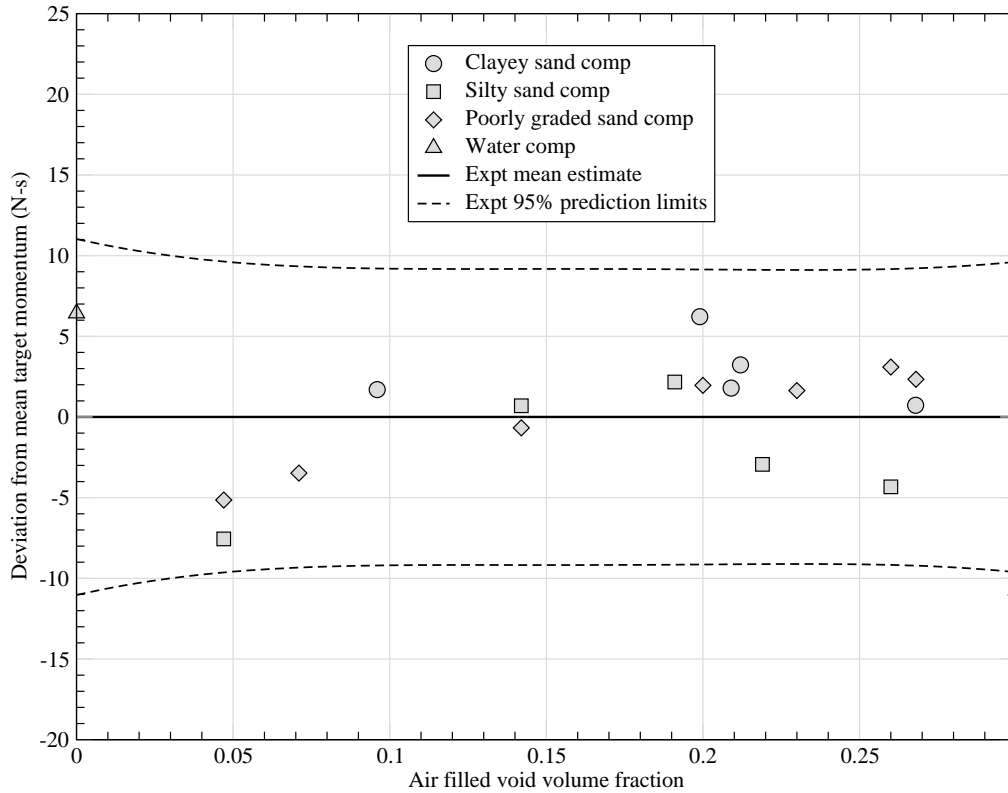


Figure 5.9: Deviation between computational results and second order polynomial estimate of mean value from blast experiments. 95% limits are bounds for the prediction limits based on the blast experiment data.

Figure 5.9, offers an attempt to give a better sense of the accuracy of the computational momentum as compared to the mean values of the experimental momentum as a function of air filled void content.

The ordinate in Figure 5.9, in other words, the deviation from the mean target momentum, is defined as the algebraic difference between a particular momentum, for example, a computationally determined momentum, and the second order polynomial estimate of the experimentally determined momentum (cf. Oberkamp and Roy (2010)). It can be seen that, except for the case of the 30% air filled void content poorly graded sand, the values of the computations fell within the 95% limits for prediction derived from the experimentally determined momentum results.

Table 5.5: Starting points, for each of the three soil types, for the computational sensitivity studies.

Soil type	Initial volume fraction air	Water content (%)	Natural volumetric strain at lock-up	Mean yield strength (MPa)	initial wet density (kg/m ³)
SP	0.200	12.8	0.223	168.86	1801
SM	0.191	11.0	0.212	4.00	1876
SC	0.209	9.5	0.234	7.39	1840

5.5 Sensitivities to yield surface, hydrostat, and bulk density

Further computations were performed to investigate the sensitivity of the target momentum to variation of the initial density, the yield surface, and the hydrostat of the test bed soil. As was discussed in Section 5.3.2, constitutive models, based on experimental data, were developed at five different soil emplacement conditions for each of the three soil types. For each of the three soil types, the constitutive model associated with the median volume fraction of air voids was used as a starting point for the sensitivity studies (Table 5.5). Sensitivities were then estimated by separately adjusting the yield surface, the hydrostat, and the density to those of the models for each of the other four levels of air voids for each of the soils. The various levels of metrics associated with the key characteristics of the soil models used for the sensitivity studies are summarized in Table 5.6.

Figure 5.10 and Table 5.7, show the computational sensitivity of the target momentum to the mean yield strength of the soil. Mean yield strength was calculated as

$$Y_{mean} = \frac{\int_0^{p_{max}} Y(p) dp}{p_{max}} \quad (5.7)$$

where $Y(p)$ is the pressure dependent yield surface and p_{max} was 5 GPa, the maximum pressure prescribed in the hydrostat and yield surface tables.

The mean yield strength of all three soil types had a strong influence on the momentum imparted to the targets, with the momentum decreasing with increasing yield strength.

Table 5.6: Characteristics of soil models used for sensitivity study.

Soil type	Initial volume fraction air	Water content (%)	Natural volumetric strain at lock-up	Mean yield strength (MPa)	initial wet density (kg/m ³)
SP	0.047	22.7	0.048	28.61	1949
SP	0.142	17.3	0.153	87.82	1844
SP	0.200	12.8	0.223	168.86	1801
SP	0.230	12.2	0.261	268.80	1746
SP	0.268	8.8	0.312	459.41	1728
SM	0.047	11.1	0.048	3.40	2210
SM	0.142	11.16	0.153	3.60	1990
SM	0.191	11.0	0.212	4.00	1876
SM	0.219	6.8	0.247	21.46	1915
SM	0.260	7.0	0.301	29.94	1808
SC	0.096	13.5	0.101	0.90	2010
SC	0.199	13.3	0.222	1.50	1756
SC	0.209	9.5	0.234	7.39	1840
SC	0.212	11.35	0.238	3.00	1790
SC	0.268	9.6	0.312	7.39	1700

The range of variation in momentum for the poorly graded sand as well as for the two soils with fines - silty sand and clayey sand - was about 15 N-s over the range of yield strength evaluated. This was because decreasing yield strength promotes an increasing rate of flow of the substrate material out of the soil bed thereby increasing tractions on the bottom surface of the target plate.

Figure 5.11 shows an example of the increase in flow rate resulting from a change in yield surface, 300 μ s after detonation, for the case of silty sand with mean yield strength of 3.4 MPa (Figure 5.11a) and 29.9 MPa (Figure 5.11b). First, it can be seen that, for the case of the lower yield strength, more material has been removed from the soil bed than was removed for the case of the 29.9 MPa mean yield strength.

It can also be seen that, as a result of the increased propensity toward flow of the lower yield strength soil, the annular region of soil above the initial top surface of the soil bed for that material has greater integrity than the annular region associated with the higher yield

Table 5.7: Computational sensitivity of target momentum to mean yield strength of soils. The prescribed bulk densities and hydrostats for each soil type were held constant; only the prescribed yield surfaces were varied.

Soil type	Mean yield strength (MPa)	Target momentum (N-s)
SP	28.61	49.5
SP	87.82	40.9
SP	168.86	36.4
SP	268.80	34.9
SP	459.41	33.3
SM	3.40	38.2
SM	3.60	37.9
SM	4.00	39.1
SM	21.46	29.8
SM	29.94	27.4
SC	0.90	43.5
SC	1.50	42.7
SC	3.00	38.9
SC	7.39	35.1

strength soil as is evidenced by the leakage of the detonation products at the top of the soil region (Figure 5.11b). Figure 5.12, based on finite element-based sensitivity calculations, shows that approximately twice as much soil was ejected from its original position for the case involving the material with the lower (3.4 MPa) yield strength than was ejected for the case of the higher (29.9 MPa) mean yield strength.

Part of this difference is also a result of the different approach required for modeling the yield strength of the poorly graded sand due to difficulties in triaxial test sample preparation because of the greater permeability of the more porous material to the interstitial flow of water. The silty sand and the clayey sand could be tested directly for determination of the yield surface. On the other hand, it was necessary to combine test results for relatively dry sand with effective stress theory in order to estimate the yield surface for various states of the poorly graded sand.

A very important characteristic of the volumetric high pressure compressive stress strain behavior of soils is the phenomenon of lock-up. Lock-up occurs, in an undrained soil

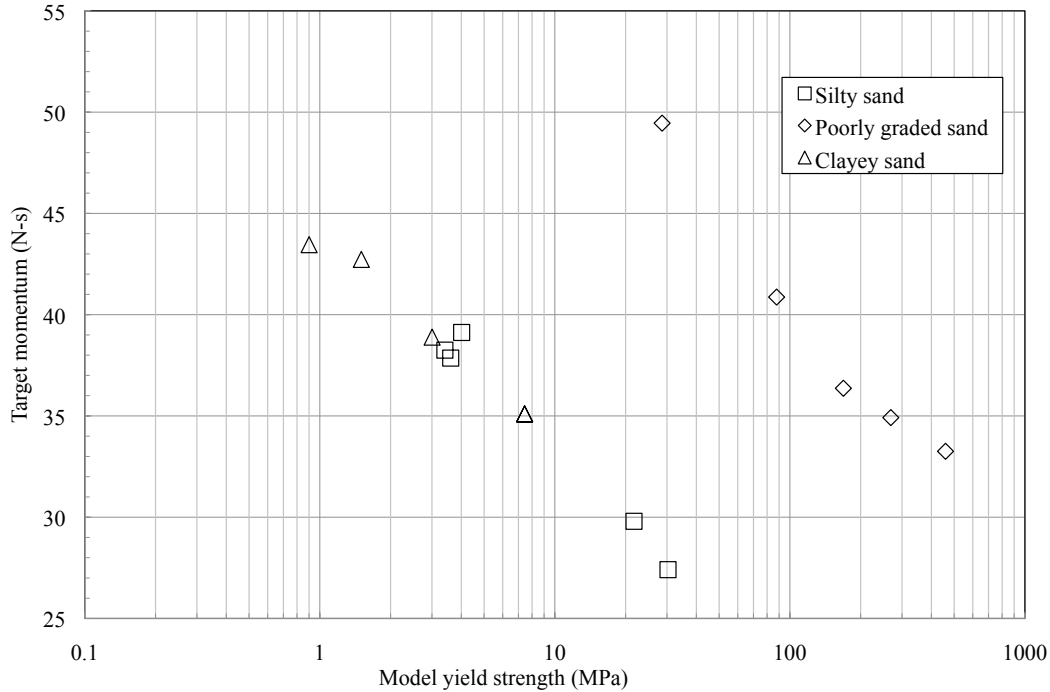


Figure 5.10: Computational sensitivity of target momentum to mean yield strength of soils. The prescribed bulk densities and hydrostats for each soil type were held constant; only the prescribed yield surfaces were varied. The range of momentum for the poorly graded sand as well as for the two soils with fines - silty sand and clayey sand - was about 15 N-s over the range of yield strength evaluated.

condition, at the level of pressure and compressive strain at which the air void volume fraction becomes vanishingly small thereby causing the bulk modulus to increase very significantly. Referring to the quasi-static, experimentally determined, hydrostats for silty sand in Figure 5.13, the lock-up points are seen to be at natural strain levels of 0.05, 0.15, 0.21, 0.25, and 0.30, respectively, for initial air filled void contents of 4.7, 14.2, 19.1, 21.9, and 26.0 percent.

The computational sensitivity of target momentum to the hydrostat - and thus to the lock-up point and air filled void content - is shown in Figure 5.14 and Table 5.8. The hydrostat influenced the target momentum at all levels of air filled void content; this sensitivity seemed to be more pronounced for initial volume fractions below about 0.2. Artyunov, Grigoryan, and Kamalyan (1985) suggested that the volume of the crater cuts they were

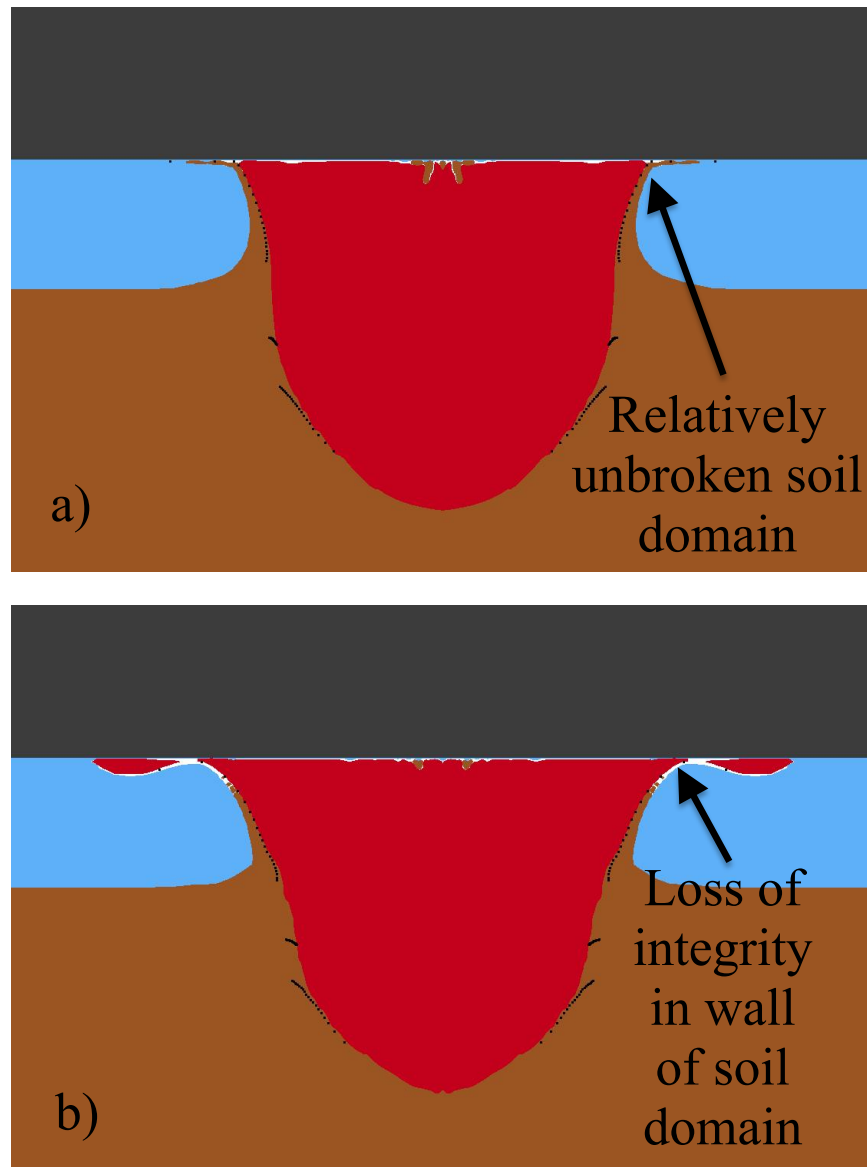


Figure 5.11: Effect of silty sand yield strength on flow and target loading at 300 μs . The grey material represents the rigid aluminum target, the light blue material the air, the red material the gaseous detonation reaction products, and the brown material the soil. a) 3.4 MPa soil mean yield strength; b) 29.9 MPa soil mean yield strength. For the case of the soil with lower yield strength, more soil was removed from its original position and was traveling toward - and loading - the rigid target (cf. Figure 5.12).

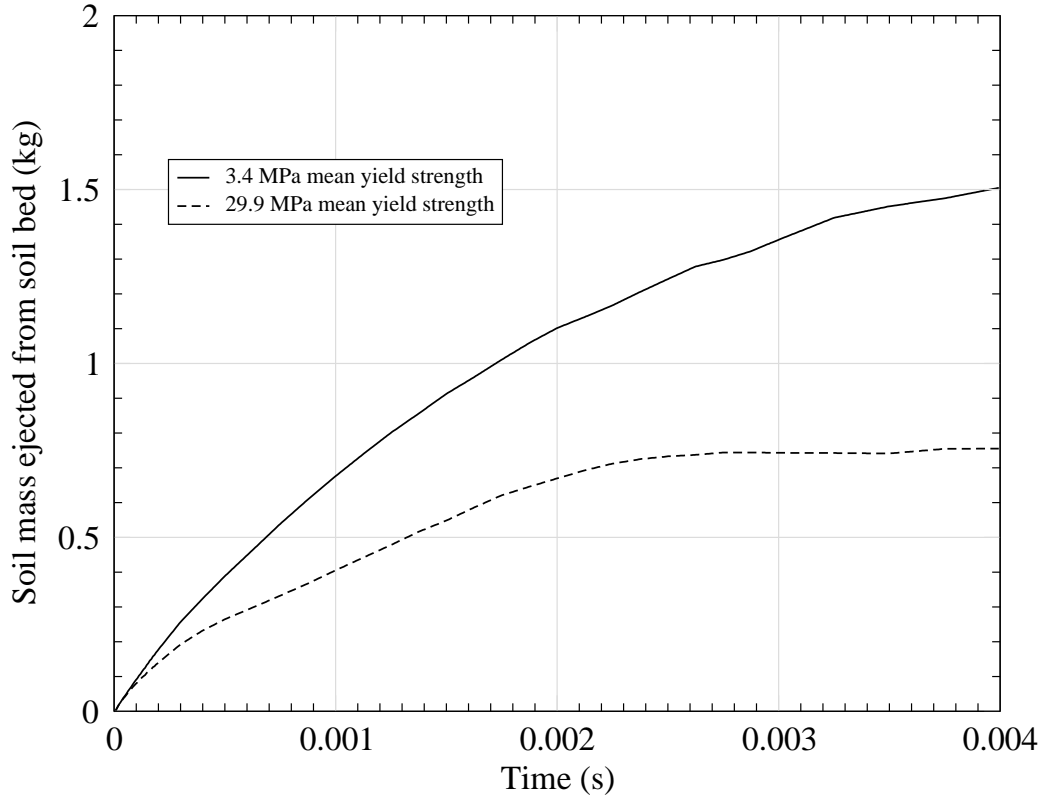


Figure 5.12: Effect of silty sand yield strength, based on the finite element computational sensitivity study, on the mass of soil ejected from the soil bed. Approximately twice as much soil was ejected from the bed containing the lower yield strength soil.

producing experimentally were comprised of the sum of the volume increase caused by compaction of the soil and of the volume increase that resulted from the movement of some of the soil out of the soil bed.

It seems correct to assume similarly that for the case of the present work part of the available mechanical energy available from the detonation of the explosive and expansion of the gaseous detonation products was expended in compressing the soil bed and that part of it was used to push some of the soil away from the soil bed. A portion of that energy that resulted in the ejection of the soil from the bed was then used to supply the tractions that imparted the momentum to and propelled the rigid target upward.

Referring again to Figure 5.13, one notices that the amount of mechanical energy required to perform a uniaxial compression of an element of soil by a particular volume

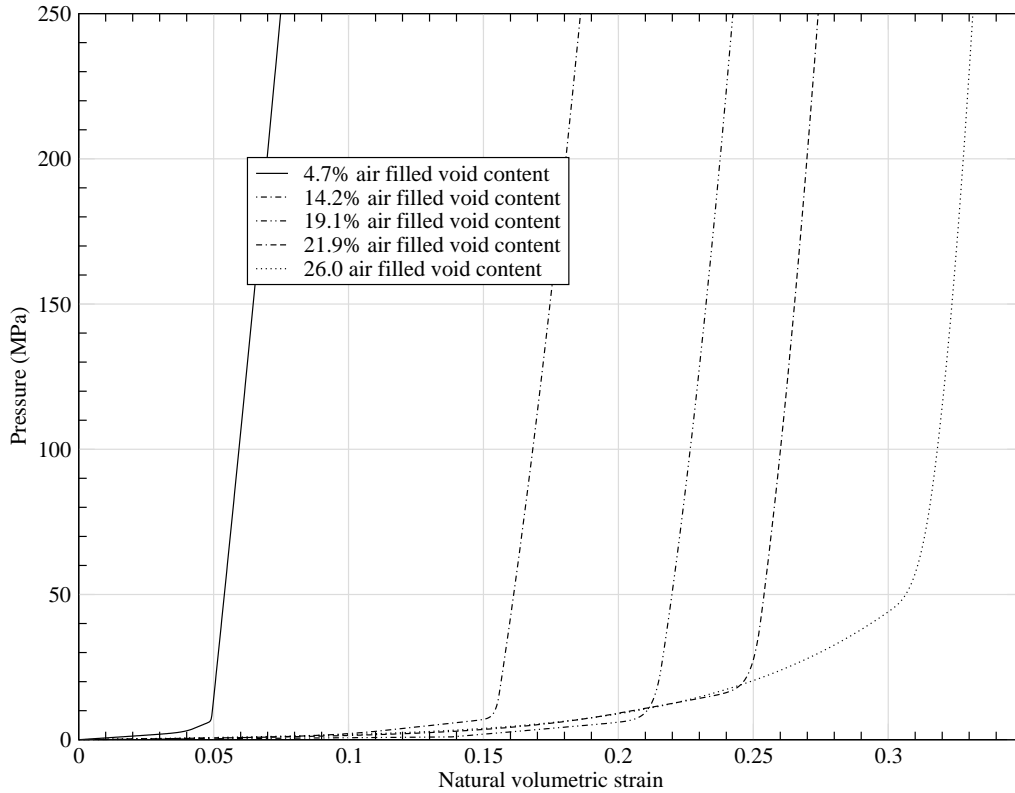


Figure 5.13: Variation of hydrostat lock-up position with changes in soil initial air filled void content for the case of silty sand. Lock-up strain increases with increasing air filled void content.

increment increases with decreasing levels of initial air filled void volume fraction. Lower air filled void content results in higher soil stiffness which forces more of the soil to move up and away from the bed and toward the target which, in turn, yields increased upward target momentum.

This is precisely what was observed in the results from the computations. Figure 5.15 shows a comparison of the computational results for silty sand 300 μ s after detonation. Figure 5.15a, shows results for the case of the 4.7 percent air filled voids hydrostat; in Figure 5.15b, for the hydrostat associated with an initial 26.0 percent air filled voids content. It can be seen that, for the case of the 4.7 percent air filled voids hydrostat, the amount of soil close to the boundary of the rigid target - and therefore able to produce tractions on the target boundary - is significantly greater than it is for the case of the 26.0 percent

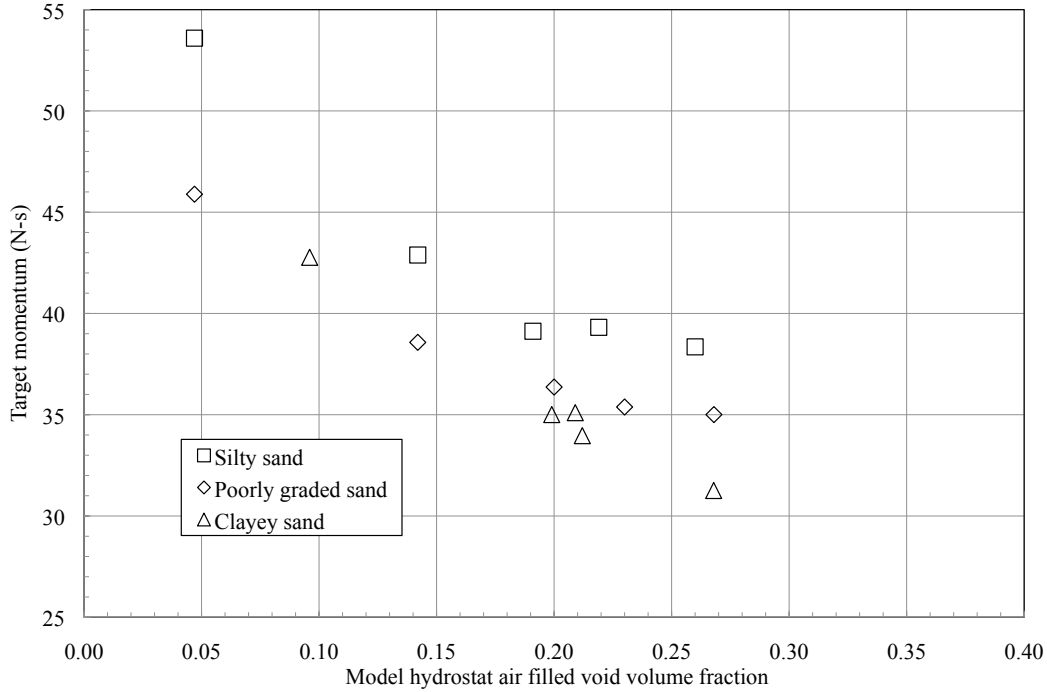


Figure 5.14: Computational sensitivity of target momentum to lock-up strain of soils. The prescribed bulk densities and yield surfaces for each soil type were held constant; only the prescribed hydrostats were varied. The range of momentum for the poorly graded sand as well as for the two soils with fines - silty sand and clayey sand - was about 15 N-s over the range of air filled voids that was evaluated.

hydrostat.

In fact, from the computational results it was noticed that there were actually some gaps containing no soil in the annulus comprised mostly of soil closest to the boundary of the target. It can be also be seen that when the initial air filled void content increased there was a substantial decrease in the amount of soil ejected from the test bed. In Figure 5.16 it can be seen that about two thirds more soil was ejected from the bed containing soil that initially had 4.7 percent air filled voids content than was ejected from the bed containing the soil that initially had 26 percent air filled voids content.

It has been generally considered, based to some degree on the work performed by Westine et al. (1985), that the mass density of a soil emplacement is the dominant factor with regard to momentum transfer. It should, however, be emphasized that the effects

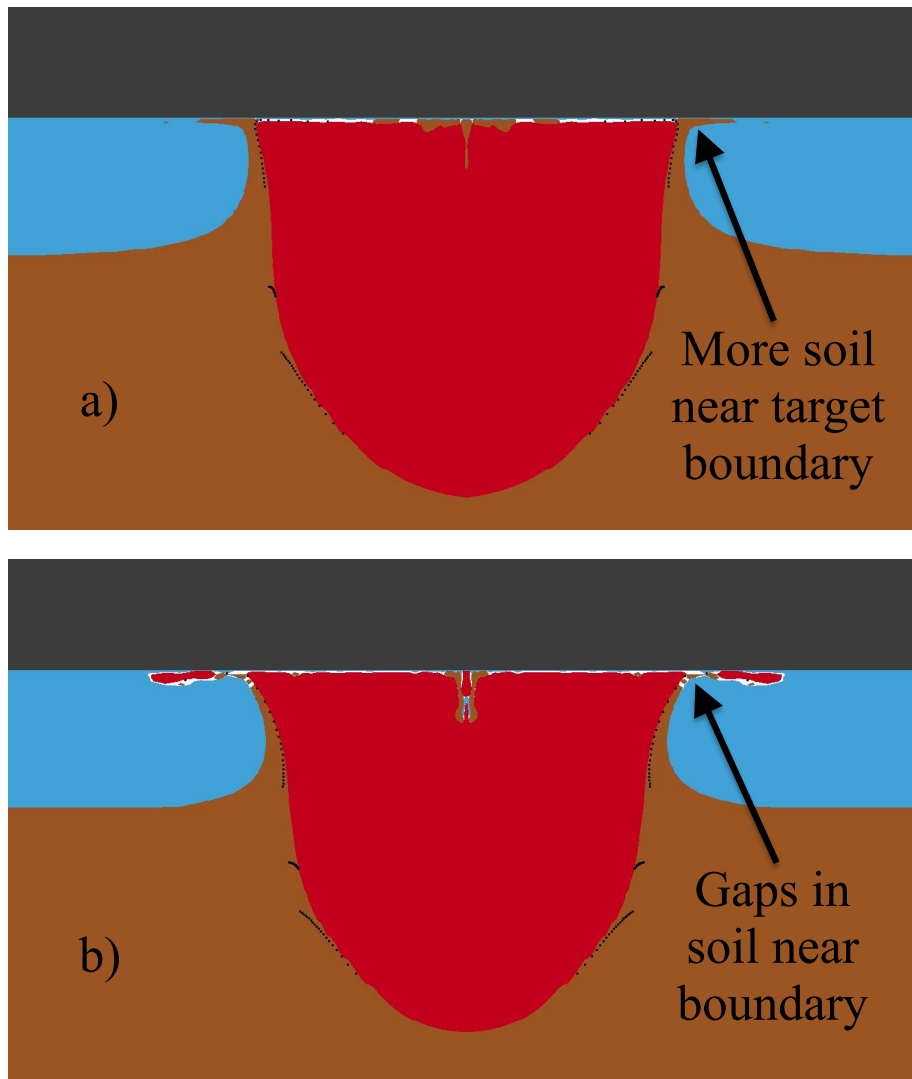


Figure 5.15: The effect of initial air filled void content on silty sand soil ejection and soil volume fraction 300 μ s after detonation. The grey material represents the rigid aluminum target, the light blue blue material the air, the red material the gaseous detonation reaction products, and the brown material the soil. a) 4.7 percent initial air filled voids content hydrostat (stiffer); b) 26.0 percent air filled voids hydrostat (softer). A greater proportion of the stiffer soil was ejected from the bed (cf. Figure 5.16). This resulted in higher target loading.

Table 5.8: Computational sensitivity of target momentum to lock-up strain of soils. The prescribed bulk densities and yield surfaces for each soil type were held constant; only the prescribed hydrostats were varied.

Soil type	Initial volume fraction air	Target momentum (N-s)
SP	0.047	45.9
SP	0.142	38.6
SP	0.200	36.4
SP	0.230	35.4
SP	0.268	35.0
SM	0.047	53.6
SM	0.142	42.9
SM	0.191	39.1
SM	0.219	39.3
SM	0.260	38.4
SC	0.096	42.8
SC	0.199	35.0
SC	0.209	35.1
SC	0.212	34.0
SC	0.268	31.3

of soil water content and air filled void content were not examined in that study. Figure 5.17 shows the sensitivity of target momentum to the initial wet or bulk density of the soil. There was a trend toward a moderate increase of momentum transfer with increasing initial bulk density but this sensitivity was clearly much less significant than the sensitivities to mean yield strength (Figure 5.10) and to hydrostat (Figure 5.14).

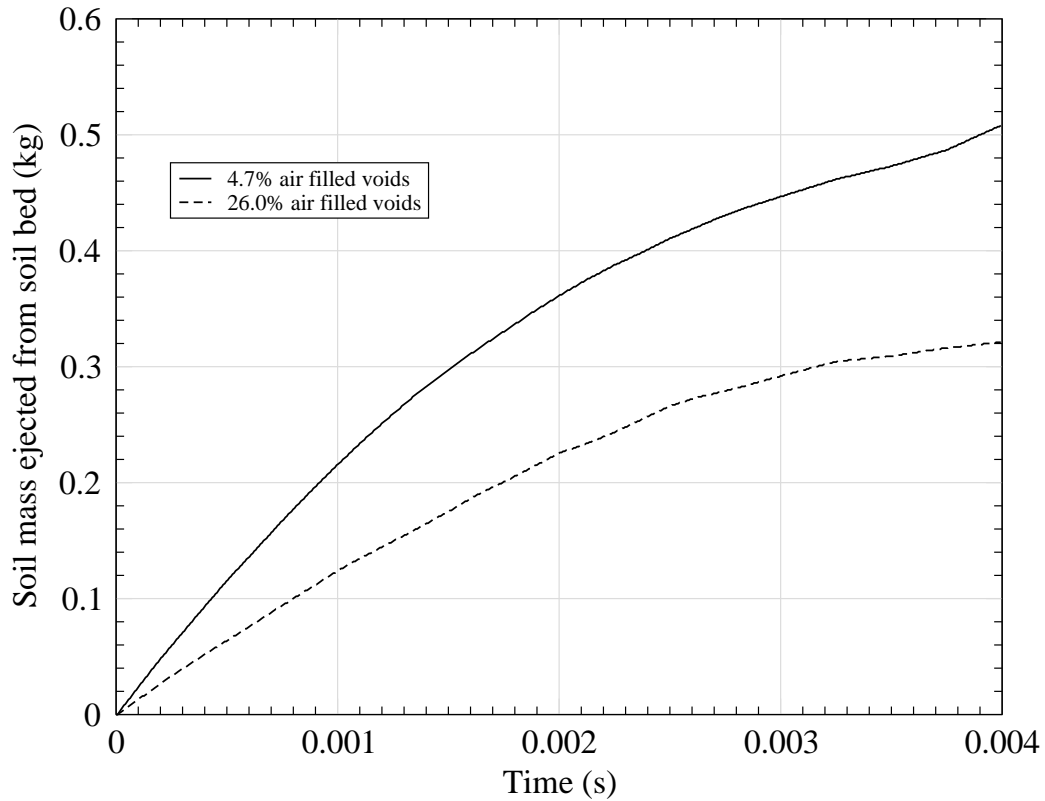


Figure 5.16: Effect of air filled voids content, based on the silty sand computational sensitivity study, on the mass of soil ejected from the soil bed. Approximately two thirds more soil was ejected from the bed containing the lower air filled void content soil.

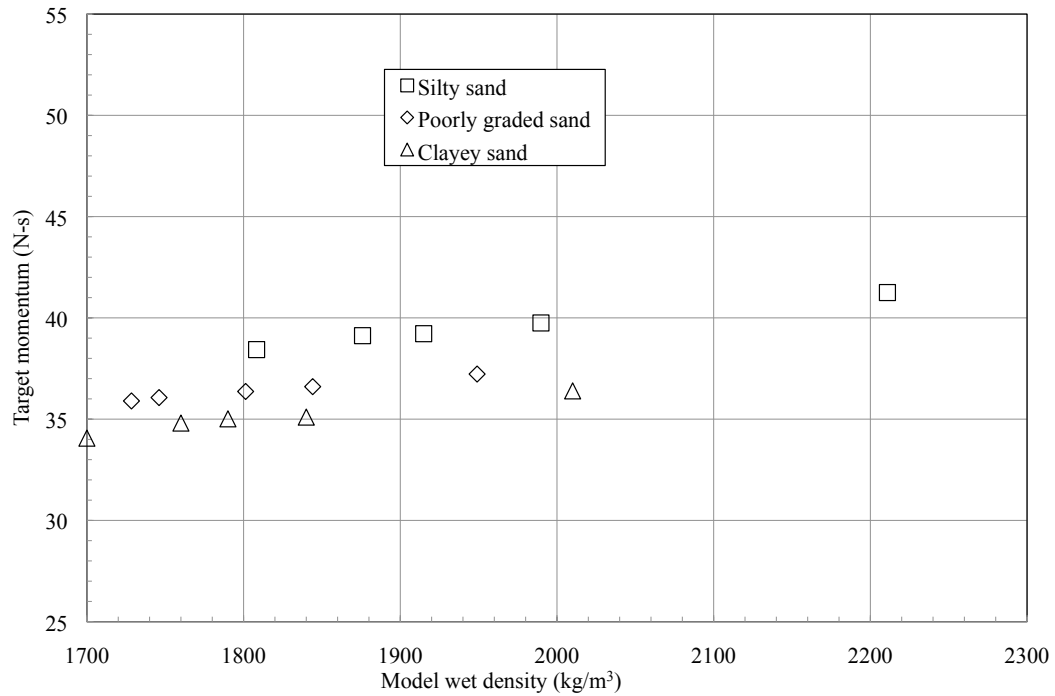


Figure 5.17: Computational sensitivity of target momentum to wet density of soils. The prescribed hydrostats and yield surfaces for each soil type were held constant; only the prescribed bulk densities were varied. The target momentum was less sensitive to initial wet density than it was to yield surface and pressure-volume lock-up point.

Table 5.9: Computational sensitivity of target momentum to wet density of soils. The prescribed hydrostats and yield surfaces for each soil type were held constant; only the prescribed bulk densities were varied.

Soil type	Wet density (kg/m ³)	Target momentum (N-s)
SP	1728	35.9
SP	1746	36.1
SP	1801	36.4
SP	1844	36.6
SP	1949	37.2
SM	1808	38.4
SM	1876	39.1
SM	1915	39.2
SM	1990	39.7
SM	2211	41.3
SC	1700	34.1
SC	1756	34.8
SC	1790	35.0
SC	1840	35.1
SC	2010	36.4

Chapter 6

Momentum transfer to more complex target geometries

6.1 Overview

Experimental and computational investigations were performed in order to better understand the mechanical response of rigid targets with various geometries to the detonation of shallow buried explosives. The focus of the present chapter is on the analysis, interpretation, and application of computational methods to better understand the mechanics behind experimentally observed results. The motion of the targets in response to loading from explosive buried in soil was measured experimentally by colleagues at the University of Maryland Dynamic Effects Laboratory using high-speed digital video photography (Fourney et al., 2010).

This work involved flat targets, targets that were downwardly convex, and targets that were downwardly concave with explosive charges located at various positions beneath the targets. It was observed that, in general, angled targets - whether downwardly concave or convex - tended to reduce the amount of momentum imparted to the center of mass of the targets. Computations were performed by use of an arbitrary Lagrangian-Eulerian treatment in a nonlinear finite element code. A model based on quasi-static test evaluations of poorly graded concrete sand was used for prediction of the soil behavior. The computational technique used for predicting blast response provided results that showed very good agreement with experiment.

The effect of variation of explosive lateral location relative to the centerline of the targets was examined, as was the effect of variation of the angle of concavity and convexity. Impulse response for downwardly concave models was compared with the response for downwardly convex targets in order to further investigate the question of whether the well known reduction in impulse for the downwardly convex topology is entirely due to an increased offset of target bottom surface from the soil surface or whether other reasons might also

affect blast response.

6.2 Experimental setup

The charge size and scale used for the work discussed in this chapter was found, from an experimental standpoint, to be easy to manage and to be appropriate for prediction of full-scale tests. Figure 6.1 illustrates the experimental setup used by Fourney et al. (2010) to measure the response of the rigid aluminum plates to the excitation of shallow buried explosive. The 636 mg explosive charges used for this work were constructed with of Detasheet C, which contributed 567 mg of the high explosive PETN, and an RP-87 detonator, which added another 26 mg of PETN and 43 mg of RDX so that the total amount of explosive added by the detonator was 69 mg.

Most of the mechanical energy from the detonation was provided by the Detasheet C. The cylindrical charges were inserted into a bed of wet concrete sand so that their top faces were 4.8 mm below the top surface of the sand. The rigid aluminum target plates were located in the desired conformation above the buried charge. The lowest point of each plate was positioned at the desired standoff distance, 21.6 mm, above the surface of the sand using either blocks of wood or stand off bolts.

The experimental work referenced in this chapter (Fourney et al., 2010) built upon the initial work done by Genson (2006), but included a deeper investigation of the effects of variation of charge location and target shape. The details regarding test bed preparation, explosive charge manufacture, and many aspects of the experimental procedures performed for the present work are contained in Genson's thesis. The charge size, depth of burial of the explosive, and distance from the soil surface to the bottom of the target would be expected to compare, using Hopkinson-Cranz scaling, with a full-size charge of 4.54 kg, a depth of burial of 93 mm, and a distance from soil surface to target bottom of 416 mm.

The displacements of markings on the corners of each of the plates were measured by use of high-speed digital video. These displacement measurements were used to calculate the velocities of the plates. The velocity values, in conjunction with the measured masses

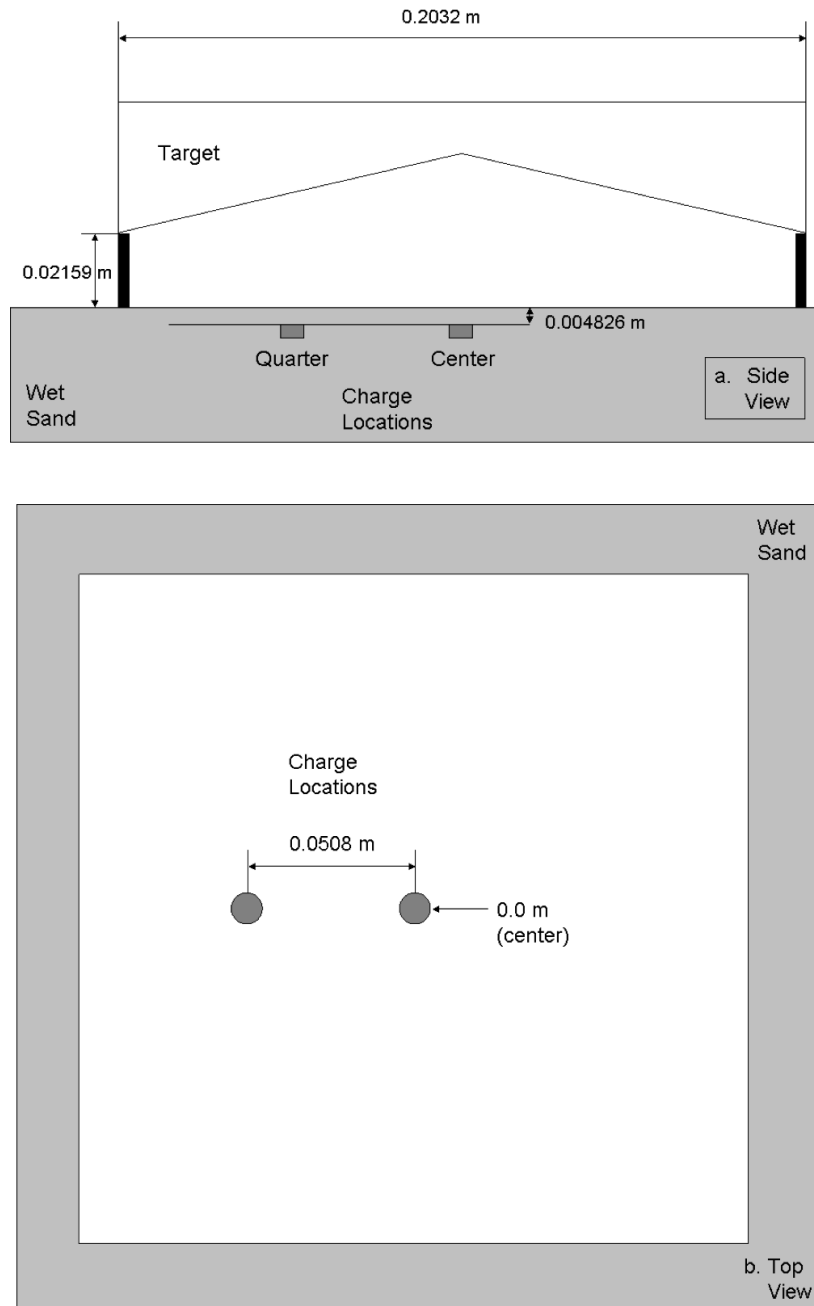


Figure 6.1: Experimental setup. 636 mg cylindrical explosive charges were buried to a depth of 4.8 mm in wet concrete sand and placed at various distances from the centerline of rigid aluminum targets. The vertical distance between the top surface of the sand and the lowest point of each of the 203.2 mm X 203.2 mm targets was 21.6 mm. Each test performed was a specific combination of one target geometry and one charge location. a. Side view. b. Top view.

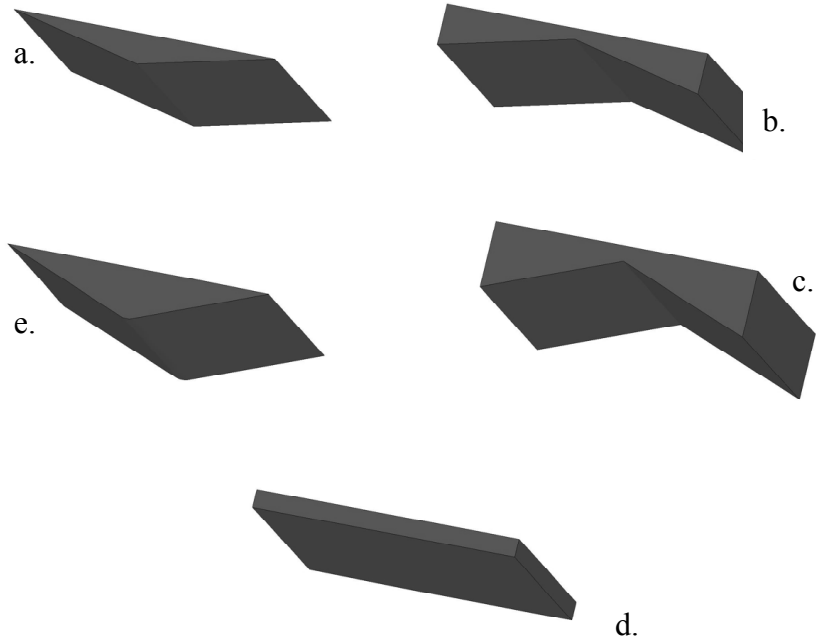
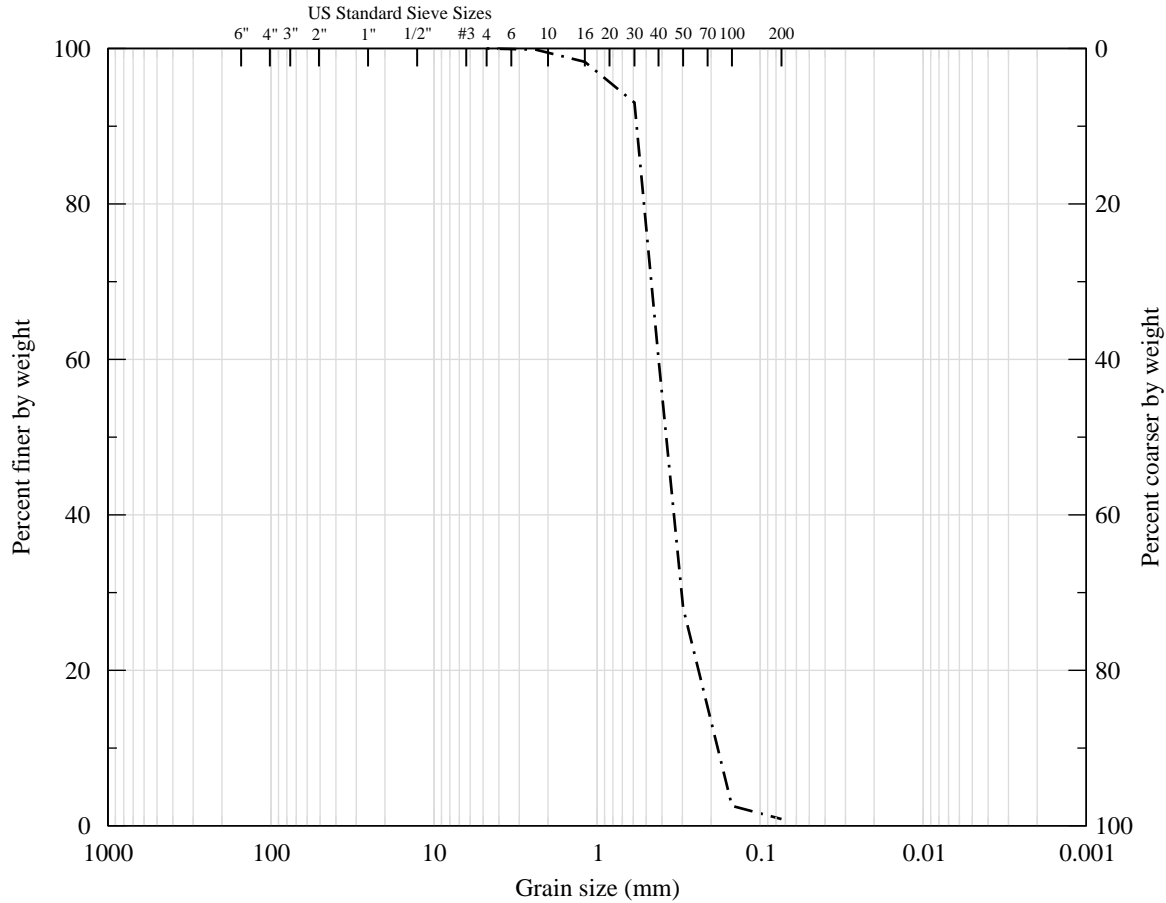


Figure 6.2: Target plate geometries, clockwise from top left, a. 13° convex down; b. 13° concave down; c. 21° concave down; d. flat; and e. 21° convex down. Targets were machined from aluminum alloy 6061 and shallow buried explosives were detonated at various locations beneath the targets. Target angle was defined as the initial angle between a target bottom half-surface and the horizontal plane.

of the targets were then used to determine the impulse imparted to the targets. Figure 6.2 shows the geometries of the plates that were tested. The plates were constructed of aluminum alloy 6061 and behaved essentially as rigid bodies in their response to the loading from the buried explosive. The plates were machined in such a way that all of them were of, nominally, 1.5 kg mass. The particle size distribution for the poorly graded concrete sand that was used was determined experimentally using a sieve test and is shown in Figure 6.3.

6.3 Computational domain model

The methods used for performing the computations with the wet and dry sand were similar to those described in Section 4.3 of this thesis. However, as a result of the lack of axial symmetry in the geometry of the targets (cf. Figure 6.2) it was necessary to perform the finite element ALE computations using a three-dimensional mesh. Figure 6.4 shows the three-dimensional, cylindrical mesh that was used for the ALE domain. The radius of the



energy are radially propagated in the plane of the cylinder. An unstructured mesh was used to model the problem.

A mesh convergence study was performed which involved excitation of the flat target by means of the explosive charge buried in wet sand directly beneath the center of the target. The results of this study indicated that the mesh with the nominally 2 mm center region was well within the converged region (Figure 6.5).

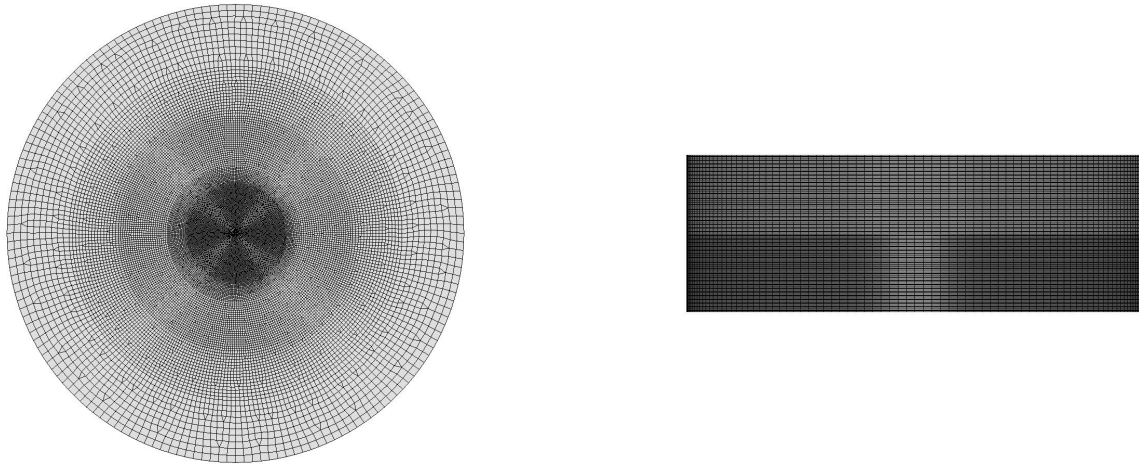


Figure 6.4: The mesh that was used for the three-dimensional ALE computational domain.

6.4 Effect of target geometry

A summary of the experimental results for the various targets is given in Table 6.1. For factor combinations for which more than one test was performed it can be seen that there was some degree of variability. Thus far no detailed examination of test-to-test variability has been performed, but possible sources for this variation might include small differences in explosive charge mass, in soil moisture content, as well as in the spatial configuration of the explosive in the soil and the height of the target above the top of the soil. An examination of the result averages reveals several trends. It was observed that, for the cases where the charge was located directly beneath the centers of the targets, the amount of peak momentum imparted to the flat target and the 13° concave target were relatively similar whereas the 21° concave target exhibited a moderately lower level. For these center

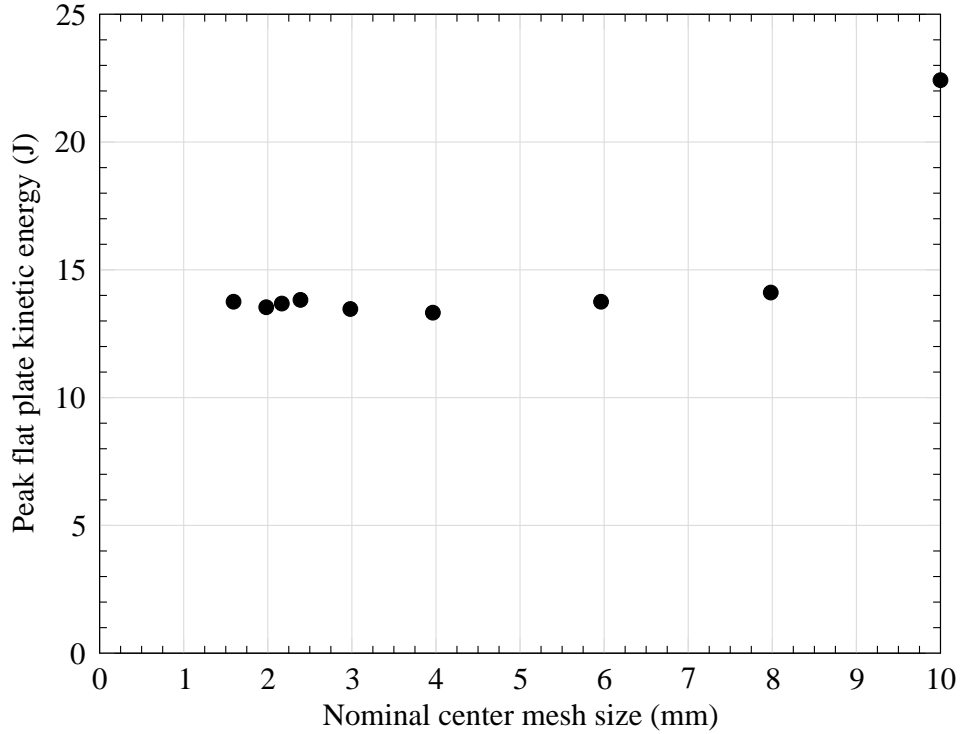


Figure 6.5: Results of the mesh convergence study. The nominally 2 mm mesh that was used for the computational work was in the converged region.

shots, the severity of the blast load was significantly reduced for both of the targets that were downwardly convex, with increased reduction for the 21° target.

The nominal depth of burial of the explosive and the stand-off distance between the targets and the upper surface of the soil bed was the same for all of the tests performed for this work. The target stand-off distance was taken to be the vertical distance from the sand surface to the nearest point on the target. For the downwardly convex targets, this point was at the lateral centerline of plate. For the downwardly concave targets, these points were at the outer edges of the plate. As a result, the distance between the surfaces of the angled plates and the charge was greater than it was between the flat plate and the charge.

Figure 6.6 shows experimental results from Fournery et al. (2010) for a flat plate excited by a 4.4g charge with a depth of burial of 5.34 mm in wet sand. It can be observed that

Table 6.1: Computational and experimental (Fourney et al., 2010) results for center and quarter shot excitation of target plates. Negative angle definitions indicate downwardly concave targets. Positive angle definitions indicate that targets were downwardly convex. For factor combinations for which more than one test was performed, individual test results are shown first and these are then followed by their average value.

Target bottom angle ($^{\circ}$)	Charge location	Experimental peak target momentum (N-s)	Computational peak target momentum (N-s)	Percentage difference
-21	Center	5.62, 6.42; mean 6.02	6.50	7.7
-13	Center	6.41, 6.96, 6.66; mean 6.68	6.69	0.2
0	Center	6.49, 6.78; mean 6.64	6.64	0 - used to calibrate model
13	Center	5.26	5.26	0.0
21	Center	4.84	4.38	-9.5
0	Quarter	8.35, 7.44; mean 7.90	7.18	-9.1
13	Quarter	6.94	6.26	-9.8
21	Quarter	5.74	5.36	-6.6

impulse decreases significantly with increasing stand off distance. It seems most likely that at least some of the observed reduction in the loading of the 21 degree downwardly concave, the 13 degree downwardly convex, and the 21 degree downwardly convex plates was a result of the increased distance between explosive and target. It is interesting to note that the downwardly convex targets, for the case of central loading, exhibited lower momentum than did the downwardly concave targets (Table 6.1).

In order to more carefully examine the mechanics of target loading as they relate to angled surfaces, a series of tests was conducted by Fourney et al. (2010) that involved the measurement of specific impulse at various locations on rigid downwardly convex targets as well as on rigid flat plates. For this work measurements were taken, using high speed digital video, of the impulse delivered to tapered, removable 25.4 mm diameter plugs. The mass of the plugs was varied, depending on the location on the rigid target, so that the velocity could be most accurately measured. Results from this work are shown in Figure

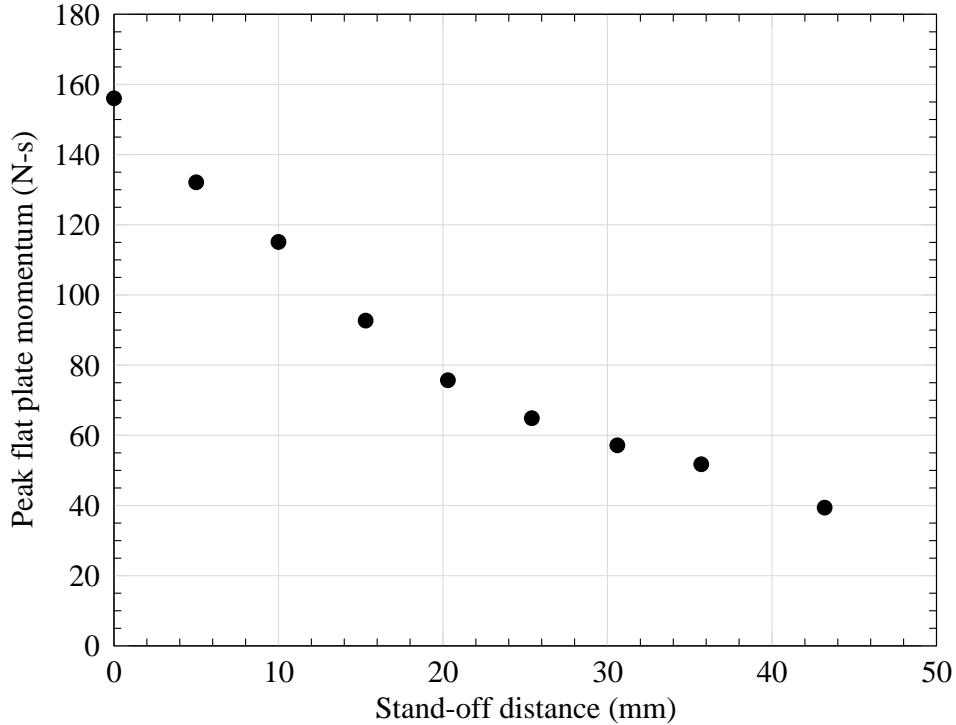


Figure 6.6: Impulse versus stand-off distance (SOD) for flat plate targets (from Fourney et al. (2010)). Charge size was 4.4 g and depth of burial was 5.34 mm. Impulse decreased exponentially with increasing distance between explosive and flat plate target.

6.7.

Referring to Figure 6.7, it is difficult, for distances greater than about 50 or 60 mm from the explosive, to distinguish between the response of the flat plate and the angled plate. However, as the distance between the explosive and the target decreased below this level there was some divergence between the results for the two cases. As the distance decreased, there appeared to be a trend toward higher excitation of the flat plate than of the angled target. On this basis it could be hypothesized that some portion of the reduction in excitation was a result of the effect of the geometric shape of the bottom of the target.

The performance of additional tests at smaller distances between charge and flat plate would help to clarify whether such an hypothesis is, in fact, correct. A comparison, taken from high speed video of some of the blast experiments, of the response of plates to excitation beneath their centerline and for quarter shots, i.e., for shots with charge located

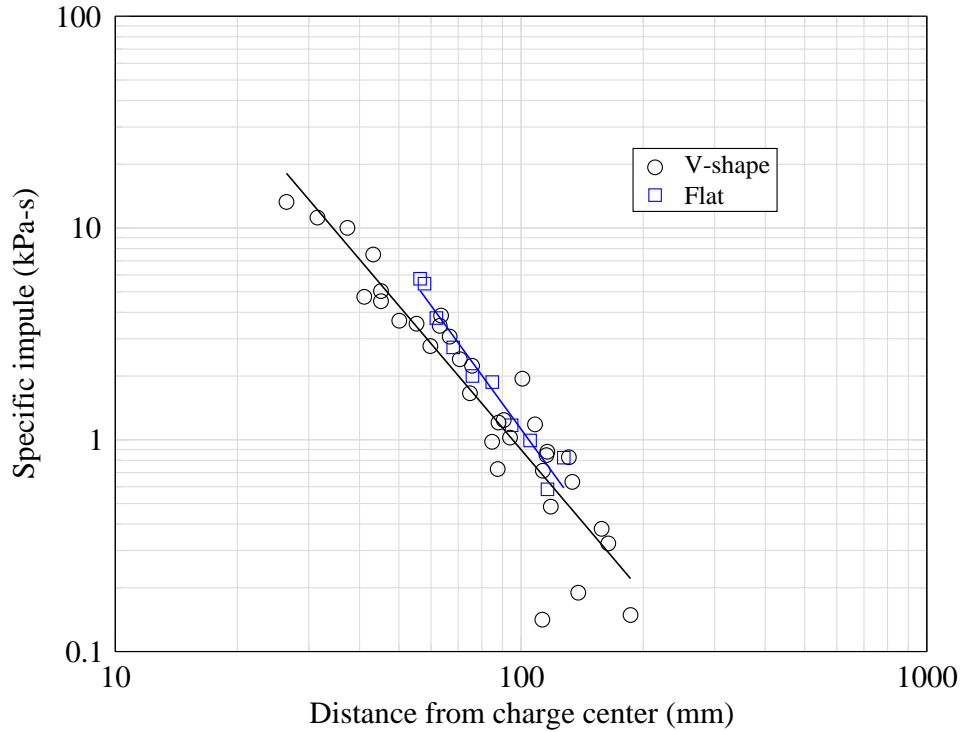


Figure 6.7: Specific Impulse versus radial distance from explosive charge center as measured by the momentum of tapered plugs located at various positions on flat and downwardly convex rigid aluminum targets (from Fourny et al. (2010)).

beneath a position halfway between the center and the outer lateral edge of the targets, can be seen in Figure 6.8. These images, from high speed video recordings of blast experiments performed by Fourny et al. (2010), were taken 20 milliseconds after explosive detonation.

6.5 Effect of offset loading

For the impacts that involved flat and downwardly convex plates (Table 6.1), the imparted momentum was higher for shots with the charge located halfway between the center and edge of the target than it was for the case of the centerline shots. This was a result of the combination two factors. First, a significant rotational component of the motion was caused by the offset location of the bottom surfaces of the targets relative to the progression of the blast front. This effect for the offset explosive location, developed from computational results, is shown in Figure 6.9.

Figure 6.9a shows the initial configuration of the flat plate as it rests upon its supports.

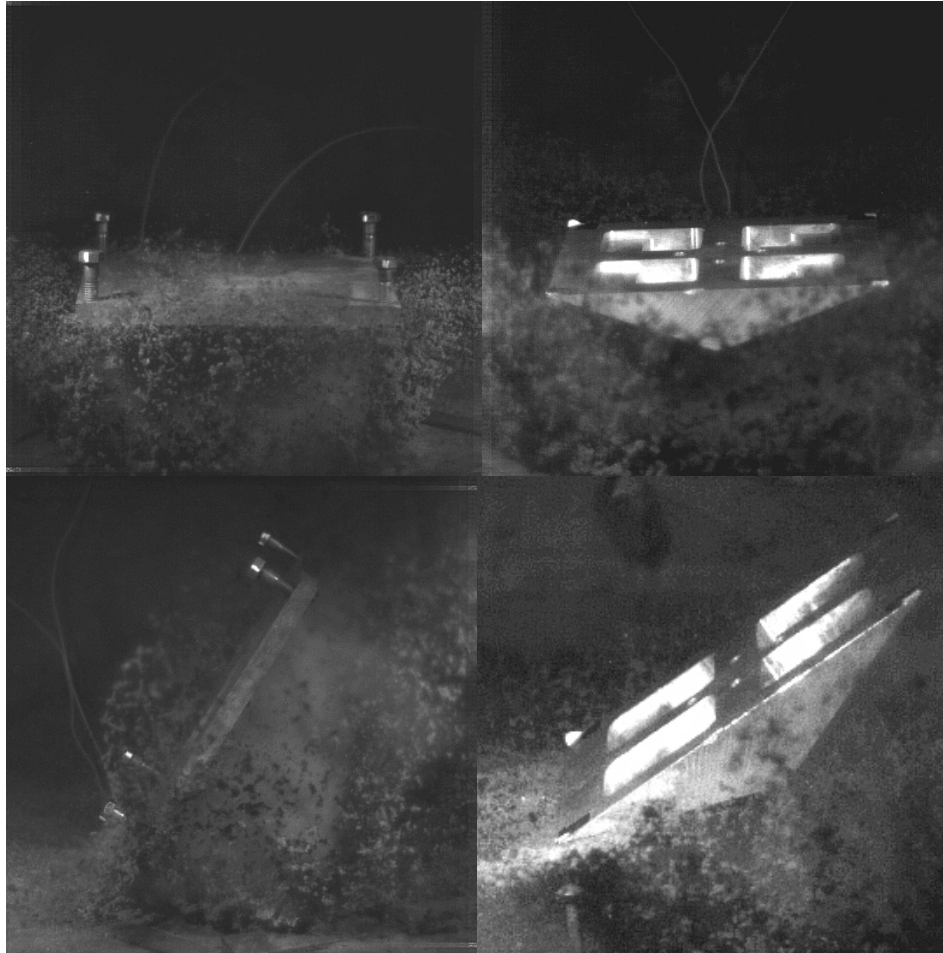
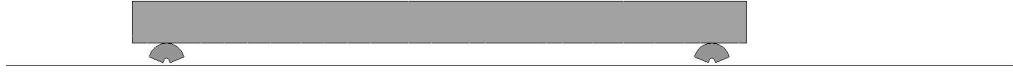


Figure 6.8: Conformation of flat (left), and 21° convex down (right) plates 20 milliseconds after charge detonation. Top row: targets that were excited by means of explosive buried beneath target centerline. Bottom row: targets that were excited by means of buried explosive charge located halfway between the centerline and outer lateral edge of target.

Figure 6.9b shows the conformation of the plate about 200 microseconds after the initiation of the detonation, at which point it is constrained on its left side by the support bolt but is rotating counter-clockwise and separating slightly on its right side from support bolt. Figure 6.9c shows the target 8 milliseconds after detonation, rotating counter-clockwise and completely separated from the bolt supports.

A hand calculation for impulsive loading of a very thin, rigid rod helped to clarify the fundamental reasons that the offset shots resulted in higher target translational momentum than did the center shots. If an impulse is defined as, say $[\delta(t) \text{ FC}]$ where $\delta(t)$ is the Dirac

a.



b.



c.

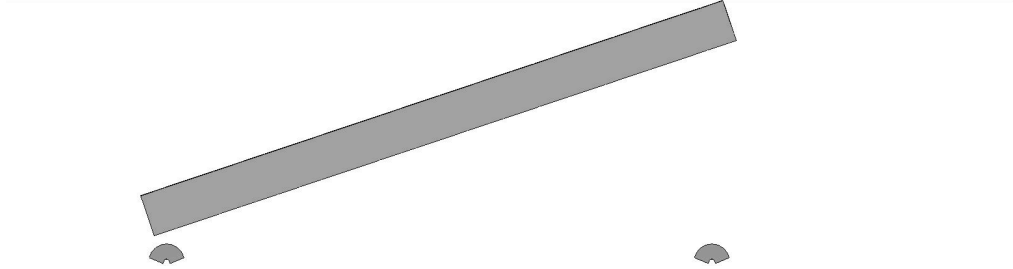


Figure 6.9: Effect, for quarter shot computations, of constraining bolt supports on target dynamics. a. Target in initial configuration. b. Target 200 microseconds after detonation, constrained on left side by support bolt but rotating and separating slightly on right side from support bolt. c. Target 8 milliseconds after detonation, rotating and separated from all bolt supports.

delta function and FC is the magnitude of the impulsive load then it can be shown, by integrating the relations for conservation of linear and angular momentum, that this impulse applied as quarter loading to the rod will impart 1.75 times the kinetic energy that it would impart if applied at the center of the rod. Therefore, even a somewhat lower impulsive load applied as a quarter shot could still impart more kinetic energy to a target than a somewhat higher impulsive load applied at the center of the target.

In addition, the initial constraint on the targets caused by the presence of the bolts used to position the targets above the top surface of the soil served to redirect a portion of the quarter shot rotational kinetic energy to the end that it was converted to translational kinetic energy thereby increasing the translational momentum of the targets' centers of

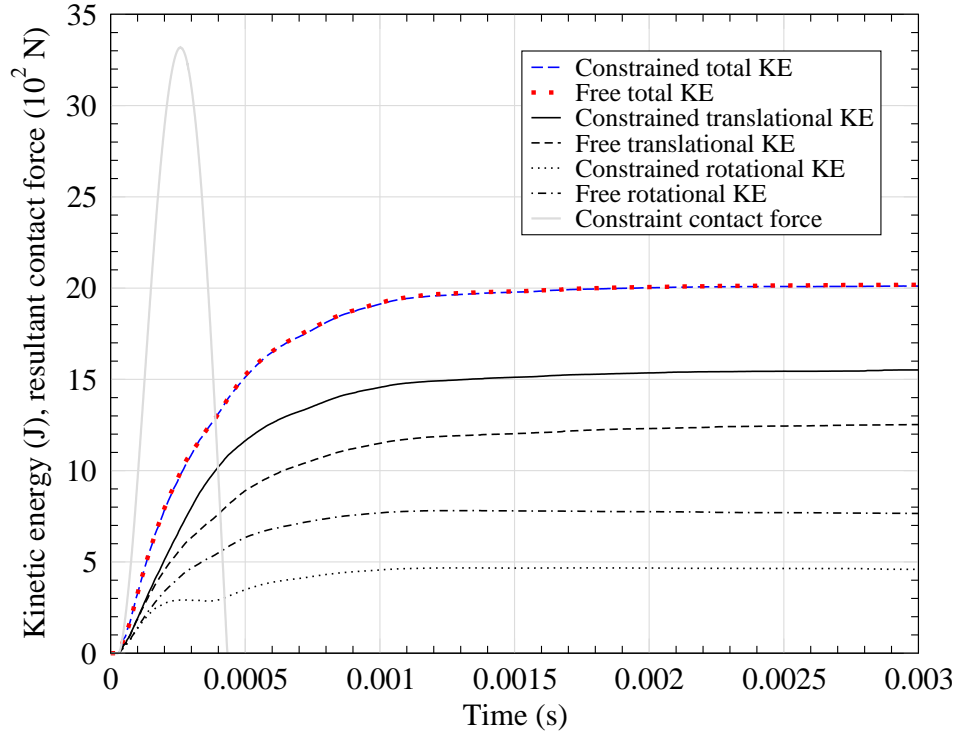


Figure 6.10: Computational kinetic energy results for flat plate rotation constrained by support bolts are compared with results for unconstrained flat plate. Support bolt constraint contact forces, for the constrained case, are superimposed.

mass. This point is illustrated in Figure 6.10, taken from a comparison of computational results for the flat plate with offset excitation but in one case constrained by the support bolts and, in another case floating free in space, that is, with no bolt constraints.

The total calculated kinetic energy for the target is almost the same for the constrained case as it is for the unconstrained case. However, it can be seen that the partitioning of rotational and translational energy is significantly different for the two cases. In the constrained case, the torque resulting from the contact forces between the target and the constraining bolts results in a significant reduction of target rotational inertia, and therefore rotational kinetic energy, which leads to a higher proportion of target translational kinetic energy - and translational momentum - than that which is observed for the unconstrained case. It is interesting to note the correspondence between the constrained case contact forces and the rotational kinetic energy of the target for the constrained case.

6.6 Computational results

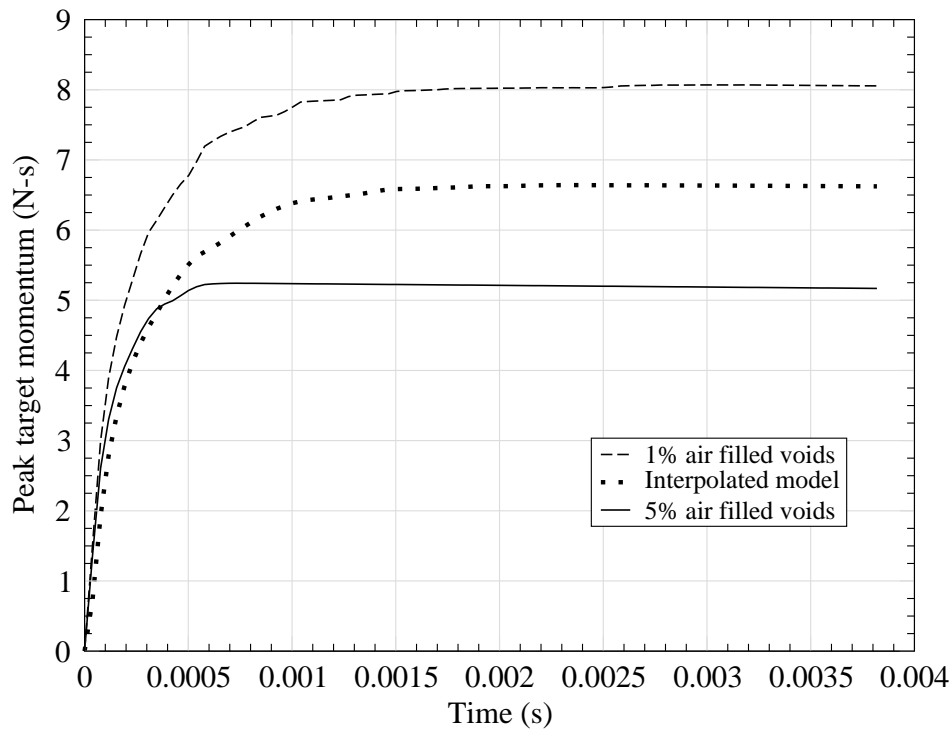


Figure 6.11: Computed target momentum - time histories generated using concrete sand models with 1 percent, 5 percent, and an interpolated, intermediate, level of air filled voids for the case of the flat plate with explosive charge buried directly beneath the lateral centerline of the plate.

Constitutive models associated with the SABER ground shock solver (Zimmerman et al., 1993; Akers et al., 1995) were used for performing calculations involving 1 percent air filled void and 5 percent air filled void poorly graded wet concrete sand. Computations performed using models for these two soils for the case of the flat plate and centerline location of the explosive produced target peak momentum of 8.07 N-s and 5.24 N-s, respectively. One of the primary aims of this study was to examine the use of a computational method that would be based very much on the physics of the problem and that would involve a minimal amount of tuning of model parameters.

However, no constitutive models were immediately available for concrete sand emplacement conditions with air filled void contents between 1 and 5 percent. As a result, an

iterative process, based on the physical behavior of the soil and discussed previously in section 4.3.2, was used to develop interpolated values for the various components of the soil model to the end that the computational model produced a peak target momentum that matched the experimental peak level of 6.64 N-s. Computed target momentum - time histories generated using concrete sand models with 1 percent, 5 percent, and the calibrated intermediate level of air filled voids are presented in Figure 6.11.

High speed video was used by Genson (2006) in order to investigate the evolution, for time increments of 40 microseconds, of the blast for the case of a 0.636 g explosive charge, wet sand, 4.826 mm depth of charge burial but with no target, in other words, under the same conditions of soil and explosive that were used in the present study for aluminum target excitation. Computations, using the ALE method described above, were performed for this same set of parameters. A comparison of these results is given in Figure 6.12.

All frames in the figure are shown at the same scale. In the figure, the soil was represented by the light gray colored continuum while the reaction products from the detonation of the explosive were represented by the black region. As a result of the relatively low volume fraction of sand in the dust cloud and the computational mesh size in comparison to the scale of the sand particles, it was not possible to capture, for the case of the computations, the fine detail of the dust that comprised the cloud of ejecta.

During the course of computations performed on the downwardly convex target plates for center shot charge location, convergence problems emerged for the case of the 250 mm computational domain radius. A physically unrealistic continuous increase in target momentum was observed in the plate response to the blast load. This was caused by the emergence of numerical instabilities at the ALE computational domain boundaries. A convergence study that involved several iterations with expansion of the outer radius of the cylindrical ALE computational domain beyond its initial value of 246.3 mm supported this hypothesis. Based on the results of the convergence study, the computational domain size was ultimately expanded to a radius of 480 mm.

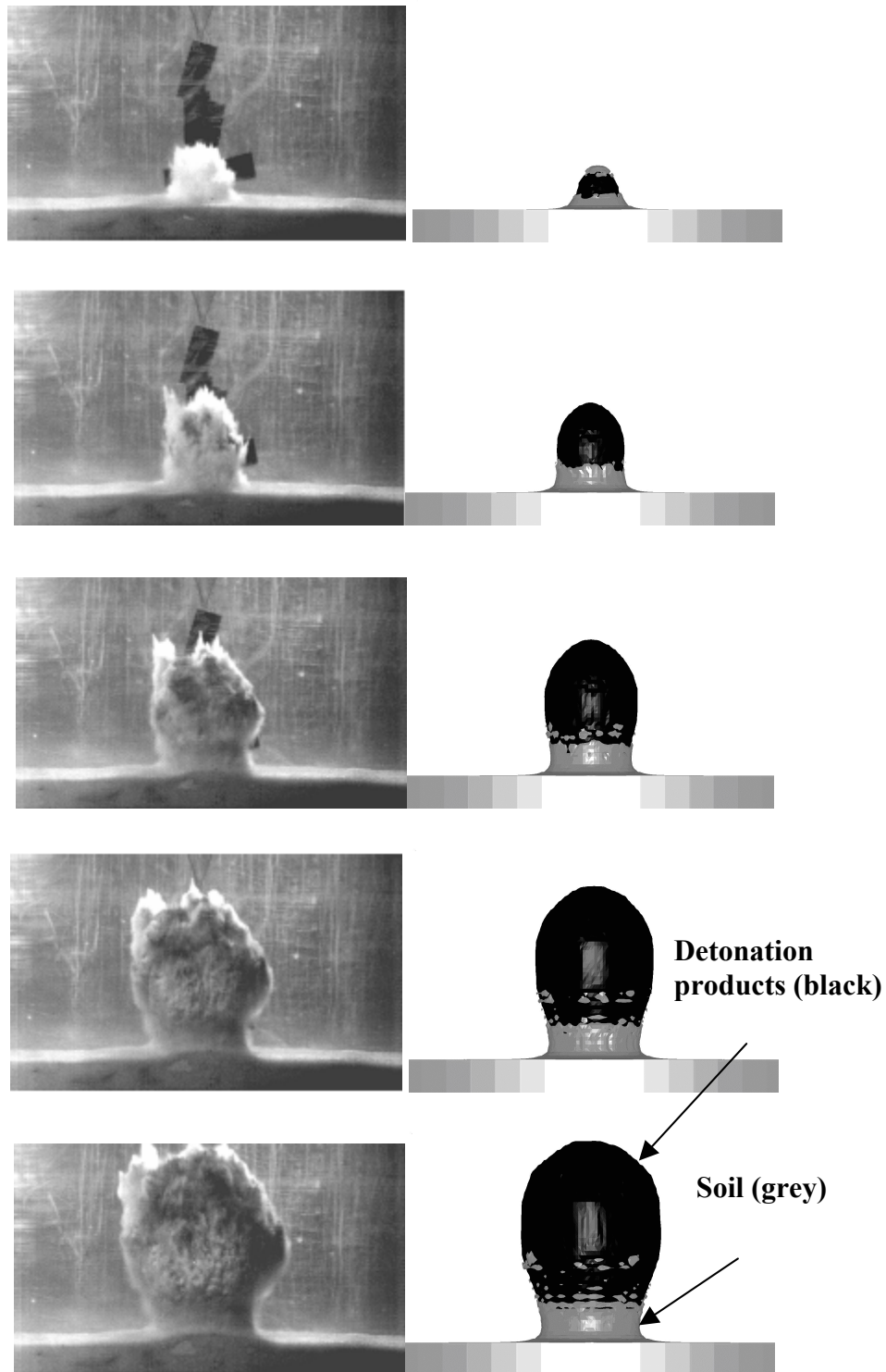


Figure 6.12: 40 μs per frame comparison of experimental results (from Genson (2006)), with computational results. In the animation illustrations, the grey material is the wet sand; the black material is the detonation reaction product gases.

Computations were performed first for center shots on all target configurations. A primary objective of the computational work was to determine whether it would be possible to match the experimental results for the rigid plates by using ALE computations and the soil model described above, a soil model that was based purely on quasi-static determination of the soil behavior. The results from these computations are compared with the experimental findings in Table 6.1.

Percentage difference was calculated based on the deviation of computational results from experimental results. The case of the flat plate, center charge location was used to interpolate the soil model. Thus, for that particular case, the calculation of percentage difference was not relevant.

It can be seen that, for the remaining cases, the agreement between computation and experiment was reasonable. Computations were also performed for some of the cases that involved explosive buried halfway between the center and the outside lateral edge of these targets. The agreement with the experimental results was found to be, for these cases, also very good.

Chapter 7

Conclusions and future research recommendations

7.1 Conclusions

The two phase fluid model developed for this work and applied to the Couette flow of a fluidized bed very closely matched experimental data. Although it was a relatively simple model, it yielded accurate results. It could possibly, in the future, be applied toward examination of a secondary blast effect, namely, the flow of soil that has been ejected, via erosion, from the surfaces of craters.

The application of soil mechanics principles and effective stress theory to computations involving shallow buried explosives in water, dry sand, and unsaturated sand yielded close agreement with small scale experiments as well as some insight into the mechanisms behind target loading from such events.

Materials with yield surfaces that had lower yield strengths demonstrated a greater propensity toward flow and toward higher target momentum loading. This was, when comparing effects due to dry sand, wet sand, and water the most significant factor. Water, being a fluid, had no strength and produced the highest target loading. Dry sand had the highest strength at any given pressure and produced the lowest target loading. The strength and target loading for the case of unsaturated sand were intermediate between those observed with the other two materials.

Other, but less important factors, for the comparison of responses due to water, wet sand, and dry sand, were those associated with bulk compressibility and initial bulk density. It was observed that lower volumetric stiffness yielded somewhat lower target loading and that higher initial density yielded moderately higher target loading.

Next, investigations were performed using beds comprised of water as well as beds comprised of each of three soil types - poorly graded sand, silty sand, and clayey sand - using various combinations of initial water content and compaction. It was demonstrated that,

in both the experiments and in the computations, that there is a significant relationship between initial air filled voids volume fraction and the momentum applied to a rigid target plate by an explosion in a bed filled with soil or with water, and that the the momentum imparted to the target decreases with increasing initial air filled void content. Not all computations converged to a single curve, but leading order effects were captured.

Computations were used, based on experimentally obtained constitutive models for the behavior of the soils, to determine and compare the sensitivity of the target momentum to soil yield behavior, to compressive soil hydrostatic behavior, and to initial soil bulk density. It was shown, using computations, that the momentum imparted to the target increases with decreasing yield strength as a result of the propensity of the lower levels of yield strength to increase the rate of flow of the soil out of the soil bed and toward the rigid target.

It was shown, by comparing experimentally determined constitutive behavior for soils with varying levels of water content, that there is a relation between soil initial water content and the mean yield strength whereby the yield strength decreases with increasing water content. It was also shown, via computations, that there was significant sensitivity to the lock-up point of the hydrostat which is directly related to the initial air filled void volume fraction of a soil. The lock-up point is the point at the level of compressive strain at which the air filled void content of the soil becomes vanishingly small and at which the bulk modulus makes a significant jump.

The target momentum increased as the saturation or lock-up point moved toward decreasing levels of strain due to the tendency of the reduction in compliance to force more soil outward from the soil bed and upward toward the rigid target. Finally, it was observed, using a series of computations, that there was somewhat less sensitivity of target momentum to the initial bulk density of the soil.

The response of downwardly convex, flat, and downwardly concave rigid targets to excitation from shallow buried explosives located at various locations beneath the targets

was examined using an approach that involved experimental, computational, and analytical methods. High speed video techniques were used to observe blast phenomena and measure the dynamics of the target plates. It was observed experimentally that rigid targets - with bottom geometries that were downwardly convex and with bottom geometries that were downwardly concave - reduced the amount of momentum imparted to the target by the explosive detonation products and the soil.

Also, it was observed that the rotational effects imparted to flat and downwardly convex targets with explosive buried in non-centerline locations were significant. The computations that were performed were found to agree very closely with experimental results. This work served to reinforce the hypothesis that a computational soil model, based purely on quasi-static test evaluations, could enable close agreement between experiment and computational results for peak target momentum.

7.2 Recommendations for future research

Several areas for future research are indicated by the findings from the current work.

- The two phase fluidized bed model developed for this work has some potential for application to the flow of soil removed, by erosion, from crater boundaries. Before it is assumed, however, that this model accurately predicts more general two phase flow phenomena, the model should be modified in order to be able to treat two or three dimensional problems and then more completely evaluated using the experimental crater evolution results available from, say, Bergeron et al. (1998) or Foedinger and Caiazzo (2006).

- New aspects of the mechanics of momentum transfer from explosive charges buried in water, sand, clayey sand, and silty sand to rigid structures were discovered and examined. There are still significant opportunities for investigation of these types of effects when the explosive is buried in more cohesive soils consisting primarily of clay.

- The deviatoric yield behavior used in these investigations was treated as being plastic, and was defined as being dependent only on the the first and second stress invariants. It might prove to be worthwhile to use similar methodology in order to more carefully examine

the dependence of momentum transfer on viscous effects and, also, whether it would be useful to define yield behavior in terms of all three stress invariants.

- This work involved measurement and definition of the effects on structures in terms of the total momentum transferred to them, that is on the temporal-spatial integral of momentum transferred to the structures. There is still a need for a more detailed examination, in time and space, of the nature of the momentum field created by the soil and buried explosive.

- The effects of buried charges were, in this work, examined in terms of loading on rigid structures. Many relevant structures are not rigid but are deformable. Therefore the effects of buried explosives on deformable structures ought also to be investigated.

- Finally, further research ought to be undertaken in order to more fully understand the physics associated with the placement of buried explosive charges in positions that are laterally off-center relative to structures.

REFERENCES

1. Akers, S.A., and Stelter, J., 1991, SABER-PC: A Ground Shock Software Package for the PC, in: Proceedings, 5th International Symposium on Interaction of Effects of Munitions with Structures, Mannheim, Germany.
2. Akers, S. A., Adley, M. D., and Cargile, J. D., 1995, Comparison of constitutive models for geologic materials used in penetration and ground shock calculations, in: Proceedings, 7th International Symposium on Interaction of Effects of Munitions with Structures, Mannheim, Germany.
3. Anderson, T.B., and Jackson, R., 1967, A fluid mechanical description of fluidized beds, *I&EC Fundam.*, **6**(4), 527-539.
4. Anderson, C.E., Behner, T., Weiss, C.E., Chocron, S., and Bigger, R.P., 2010, Mine blast loading: Experiments and Simulations, Southwest Research Institute Report 18.12544/011, San Antonio, TX.
5. Anderson, C.E., Behner, T., Weiss, C.E., 2011, Mine blast loading experiments, *Int. J. Impact Eng.*, **38**(8-9), 697-706.
6. Anjaneyulu, P., and Khakhar, D.V., 1995, Rheology of a gas-fluidized bed, *Powder Technology*, **83** (1), 29-34.
7. Artyunov, O.A., Grigoryan, S.S, and Kamalyan, R.Z, 1985, Effect of soil moisture content on parameters of crater cuts, *Combust. Explos. Shock Waves (USSR)*, **21**(2), 259-262.
8. Baker, W.E., 1972, *Explosions in Air*, University of Texas Press, Austin, TX.
9. Benson, D.J., 2010, Introduction to Arbitrary Lagrangian-Eulerian in Finite Element Methods, in: Souli, M. and Benson, D.J, editors., *Arbitrary Lagrangian-Eulerian and Fluid-Structure Interaction*, Wiley, Hoboken, NJ, pp. 1-50.
10. Bergeron, D., Walker, R., and Coffey, C., 1998, Detonation of 100-Gram Anti-

Personnel Mine Surrogate Charges in Sand, Suffield Report No. 668, Defence Research Establishment Suffield, Ralston, AB, Canada.

11. Bouillard, J. X., Lyczkowski, R. W. and Gidaspow, D., 1989, Porosity distributions in a fluidized bed with an immersed obstacle, *AIChE Journal*, **35**(6), 908-922.

12. Braid, M.P., 2001, Experimental investigation and analysis of the effects of anti-personnel land mine blasts, Master of Engineering Thesis, Royal Military College of Canada, Kingston, ON.

13. Carnahan, B., Luther, H.A., and Wilkes, J.O., 1969, *Applied Numerical Methods*, Wiley, New York, pp. 573-574.

14. Cherry, J.T., 1967, Computer calculations of explosion-produced craters, *Int. J. Rock Mech. Min. Sci.* **4**(1), pp. 1-12.

15. Cho, G.C., Dodds, J., and Santamarina, J.C., 2006, Shape effects on packing density, stiffness, and strength: Natural and crushed sands, *J. Geotech. Geoenviron. Engrg.*, **132** (5), 591-602.

16. Cole, R.H., 1965, *Underwater Explosions*, Dover, New York.

17. Cooper, P.W., 1997, Introduction to Detonation Physics, in: *Explosive Effects and Applications*, ed. J.A. Zukas and W.P. Walters, Springer, New York, pp. 115-135.

18. Laboratory soils testing, 1980, Engineering Manual EM-1110-2-1906, U.S. Army Corps of Engineers, Washington DC, 1980.

19. Danielson, K.T., Akers, S.A., O'Daniel, J.L., Adley, M.D., and Garner, S.B., 2008, Large-Scale Parallel Computation Methodologies for Highly Nonlinear Concrete and Soil Applications, *ASCE Journal of Computing in Civil Engineering*, **22**(2), pp. 140-146.

20. Dartevelle, S., 2004, Numerical modeling of geophysical granular flows 1, A comprehensive approach to granular rheologies and geophysical multiphase flows, *Geochem. Geophys. Geosyst.*, **5**(8).

21. Deshpande, V.S., McMeeking, R.M., Wadley, H.N.G. , and Evans, A.G., 2009, Constitutive model for predicting dynamic interactions between soil ejecta and structural panels, *J. Mech. Phys. Solids* **57**(8) 1139-1164.
22. DiMaggio, F.L. and Sandler, I.S., 1971 Material model for granular soils, *J. Eng. Mech. Div-A.S.C.E.*, **97**(3), 935-950.
23. B.M. Dobratz, B.M, 1981 LLNL Handbook of Explosives, UCRL-52997, Lawrence Livermore National Laboratory, Livermore, CA.
24. Drake, J.L., and Little, C.D., 1983, Ground shock from penetrating conventional weapons, in: *Proceedings of the Symposium on the Interaction of Non-nuclear Weapons with Structures*, Colorado Springs, CO, pp 1-6.
25. Drucker, D.C., and Prager, W., 1952, Soil mechanics and plastic analysis for limit design, *Quart. Appl. Math.*, **10**(2), 157165.
26. Enwald, H., Peirano, E., and Almstedt, A.E., 1996, Eulerian two-phase flow theory applied to fluidization, *Int. J. Multiphase Flow*, **22**, Supplement, 21-66.
27. Ehr Gott, J.Q., Akers, S.A., Windham, J.E., Rickman, D.D., and Danielson, K.T., 2011, The influence of soil parameters on the impulse and airblast overpressure loading above surface-laid and shallow-buried explosives, *Shock Vib.*, **18**(6), 857-874.
28. Ehr Gott, J.Q., 2011, Influence of Soil Properties on the Aboveground Blast Environment from a Near-Surface Detonation, ERDC/GSL Technical Report TR-11-28, U.S. Army Engineer Research and Development Center, Vicksburg, MS.
29. Ehr Gott, J.Q., U.S. Army Engineer Research and Development Center, Vicksburg, MS, Personal communication.
30. The Unified Soil Classification System, 1960 Technical Memorandum No. 3-357, US Army Engineer Waterways Experiment Station, Vicksburg, MS.
31. Foedinger R., and Caiazzo, A., 2006, Methodology for improved characterization of land mine explosions, Technical Progress Report 6062/CC02, Materials Sciences Corporation, Horsham, PA.

32. Fourney, W.L., Taylor, L.C., and Robeson, D., 1999, Underwater cratering and channeling with explosives, *Fragblast*, **3**(2), 165-183.
33. Fourney, W.L., Leiste, U., Bonenberger, R., and Goodings, D., 2005, Explosive impact on plates, *Fragblast*, **9**(1), 1-17.
34. Fourney, W.L., Leiste, U., Hauch, A., and Jung, D., 2010, Distribution of Specific Impulse on Vehicles Subjected to Improvised Explosive Devices, *Blasting and Fragmentation Journal*, **4**(2), 117-135.
35. Fourney, W.L., Personal communication.
36. Fourney, W.L., Leiste, U., and Fox, D.M., 2013, The effect of air filled voids on impulse delivered by a buried mine, *Blasting and Fragmentation Journal*, **7**(1), 31ff.
37. Fox, D.M. and Lee, J.S., 2011, Application of an Arbitrary Lagrangian Eulerian Method to Describe High Velocity Gas-Particle Flow Behavior, in: *Proceedings, ASME-JSME-KSME 2011 Joint Fluids Engineering Conference*, Hamamatsu, Japan, pp. 1507-1514.
38. Friedman, B., 1950, Theory of underwater explosion bubbles, *Commun. Pure Appl. Math.*, **3**(2), 177-199.
39. Fulmer C.V., 1965, Cratering characteristics of wet and dry sand, Technical Report D2-90683-1, The Boeing Company, Seattle, WA.
40. Gear, C.W., *Applications and Algorithms in Science and Engineering*, Science Research Associates, Chicago, 1978.
41. Genson, K.W., 2006, Vehicle shaping for mine blast damage reduction, M.S. Thesis, University of Maryland, College Park, MD.
42. Gidaspow, D. and Ettehadieh, B., 1983, Fluidization in two-dimensional beds with a jet: 2 Hydrodynamic modelling, I & EC Fundam, **22**(2), 193-201.
43. Gidaspow, D. and Syamlal, M., 10-15 November, 1985, Solid-gas critical flow, AIChE Meeting, Chicago.

44. Goodrich, M.F., Bryan, J.B., Thomsen, J.M., and Snell, C.M., 1976 Final report on a calculational parameter study of soils typical of some Essex I cratering sites, UCRL-52038, Lawrence Livermore National Laboratory, Livermore, CA.
45. Gupta, A.D., 2001, Modeling and analysis of a 3-D asymmetric mine-soil-hull-floor interaction problem with mine buried in dry and wet sand, Report No. ARL-RP-29 US Army Research Laboratory, Aberdeen Proving Ground, MD.
46. Hallquist, J.O., 2006, LS-DYNA Theoretical Manual, Livermore Software Technology Corporation, Livermore, CA.
47. Henrych, J., 1979, The Dynamics of Explosion and Its Use, Elsevier, New York.
48. Hlady, S.L., 2004 Effect of soil parameters on landmine blast, 18th Military Aspects of Blast and Shock Conference, Mannheim, Germany.
49. Ishii, M., and Hibiki, T., 2006, Thermo-Fluid Dynamics of Two-Phase Flow, Springer, New York.
50. Jackson, Jr., J.G., 1969, Analysis of laboratory test data to derive soil constitutive properties, U.S. Army Engineer Waterways Experiment Station Miscellaneous Paper S-69-16, Vicksburg, MS.
51. Johansson, K., van Wachem, B.G.M., Almstedt, A.E., 2006, Experimental validation of CFD models for fluidized beds: Influence of particle stress models, gas phase compressibility and air inflow models, Chem. Eng. Sci, **61**(5), 1705-1717.
52. Kerley, G.I., 1999, Equations of State for Composite Materials, Kerley Publishing Services Report KPS99-4, Albuquerque, NM.
53. Kerley, G.I., 2001, Numerical Modeling of Buried Mine Explosions, Technical Report ARL-CR-461, US Army Research Laboratory, Aberdeen Proving Ground, MD.
54. Kerley, G.I., 2002, The Effects of Soil Type on Numerical Simulations of Buried Mine Explosions, Technical Report KTS02-3, Kerley Technical Services, Appomattox, VA.

55. Kerley, G.I., 2005, On the Numerical Simulation of Buried Mine Explosions: Choosing Constitutive Models, Technical Report KTS05-3, Kerley Technical Services, Appomattox, VA.
56. Kingery, C.N. and Bulmash, G., 1984, Airblast Parameters from TNT Spherical Air Burst and Hemispherical Surface Burst, Technical Report ARBRL-TR-02555, US Army Ballistic Research Laboratory, Aberdeen Proving Ground, MD.
57. Kolsky, H., Lewis, J.P., Sampson, M.T., Shearman, A.C., and Snow, C.I., 1949, Splashes from underwater explosions, *Philos. Trans. R. Soc. London, Ser. A*, **196**(1046), pp. 397-402.
58. Laine, L., and Sandvik, A., 2001, Derivation of Mechanical Properties for Sand, 4th Asia-Pacific Conference on Shock and Impact Loads on Structures, CI-Premier PTE Ltd., Singapore, pp. 361-368.
59. Laine, L., Ranestad, O. Sandvik, A., and Snekkevik, A., 2002, Numerical Simulation of Antitank Mine Detonations, in: M.D. Furnish, N.N. Thadhani, and Y. Horie, Eds., *Shock Compression of Condensed Matter*, Conf. Proc. 620, American Institute of Physics, College Park, MD, pp. 431-434.
60. Lambe, T.W. and Whitman, R.V., 1969, *Soil Mechanics*, Wiley, New York.
61. Lampson, C.W., 1946, Final report on effects of underground explosions, NDRC Report No. A-479, OSRD Report No. 6645, Washington, DC.
62. Lottero, R.E., and Kimsey, K.D., 1978, A comparison of computed versus experimental loading and response of a flat plate subjected to mine blast, Memorandum Report ARBRL-MR-02807, US Army Ballistics Research Laboratory, Aberdeen Proving Ground, MD.
63. Livermore Software Technology Corporation, 2012, LS-Dyna keyword user's manual, Volumes I and II, Livermore, CA.
64. Lyakhov, G.M., 1964, *Principles of Explosion Dynamics in Soils and in Liquid Media*, Nedra, Moscow.

65. Maenchen, G., and Sack, S., 1963, The TENSOR code, Report No. UCRL-7316, Lawrence Radiation Laboratory, Livermore, CA.
66. C.I. Malme, C.I., Carbonell, J.R., and Dyer, I., 1966 Mechanisms in the generation of airblasts by underwater explosions, Naval Ordnance Laboratory Technical Report 66-88, White Oak, MD.
67. McCabe W.E., Smith J.C., and Harriott P., 2001, Unit Operations of Chemical Engineering, McGraw Hill, New York.
68. McGlaun, J.M., Thompson, S.L., and Elrick, M.G., 1990, CTH: A Three-Dimensional Shock Wave Physics Code, *Int. J. Impact Eng.*, **10**(1-4), pp. 251-360.
69. Montgomery, D.C., 1991 Design and Analysis of Experiments, 3rd Ed., Wiley, New York.
70. Moxnes, J.F., Odegardstuen, G., Atwood, A., and Curran, P., 1999, Mechanical Properties of a Porous Material Studied in a High Speed Piston Driven Compaction Experiment, 30th International International Conference of the Fraunhofer Institute for Chemical Technology, Karlsruhe, Federal Republic of Germany.
71. Nelson, I. and Baron, M.L., 1971, Application of variable moduli models to soil behavior, *Int. J. Solids Structures*, **7**(4) 399-417.
72. Neuberger A, Peles S, and Rittel D., 2007, Scaling the response of circular plates subjected to large and close-range spherical explosions. Part II: buried charges, *Int. J. Impact Eng.*, **34**(5), 874-882.
73. Nordyke, M.D., 1961, Nuclear Craters and Preliminary Theory of the Mechanics of Explosive Crater Formation, *J. Geophys. Res.*, **66**(10), 3439-3459.
74. Oberkampf, W.L. and C.J. Roy, C.J., 2010, Verification and Validation in Scientific Computing, Cambridge University Press, Cambridge, pp. 489-516.
75. Olowson, P.A. and Almstedt, A.E., 1991, Influence of pressure on the minimum fluidization velocity, *Chemical Engineering Science*, **46**(2), 637-640.

76. Perkins, B., 1954, True crater dimensions in various soils and rock, Ballistic Research Laboratories Memorandum Report No. 773, Aberdeen Proving Ground, MD.
77. Rohani, B., 1977, Mechanical constitutive models for engineering materials, U.S. Army Engineer Waterways Experiment Station Miscellaneous Paper S-77-19, Vicksburg, MS.
78. Rowe, P.N., 1961, Drag forces in a hydraulic model of a fluidized bed, part II, Transactions of the Institution of Chemical Engineers, **39**, 175-180.
79. Steinberg, D.J., 1987, Spherical explosions and the equation of state of water, UCID-20974, Livermore, CA.
80. Stiglitz, J., and Bilmes, L., 2008, The Three Trillion Dollar War: The True Cost of the Iraq Conflict, W.W. Norton, New York.
81. Szymczak, W.G. and Rogers, J.C.W., 2000, Generalized Hydrodynamics With Viscoplasticity for Channeling in Saturated Sand, Report No. NRL/FR/7130-00-9946, Naval Research Laboratory, Washington, DC.
82. Szymczak, W.G., 2005, Platform loading from explosions in saturated sand using a visco-plastic model, Fragblast, **9**(4), 189-203.
83. Taylor, L.C., Skaggs, R.R., and Gault, W., 2005, Vertical impulse measurements of mines buried in saturated sand, Fragblast, **9**(1), 19-28.
84. Terhune, R.W., Stubbs, T.F., and Cherry, J.T., 1970, Nuclear cratering on a digital computer, UCRL-50898, Livermore, CA.
85. Tillotson, J.H., 1962, Metallic equations of state for hypervelocity impact, GA-3216, General Atomic, San Diego, CA.
86. United States Department of Defense Office of the Assistant Secretary of Defense for Special Operations / Low Intensity Conflict, 2000, Landmine Casualty Data Report: Deminer Injuries, Washington, D.C.

87. United States Department of Defense Manpower Data Center, 2008, Global War on Terrorism Casualties by Reason - October 7, 2001 Through August 2, 2008, Washington, D.C.
88. van Wachem, B.G.M., Schouten, J.C., van den Bleek, C.M., and Sinclair, J.L., 2001, Comparative analysis of CFD models of dense gas-solid systems, *A.I.Ch.E. Journal*, **47**(5), 1035-1051.
89. Wagner, M.H., Zimmerman, H.D., Cooper, G.C., Simonian, S.E., and Ito, Y.M., 1986, Influence of Material Models on Ground Shock Environments: Report 1, Three Invariant H-E-P Model with Separate Reloading, Technical Report SL-86-47, California Research and Technology, Inc., Chatsworth, CA.
90. Wang, J., 2001, Benchmark Work of Simulation of Explosion in Soil and Air, Report No. DSTO-TR-1168, Defence Science & Technology Organisation, Fishermans Bend, Vic, Australia.
91. Wardlaw, A.B., Luton, J.A., Renzi, J.R., Kiddy, K.C., McKeown, R.M., 2003 The Gemini Euler solver for the simulation of underwater explosions, Naval Surface Warfare Center, Indian Head Technical Report 2500, Indian Head, MD.
92. Wen, C.Y. and Yu, Y.H., 1966, Mechanics of fluidization, *Chemical Engineering Progress Symposium Series* 62, 100-111.
93. Wenzel, A.B., and Esparza, E.D., 1972 Measurement of pressures and impulses at close distance from explosive charges buried and in air, U.S. Army Mobility Equipment Research and Development Center, Fort Belvoir, VA.
94. Wenzel, A.B., and Esparza, E.D., 1974, The response of armor plates to landmines using model experiments, U.S. Army Tank Automotive Command, Warren, MI.
95. Westine, P.S., 1972 The impulse imparted to targets by the detonation of land mines, *The Shock and Vibration Bulletin*, Bulletin 42, Part 4, pp. 97-107 Naval Research Center, Washington, DC.

96. Westine, P.S., Morris, B.L., Cox, P.A., and Polch, E.Z. , 1985, Development of a Computer Program for Floor Plate Response from Land Mine Explosions, Contract Report no. 13045, U.S. Army TACOM Research and Development Center, Warren, MI.
97. Whitmen, R.V., 1964, Mechanical properties of soil, In: Sauer, F.M., Nuclear Geoplosics, Part II, Stanford Research Institute, Menlo Park, CA pp 1-110.
98. Williams, K., and McLennan, S., 2003, A numerical analysis of mine blast effects on simplified target geometries, DRDC Valcartier Technical Memorandum No. 2002-260, Defence R&D Canada - Valcartier, Quebec, QC.
99. Williams, E.M., Windham, J.E., Ehrgott, J.Q., Danielson, K.T., and Gorsich, T.J., 2008 Effect of Soil Properties on an Above Ground Blast Environment from Buried Bare Charges, 20th Military Aspects of Blast and Shock Symposium, Oslo, Norway.
100. Windham, J.E., U.S. Army Engineer Research and Development Center, Vicksburg, MS, Personal communication.
101. Zakrisson, B. Wikman, B., and Johansson, B., 2008, Half scale experiments with rig for measuring structural deformation and impulse transfer from land mines, in: Bless, S., Walker, J., Eds., Proc. 24th Int. Symp. Ballistics, DEStech Publications, Inc., Lancaster, PA, pp. 497-504.
102. Zhao, Y., Wei, L., 2000, Rheology of gas-solid fluidized bed, Fuel Processing Technology, **68**(2), 153-160.
103. Zimmerman, H.D., Shimano, R.T., and Ito, Y.M., 1992, Early time ground shock from buried conventional explosives: users guide for SABER-PC/CWE, Report SL-92-1, California Research & Technology Division, Titan Corporation, Chatsworth, CA.
104. Zimmerman, H.D., Ito, Y.M., and Carney, J.A., 1993 Effective Stress Constitutive Models for Saturated and Partially Saturated Soils in: Proceedings of the Sixth

International Symposium on Interaction of Nonnuclear Munitions with Structures,
Panama City Beach, FL, pp. 294-299.

ABSTRACT**THE MECHANICS OF MOMENTUM TRANSFER FROM
EXPLOSIVE CHARGES BURIED IN WATER, IN SAND,
AND IN SAND WITH FINES**

by

DAVID M. FOX

August 2014

Advisor: Dr. Trilochan Singh

Co-Advisor: Dr. Joon Sang Lee

Major: Mechanical Engineering

Degree: Doctor of Philosophy

Physical tests involving full-scale systems subjected to blast loads are expensive. The development of more accurate computational and analytical methods to better understand and predict the mechanics of mine blast phenomena could be used to reduce the cost of development of mine protected vehicles and protective equipment for personnel involved in demining and similar activities.

Although the science associated with air blast and blast-related ground shock phenomena is very extensive, that of mine blast, involving explosives buried in soil, is less well developed. In this work, theoretical, experimental, and computational methods are synthesized to better understand some of the mechanisms that affect the way that an explosive charge, buried in a bed containing soil or water, might affect a structure located above and in proximity to the surface of the bed.

For some loading regimes, the flow of soil as it is ejected from the surface of a blast crater is important. This work first examines the behavior of a bed containing sand-like particles suspended in air by virtue of the flow of the air. A computational technique, using finite differences, was developed to solve the equations of motion for the fluidized bed. The method was applied to predict Couette flow and compare the predictions with published

experimental results. This technique was further applied to predict the sensitivity of the flow to the sphericity and size of the fluidized particles.

Next, experiments were examined which involved momentum transfer from buried gram scale explosive charges to rigid structures initially suspended above the surface of the water or soil. Associated computations were performed using an arbitrary Lagrangian Eulerian (ALE) finite element method. The constitutive behavior of the several types of soil involved in the work was defined by means of characterizations using high pressure (hundreds of millions of Pascal) uniaxial and triaxial tests at various initial combinations of water content and density; the associated computations were validated using results from blast experiments.

Various trends, sensitivities, and parametric relations, with significant practical importance, were analyzed and reported. Finally, there were analyses of experiments and computations involving momentum transfer to the bottoms of structures with various topologies.

AUTOBIOGRAPHICAL STATEMENT

DAVID M. FOX

EDUCATION

2009-Present

PhD in Mechanical Engineering, Wayne State University, MI, USA

1990-1996

MSE in Mechanical Engineering, Western Michigan University, MI, USA

1976-1979

BS in Chemistry, Grand Valley State University, Allendale, MI, USA

RECENT EXPERIENCE

2009-Present

Mechanical Engineer, US Army Research Laboratory, MD, USA

2005-2009

Mechanical Engineer, US Army TARDEC, MI, USA

1999-2005

Senior Engineer, Lear Corporation, MI, USA

1989-1999

Senior Engineer, United Technologies Corporation, MI, USA

RECENT PUBLICATIONS

Peer-reviewed journal articles

1. Fox, David M. and Lee, Joon Sang, 2009, Development and evaluation of a model for soil-air fluidized bed rheological behavior, *Int. J. Num. Meth. Fluids*, **61**(7), pp. 810-826.
2. Fox, D.M., Huang, X., Jung, D., Fournery, W. L., Leiste, U. and Lee, J. S., 2011, The response of small scale rigid targets to shallow buried explosive detonations, *Int. J. Impact Eng.*, **38**(11), pp. 882-891.
3. Fournery, W.L., Leiste, U., and Fox, D.M., 2013, The effect of air filled voids on impulse delivered by a buried mine, *Blasting and Fragmentation Journal*, **7**(1), pp. 31ff.
4. Fox, D.M., Lee, J.S., 2014, The influence of water, dry sand, and unsaturated sand constitutive behavior on the blast response of a rigid target, *Int. J. Impact Eng.*, **65**, pp. 163-173.
5. Fox, D.M., Akers, S.A., Leiste, U.H., Fournery, W.L., Windham, J.E., Lee, J.S., Ehrgott, J.Q. and Taylor, L.C., 2014, The effects of air filled voids and water content on the momentum transferred from a shallow buried explosive to a rigid target, *Int. J. Impact Eng.*, **69**, pp. 182-193.

Conference proceedings

1. Fox. D.M. and Lee, J.S., 2011, Application of an Arbitrary Lagrangian Eulerian Method to Describe High Velocity Gas-Particle Flow Behavior, in: *Proceedings, ASME-JSME-KSME 2011 Joint Fluids Engineering Conference, Hamamatsu, Japan*, pp.1507-1514.